



รายงานวิจัยฉบับสมบูรณ์

โครงการ Fundamental model building in controlled cell growth

รศ.ดร.ดวงกมล เบ้าวัน

รายงานวิจัยฉบับสมบูรณ์

โครงการ Fundamental model building in controlled cell growth

รศ.ดร. ดวงกมล เบ้าวัน ภาควิชาคณิตศาสตร์ คณะวิทยาศาสตร์ มหาวิทยาลัยมหิดล

สนับสนุนโดยสำนักงานกองทุนสนับสนุนการวิจัย และมหาวิทยาลัยมหิดล

(ความเห็นในรายงานนี้เป็นของผู้วิจัย สกว. และมหาวิทยาลัยมหิดลไม่จำเป็นต้องเห็นด้วยเสมอไป)

Abstract

The Watson and Crick model for DNA revolutionized thinking in biology and medicine, and initiated many discoveries, demonstrating that model building can not only explain the particular, but can provide deep insights into complex processes that trigger further fundamental advances. Cellular biology is presently characterized by cascading complexity, in the sense that closer inspection only reveals increasing complexity. However, since the Watson and Crick model, while the consequent advances in knowledge have been outstanding in terms of our understanding of some biological processes, there still remain many fundamental questions and there is much experimental data arising from sophisticated measurement that is in need of explanation. This theoretical proposal combines applied mathematics and computer sciences expertise and this purpose is to implement a program of fundamental model building in systems biology, molecular cell biology, material sciences, targeted drug delivery and molecular dynamics simulation.

The integration of nanomaterials with biomolecules yields novel hybrid nanobiomaterials having the combined properties and functions of each, and arising from the unique physical and chemical properties of nanomaterials and the unique recognition characteristics of the cells of the biomaterial. The interactions of nanobiomaterials with living cells offers new opportunities in research and medicine, including understanding cell biology, tissue engineering, drug and medical device development and regenerative medicine. To advance these applications, understanding the mechanisms of interaction with nanobiomaterials is important as the main objectives of this project.

Keywords: Applied mathematical modelling, Cell mechanics, Cellular modelling

Executive Summary

1. ความสำคัญและที่มาของปัญหา

The Watson and Crick model for DNA revolutionized thinking in biology and medicine, and initiated many discoveries, demonstrating that model building can not only explain the particular, but can provide deep insights into complex processes that trigger further fundamental advances. Cellular biology is presently characterized by cascading complexity, in the sense that closer inspection only reveals increasing complexity. However, since the Watson and Crick model, while the consequent advances in knowledge have been outstanding in terms of our understanding of some biological processes, there still remain many fundamental questions and there is much experimental data arising from sophisticated measurement that is in need of explanation. This theoretical proposal combines applied mathematics and computer sciences expertise and this purpose is to implement a program of fundamental model building in systems biology, molecular cell biology, material sciences, targeted drug delivery and molecular dynamics simulation.

The integration of nanomaterials with biomolecules yields novel hybrid nanobiomaterials having the combined properties and functions of each, and arising from the unique physical and chemical properties of nanomaterials and the unique recognition characteristics of the cells of the biomaterial. The interactions of nanobiomaterials with living cells offers new opportunities in research and medicine, including understanding cell biology, tissue engineering, drug and medical device development and regenerative medicine. To advance these applications, understanding the mechanisms of interaction with nanobiomaterials is important as the main objectives of this project.

2. วัตถุประสงค์

- 1. Provide new advanced mathematical models for a range of problems in cell biology, impinging on cellular interactions with their selves, with material surfaces and with nanoparticles.
- 2. Exploit continuous modelling approach used in nanotechnology in the context of cell biology, and in particular for cell-cell interactions, cell-nanobiomaterial interactions for regulating cell behaviour, and to determine the effect of nanoparticles in a cellular environment.
- 3. Use computer simulation technique to confirm mathematical finding.
- 4. Encourage PhD students into the vital area of mathematical modelling in nanobiotechnology.

3. ระเบียบวิธีวิจัย

- 1. Formulate a mathematical model to determine an interaction energy between cell and biomolecule where Lennard-Jones potential and the continuous approximation are utilized.
- 2. In the case that there exists an electrostatic energy in the system, the Columbic potential may be included.
- 3. Find an analytical expression to determine the molecular interaction for a range of problems in cell biology.
- 4. Use computer simulation techniques such as molecular dynamic simulation or molecular mechanic simulation to compare the result with the one obtained by mathematical model.
- 5. Modify our model to incorporate environment factors for example temperature and pressure of the system to make our model be more realistic.

4. แผนการดำเนินงานวิจัยตลอดโครงการในแต่ละช่วง 6 เดือน

First year

A eth sition	Months	Months	Months	Months
Activities	1-3	4-6	7-9	10-12
1. Formulate mathematical model to explain				
the interaction energy between cell and	•	-		
biomolecules.				
2. Determine our model numerically.		4	-	
3. Analyse our results and compare with				
computational simulation method.			•	-
4. Write a manuscript and submit for			4	
publication.				
5. PhD and Master degree students	4			-

Second year

A eth sition	Months	Months	Months	Months
Activities	1-3	4-6	7-9	10-12
1. Modify our model to include	•	•		
environmental effects, i.e. temperature and				
pressure.				
2. Determine our model numerically.		◀	•	
3. Analyse our results and compare with		4	•	
computational simulation method.				
4. Write manuscript(s) and submit for				
publication.			•	•
5. Study molecular dynamics simulation	4			
package(s).				
6. Attend a conference.	•			-
7. PhD and Master degree students	•			-

Third year

Activities	Months	Months	Months	Months
Activities	1-3	4-6	7-9	10-12
1. Use molecular dynamics simulation	•		-	
technique to determine the interaction				
behaviour between cells and biomolecules.				
2. Analyse our results and compare with		•	•	
computational simulation method.				
3. Write manuscript(s) and submit for				
publication.			•	•
4. Attend conference(s).	-			-
5. PhD and Master degree students	•			-

5. ผลงาน/หัวข้อเรื่องที่คาดว่าจะตีพิมพ์ในวารสารวิชาการระดับนานาชาติ

With this research project, we promise to have one PhD student and one Master degree student involving in this project, and at least four accepted manuscripts. Tentative titles for the four manuscripts are as follow

- 1. The role of applied mathematics in bionanotechnology; will be submitted to Nanoscale (IF 2013: 6.739)
- 2. Theoretical prediction for the encapsulation of a drug molecule into lipid nanotubes; will be submitted to Journal of mathematical chemistry (IF 2013: 1.270)
- 3. Interaction behaviour between cells and bimolecules; will be submitted to Journal of mathematical chemistry (IF 2013: 1.270)
- 4. Molecular dynamics simulation for molecular binding; will be submitted to Journal of computational and theoretical nanoscience (IF 2013: 1.032).

6. งบประมาณโครงการ

	ปีที่ 1	ปีที่ 2	ปีที่ 3	รวม
1. หมวดค่าตอบแทน	240,000	240,000	240,000	720,000
- ค่าตอบแทนหัวหน้าโครงการ				
10,000 x 12 / ปี				
2. หมวดค่าวัสดุ	15,000	10,000	10,000	35,000
- ค่าวัสดุทั่วไป อาทิเช่น วัสดุสำนักงาน				
3. หมวดค่าใช้สอย	35,000	80,000	80,000	195,000
- ค่าถ่ายเอกสาร	5,000	5,000	5,000	
- ค่าตีพิมพ์ผลงานวิชาการ	10,000	50,000	50,000	
- ค่าเข้าร่วมประชุมวิชาการ	-	25,000	25,000	
4. ครุภัณฑ์	50,000	-	-	50,000
- Computer notebook ¹				
รวมงบประมาณโครงการ	340,000	330,000	330,000	1,000,000

¹ งานวิจัยหลักของโครงการวิจัยนี้คือการคำนวณโดยใช้คอมพิวเตอร์ จึงจำเป็นที่ต้องใช้เครื่อง คอมพิวเตอร์ที่มีคุณภาพดีในการคำนวณ ดังนั้นจึงมีความจำเป็นที่ต้องซื้อเครื่องคอมพิวเตอร์โน้ตบุค สำหรับงานวิจัยนี้

รายละเอียดโครงการ

- 1. Project title Fundamental model building in controlled cell growth
- 2. Principal investigator
 - **2.1 Name** Miss Duangkamon Baowan Age 32
 - **2.2 Position** Assistant Professor Salary 36,000 baht
 - **2.3 Education** PhD in applied mathematics, University of Wollongong, Australia, 2008

Title of thesis Mathematical Modelling of Nanostructures

2.4 Institute Department of Mathematics, Faculty of Science,

Mahidol University

Address 272 Rama VI Road, Ratchathewi District, Bangkok 10400, THAILAND

2.5 Telephone 022015350, 0850760800

Email address duangkamon.bao@mahidol.ac.th

2.6 Weekly hours intended to spend on this project 20 hour per

week

เนื้อหางานวิจัย

Here we focus on using applied mathematical model to determine the energy for the systems consisting of bionanomolecules. Lennard-Jones potential function is utilized as a force field, and the continuous approximation where atoms on a molecule is assumed to be uniformly distribution on the surface or the volume of the molecule is employed to determined the total energy of the system.

Firstly, we review the use of applied mathematical modeling in order to determine the atomic and molecular interaction energies between nanoscale objects. In particular, we examine the use of the 6-12 Lennard-Jones potential and the continuous approximation, which assumes that discrete atomic interactions can be replaced by average surface or volume atomic densities distributed on or throughout a volume. The considerable benefit of using the Lennard-Jones potential and the continuous approximation is that the interaction energies can often be evaluated analytically, which means that extensive numerical landscapes can be determined virtually instantaneously. Formulae are presented for idealized molecular building blocks and then various applications of the formulae are considered. The modeling approach reviewed here can be applied to a variety of interacting atomic structures and leads to analytical formulae suitable for numerical evaluation.

On using the Lennard-Jones potential together with the continuous approximation, we determine the interaction energy of admantane molecules, the smallest diamondoid, and that of an admantane molecule and a carbon nanotube. Then, more complicated systems are studied which are the penetration of a spherical gold nanoparticle into a lipid nanotube and the encapsulation of a drug molecule encapsulated in lipid nanotube are determined. Finally, we determine the mechanical behavior of atomic force microscope cantilever system.

1. Mathematical modeling of interaction energies between nanoscale objects

For much of this research we are concerned with evaluating the van der Waals interaction energy between atoms, molecules and nanostructures. There are a number of different potential functions which may be used to model the van der Waals potential function. However, we will primarily concern ourselves with the

Lennard-Jones potential function $\Phi(
ho)$ which for two non-bonded atoms may be written in the form

$$\Phi(\rho) = -\frac{A}{\rho^6} + \frac{B}{\rho^{12}} \tag{1}$$

where ρ is the distance between the interacting atoms, and A and B are empirically determined constants of attraction and repulsion, respectively. The graph of Lennard-Jones potential function is as shown in Fig. 1.

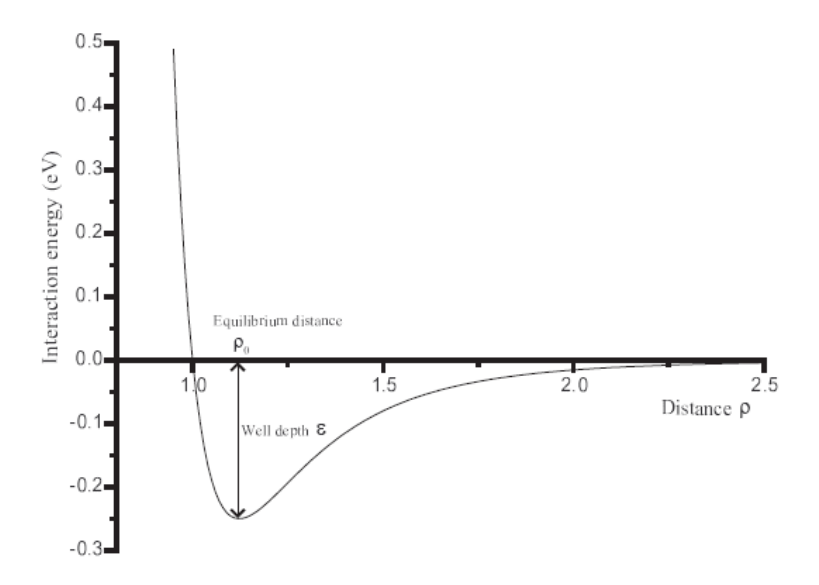


Fig.1 Lennard-Jones function

When calculating the van der Waals interaction between molecules containing a number of atoms, the pairwise interactions may be summed to derive a total interaction E which is given by

$$E = \sum_{i} \sum_{j} \Phi(\rho_{ij}) \tag{2}$$

where the indices i and j vary over all the atoms in each molecule and ρ_{ij} denotes the distance between atoms i and j. Obviously this formulation requires that we know the precise location of every atom in both molecules and we are required to perform ij individual calculations of the potential function $\Phi(\rho_{ij})$ to calculate the total interaction energy for the two molecules. These two considerations can be inconvenient or unnecessarily intensive computationally for situations when the exact orientations of the molecules are not specified or when large nanostructures are involved. Therefore, for most of this book we will make an approximation where

we assume that all the atoms are smeared over ideal lines or surfaces which represent the molecules that we are modelling. With this approximation we are able to replace the explicit summations in (2) with line or surface integrals that allow us to write

$$E = \eta_1 \eta_1 \int_{S_1} \int_{S_2} \Phi(\rho) dS_2 dS_1 \tag{3}$$

where here ρ denotes the distance between typical infinitesimal surface elements dS_1 and dS_2 of the lines or surfaces S_1 and S_2 , respectively, and the terms η_1 and η_2 are the atomic densities (i.e. atoms per unit surface area) of the surfaces S_1 and S_2 , respectively.

From these considerations we see that the task of calculating the van der Waals interactions will be made considerably easier provided that there are methods to readily evaluate integrals of the form of (3) over various lines and surfaces which are relevant to problems in nanotechnology. It turns out that many of the molecules and nanostructures that we encounter can be modelled very realistically by the basic geometric objects of points, straight lines, flat planes, spheres and right circular cylinders, and therefore integrals over these objects will be needed frequently throughout the remainder of this research. Accordingly, the purpose of here is to address these integrals in a systematic way to facilitate the evaluation of ideal van der Waals interactions.

When we investigate the form of the Lennard-Jones potential function $\Phi(\rho)$ given in (1) in the context of the integral formulation of (3) we note that the attractive term ρ^{-6} and the repulsive term ρ^{-12} can be separated and integrated independently. We also note that the two terms only vary in terms of the coefficients A and B, and the magnitude of the index which is applied to the distance variable ρ . In subsequent sections we shall occasionally make use of the fact that the indices of ρ in (1) are both negative even integers which leads us to express the Lennard-Jones potential function $\Phi(\rho)$ in the form

$$\Phi(\rho) = -AI_3(\rho) + BI_6(\rho) \tag{4}$$

where $I_n(\rho) = \rho^{-2n}$ and we will consider evaluating integrals of the form

$$I = \int_{S_1} \int_{S_2} I_n(\rho) dS_2 dS_1 \tag{5}$$

Finally, we must comment on why we seek analytical evaluation to integrals of the form given in (5). While such integrals can be handled reasonably easily using numerical methods it should be remembered that our goal is to elucidate as much as possible from the models that we develop. In some cases, this can involve constructing a broad landscape of data which might be extremely costly or even inaccessible using purely numerical methods but which may be accessed by evaluating analytical expressions for the potential functions in question. Analytical expressions can also be employed to derive expressions for other quantities, like the force experienced by a molecule would otherwise only be determined by further numerical evaluation. One can always move from the analytical to the numerical but the reverse is not possible.

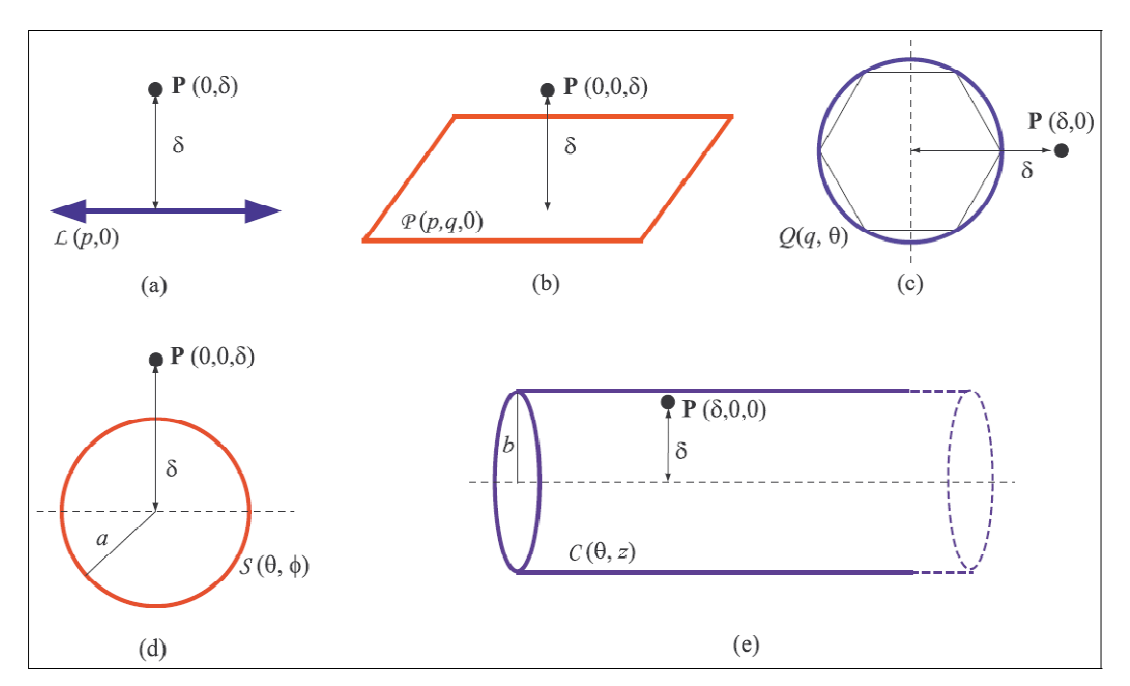


Fig. 2 Interaction of atoms with idealized building blocks: (a) point with line, (b) point with plane, (c) point with ring, (d) point with spherical surface, and (e) point with infinitely long right-cylindrical surface.

(D. Banwan and J.M. Hill, Advances in Mechanical Engineering 2016, Vol. 8(11) 1–16)

Five possible configurations considered here are shown in Fig. 2, where we obtain the interaction energies for each type as shown in Table 1.

Table 1: Equations for five interaction energy configurations where B(x,y) is the beta function and F(x,y;z;w) is the hypergeometric function.

Interaction energy	Equation	
between atom and		
Atomic line	$I = \delta^{1-2n} B\left(n - \frac{1}{2}, \frac{1}{2}\right)$	
Atomic plane	$I = \frac{\pi}{(n-1)\delta^{2n-2}}$	
Atomic ring	$I = \frac{2\pi q}{(\beta - \alpha p)^n} F\left(n, \frac{1}{2}; 1; \frac{2\alpha q}{(\alpha q - \beta)}\right)$	
Atomic spherical surface	$I = \frac{\pi a}{\delta(n-1)} \left[\frac{1}{(\delta-a)^{2(n-1)}} - \frac{1}{(\delta+a)^{2(n-1)}} \right]$	
Infinite atomic cylindrical surface	$I = \frac{2\pi b}{\delta^{2n-1}} B\left(n - \frac{1}{2}, \frac{1}{2}\right) F\left(n - \frac{1}{2}, n - \frac{1}{2}; 1; \frac{b^2}{\delta^2}\right)$	

2. Continuous approximation for interaction energy of adamantane encapsulated in carbon nanotubes

The continuous or continuum approach is employed to determine the interaction energies between two adamantane molecules and that of an adamantane molecule inside a carbon nanotube using the Lennard-Jones potential function. Adamantane is modelled as a perfect sphere with ${\rm sp}^3$ hybridization structure such as is found in diamond, while the carbon nanotube is assumed to be a cylinder with the ${\rm sp}^2$ hybridization structure such as is found in graphene.

Calculation of the interaction energy using a radius of 1.773 Å for the adamantane molecule, we find that the equilibrium distance between the two

adamantane molecules is 6.863 Å as measured from their centers which is within 10% of *ab inito* DFT calculations. However, the predicted binding energy is 52% different from the DFT calculations since only the van der Waals energy is taken into account here.

It is also found that the smallest radius of carbon nanotube that can encapsulate the adamantane is 4.847 Å which is within 2% of *ab inito* DFT calculations. The offset position e from the tube axis is also examined, and a linear relation for $\mathcal{E} \approx b - a - c_{\mathcal{E}}$ is obtained where the distance between molecule and tube wall is $c_{\mathcal{E}} = 3.446$ Å. The equilibrium distance between two molecules, suction energy for encapsulation and offset position depend linearly on the radius of the adamantane. We note that the structural information predicts the stable configurations close to those obtained from the DFT when taking only dipole-dipole interaction into account.

The major benefit of the mathematical modelling approach presented here is the use of significantly less computational resources and simplification reducing the trial-and-error process for designing experiments which allows to consider more complex systems. These findings constitute a first step toward the design of novel hybrid materials of carbon nanostructures.

3. Penetration of spherical gold nanoparticle into a lipid bilayer

The continuous approach and the Lennard-Jones potential function were employed to determine the penetration behaviour for three spherical gold nanoparticles of different radii through a lipid hole. A circular hole is assumed to be in the bilayer and the particles are initiated at rest above the bilayer. Both surface and volume integrals are evaluated to calculate the total nonbonded interaction energy of the system. An analytical expression is obtained in terms of the particle radius a, the hole radius b and the perpendicular distance from the centre of the particle to the bilayer surface Z.

In all the three cases, there are similar regions for the penetration behaviour. In the first region, the nanoparticle behaves like a hard sphere. As the circular hole radius in the bilayer increases, the particle penetrates the bilayer and relocates inside the layer until the radius acquires a critical value, which for the three cases considered are b = 20.79, 23.14 and 27.02 Å corresponding to the

particle radii a=10, 15 and 20 Å, respectively. Once the spherical gold nanoparticles enter the bilayer under no additional applied external force and charge, they tend to remain at the mid-point of the bilayer rather than penetrating further into the cell.

4. Mathematical model for drug molecules encapsulated in lipid nanotubes

Lipid nanotube is considered as a nanocontainer for drug and gene delivery. It is important to understand a basic idea of the encapsulation process. In this work, we use the Lennard-Jones potential function and the continuous approximation to explain the energy behaviour of three hollow shapes of Doxorubicin (DOX) clusters that are a sphere, a cylinder, and an ellipsoid interacting with the lipid nanotube. The schematic model for lipid nanotube is shown in Fig. 3.

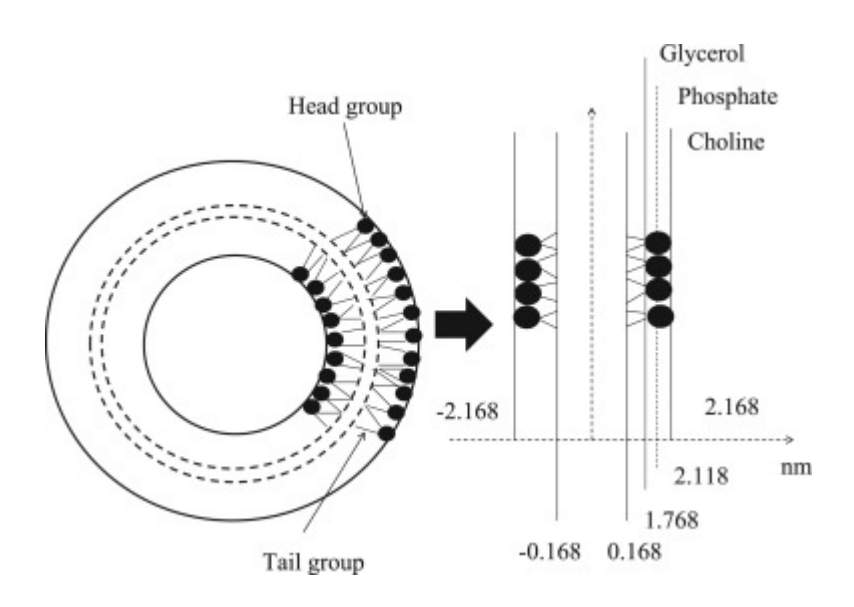


Fig 3. Diagram for lipid nanotube

On assuming that the surface areas of the three structures are equal, we can find the minimum size of the lipid nanotube that encapsulates DOX inside by determining the suction energy. Moreover, we find that a long cylindrical drug provides the largest suction energy among other structures studied here due to the perfect fit between the cylindrical drug and the cylindrical tube. This investigation is the first step to develop the design of nanocapsule for medical application.

5. Mathematical methods on atomic force microscope cantilever systems

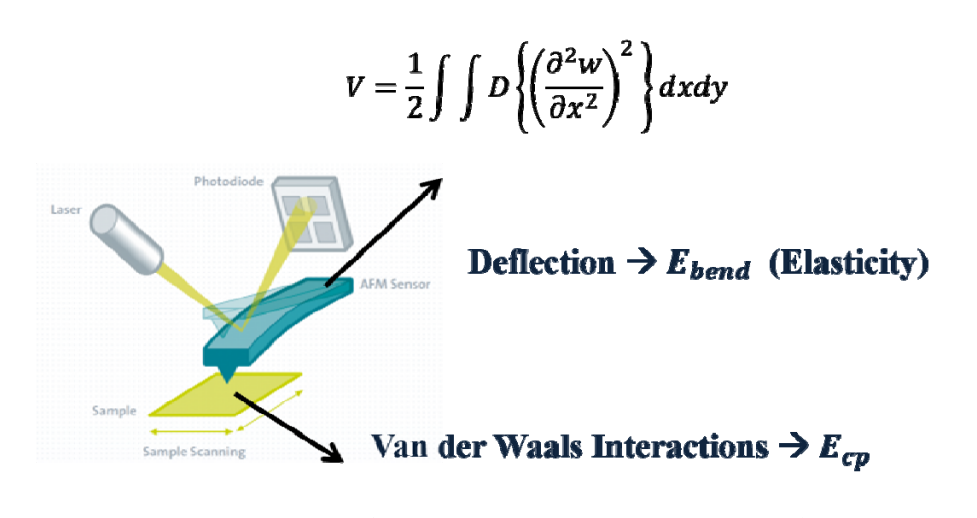
Here a theoretical study of the AFM cantilever system is presented, employing the variational calculus and the Lennard-Jones potential to determine the bending behaviour of the system, and the calculation comprises two procedures, as shown in Fig. 4. Firstly, we compute the energy between the silicon tip and the graphene plane, assuming the silicon tip is a cone, and it can act both vertical and inclined to the plane. Secondly, we solve the potential equation for the plate to deduce a bending equation, for which the solution describes the bending behaviour, and it can be used to determine the spring constant and the potential energy that is stored in the cantilever beam. We propose that the geometry of the cantilever is an isosceles trapezoid, mainly focusing on a V-shaped cantilever.

In the first procedure, we obtain the energy equations of the right cone and that of the tilted cone. In the case of the tilted cone, when the tilted angle is zero, the energy equation gives rise to the energy of the right cone of the same cone angle. Both cases have an equilibrium distance at $[B/(30A)]^{1/6}$. Moreover, the cone angle and the tilted angle do not affect the value of equilibrium distance where it is obtained as 0.206 nm.

In the second procedure, the bending profile tends to a parabola. On comparison with the spring constant to other works, our k_w gives a lower value, the results show 30–50% difference and when r increases, this difference increases.

Our method gives an alternative approach to determine the bending behaviour of the cantilever and the tip response to the surface. This analytical method is relevant in the determination of the distance, energy, and force that are the main considerations in any study of the mechanics of the system. Our approach gives a better understanding of the relations between the substrate surface, the bending distance and the properties of the surface. Moreover, this approach can be applied to any shape of the cantilever and any surface. For a given substrate, we can calculate the appropriate distance between the tip and the sample so as to fix the position of the cantilever to accommodate the bending angle. Further, if we know the surface level from the monitor and we know the bending distance or angle, we can then predict the molecules on the substrate. In the theoretical analysis, our calculation utilizes the calculus of variation, and coordinate transformation of the atoms to model the cantilever system. The approach may involve some

approximations but it gives a numerical solution that is faster than that obtained by computer simulation. Hence, we believe that the approach adopted here might be used in many future studies, not only for the cantilever system but also for any mechanical systems involving a scanning step, so that we might quickly determine a reliable solution by means of a simple mathematical formula.



$$E = \eta_1 \eta_2 \int_{S_1} \int_{S_2} \Phi(\rho) dS_2 dS_1$$

Fig 4. Two energies contribution for AFM (modified from http://www.witec.de/techniques/afm/).

Output ที่ได้จากโครงการ

- 1. **D. Baowan*** (2015) Penetration of spherical gold nanoparticle into a lipid bilayer, *ANZIAM Journal*, Vol. 57, pp. 18-28. (IF 2016: 0.898)
- 2. **D. Baowan*** and J. M. Hill (2016) Mathematical modeling of interaction energies between nanoscale objects: A review of nanotechnology applications, *Advances in Mechanical Engineering*, Vol. 8, pp. 1-16. (IF 2016: 0.827)
- 3. K. Sumetpipat, **D. Baowan***, B. J. Cox and J. M. Hill (2016) Mathematical methods on atomic force microscope cantilever systems, *RSC Advances*, Vol. 6, pp. 46658-46667. (IF 2016: 3.108)
- 4. S. Putthikorn and **D. Baowan*** (2016) Mathematical model for drug molecules encapsulated in lipid nanotube, *Physica A*, Vol. 461, pp. 46-60. (IF 2016: 2.243)
- 5. **D. Baowan***, J. M. Hill and W. Bacsa (2018) Continuous approximation for interaction energy of adamantane encapsulated inside carbon nanotubes, *Chemical Physics Letters*, Vol. 693, pp. 34-39. (IF 2016: 1.759)

PENETRATION OF SPHERICAL GOLD NANOPARTICLE INTO A LIPID BILAYER

D. BAOWAN^{1,2}

(Received 23 April, 2012; accepted 8 July, 2014; first published online 19 August 2015)

Abstract

Safety issues for the use of products containing nanoparticles need to be considered, since these nanoparticles may break through human skin to damage cells. In this paper, applied mathematical techniques are used to model the penetration of a spherical gold nanoparticle into an assumed circular hole in a lipid bilayer. The 6–12 Lennard-Jones potential is employed, and the total molecular interaction energy is obtained using the continuous approximation. Nanoparticles of three different radii, namely, 10, 15 and 20 Å, are studied, which are initiated at rest, confined to the axis of the hole. A similar behaviour for these three cases is observed. The critical hole radii at which these nanoparticles enter the bilayer are 12.65, 17.62 and 22.60 Å, respectively. Further, once the hole radii become larger than 20.79, 23.14 and 27.02 Å, respectively, the gold nanoparticles tend to remain at the mid-plane of the bilayer, and do not pass through the bilayer.

2010 Mathematics subject classification: primary 74G65; secondary 00A69.

Keywords and phrases: gold nanoparticles, interaction energy, Lennard-Jones potential, lipid bilayer.

1. Introduction

Nanoparticles have many potential benefits which can outweigh any potential hazard and possible side effects [7]. They are widely used in many industrial and consumer products, such as stain-resistant textiles or cosmetics [16, 23]. These products, while they are close to the human skin, raise many health and environmental issues. For example, nanocomposites on cloth may be released during the washing process, or nanosomes in cosmetics may penetrate the skin and subsequently damage the skin cells [23].

Gold nanoparticles have been comprehensively studied in many biological and medical areas, and extensive reviews can be found in the literature [4, 5, 9, 17, 18].

¹Department of Mathematics, Faculty of Science, Mahidol University, Rama VI Rd., Thailand;

²Centre of Excellence in Mathematics, CHE, Si Ayutthaya Rd., Bangkok 10400, Thailand; e-mail: duangkamon.bao@mahidol.ac.th.

[©] Australian Mathematical Society 2015, Serial-fee code 1446-1811/2015 \$16.00

Moreover, it has been shown that mammalian cells can uptake gold nanoparticles [6], and they have been successfully employed in cancer therapies [12]. As a result, gold nanoparticles may be used as an example to study the penetration behaviour of nanoparticles through human skin. There are various shapes of gold nanoparticles which can be controlled during the growth processes. In this paper, the gold nanoparticle is assumed to be a dense sphere.

A lipid bilayer is very thin as compared to its lateral dimensions with a hydrophilic head group on the outer surface of thickness 8-9 Å, and with a hydrophobic core typically approximately 30-40 Å thick, depending on the chain length and chemistry [13, 20]. In terms of energy determination, Berger et al. [3] have utilized molecular dynamics simulations together with the 6-12 Lennard-Jones potential function and an electrostatic term to study the interaction for the bilayer of dipalmitoylphosphatidylcholine (DPPC) under various conditions. Further, other researchers have adopted a coarse grain model to study the behaviour of the lipid bilayer, which reduces the complexity of the bilayer system [8, 15, 21, 22, 24]. Moreover, Shelley et al. [21] have concluded that the coarse grain model is more efficient than the Monte Carlo simulations to model the self-assembly of phospholipids. The physical translocation of various nanoparticle shapes through the bilayer has been studied by Yang and Ma [25], and their findings provide a practical guide to the geometry considerations for drug and gene carriers. Further, a mathematical modelling approach was used by Baowan et al. [1] to study the penetration of a C_{60} fullerene into the lipid bilayer, and a relation between particle size, hole size and the location of the particle in the bilayer was determined. Here, a model similar to that given by Baowan et al. [1] is employed to determine the corresponding penetration behaviour for gold nanoparticles.

In this paper, the penetration of a spherical gold nanoparticle through an assumed circular hole in a lipid bilayer is investigated. The Lennard-Jones potential and a continuous approach are introduced in Section 2. The continuous approach assumes that atoms in a molecule are uniformly distributed over a surface or throughout the volume of the molecule, and then an integration approach is employed to evaluate the total energy of the system. Assuming that the gold nanoparticle is a dense sphere and that the head (tail) group of the bilayer is represented by a flat plane (rectangular box), the surface integral and the volume integral approach to determine the molecular interaction energy are detailed in Section 3. Numerical results obtained from the analytical expressions are given in Section 4 and, finally, a summary of the analysis is presented in Section 5.

2. The Lennard-Jones function and continuous approximation

This study aims at computing the energy of a system involving a nanoparticle and a biomolecule of several nanometres in size. The mere size of the system renders an atomistic modelling approach very expensive. Even a coarse grained particle approach would involve computing around thousands of pairwise interactions. Instead, a much

more efficient continuous approach is used that considers the same typical nonbonded interaction. Moreover, it has been shown that such interaction based on the Lennard-Jones potential plays a major role in order to determine an equilibrium configuration of nanomaterials [2].

The classical 6–12 Lennard-Jones function is given by

$$\Phi = -\frac{A}{\rho^6} + \frac{B}{\rho^{12}} = 4\epsilon \left[-\left(\frac{\sigma}{\rho}\right)^6 + \left(\frac{\sigma}{\rho}\right)^{12} \right],$$

where ρ denotes the distance between two typical points, and A and B are attractive and repulsive Lennard-Jones constants, respectively. Further, ϵ is a well depth and σ represents a van der Waals diameter of an atom. The Lennard-Jones parameters in a system of two atomic species can be obtained using the empirical combining laws or mixing rules [11], which are given by $\epsilon_{12} = \sqrt{\epsilon_1 \epsilon_2}$ and $\sigma_{12} = (\sigma_1 + \sigma_2)/2$, where 1 and 2 refer to the respective individual atoms.

Using the continuous approach, where the atoms at discrete locations on the molecule are averaged over a surface or a volume, the total energy is obtained by calculating integrals over the surface or the volume of each molecule, given by

$$E = \eta_1 \eta_2 \int_{S_2} \int_{S_1} \left(-\frac{A}{\rho^6} + \frac{B}{\rho^{12}} \right) dS_1 dS_2,$$

where η_1 represents the mean volume density of the volume element S_1 on the nanoparticle. The second element S_2 is assumed to be either the head or the tail group of the lipid with the mean surface or the mean volume density η_2 , respectively. Further, the integral I_n is defined as

$$I_n = \int_{S_1} \int_{S_2} \rho^{-2n} dS_2 dS_1, \quad n = 3, 6,$$
 (2.1)

and, therefore, $E = \eta_1 \eta_2 (-AI_3 + BI_6)$.

The Lennard-Jones parameters for the lipid bilayer are taken from the work of Marrink et al. [15]. The head group is assumed to be a charged site Q, whereas the tail group is assumed to be an apolar site C, both interacting with a nonpolar and nonhydrogen bonding gold nanoparticle N_0 . The parameter values for Q, C and N_0 can be found in the work of Marrink et al. [15], and these values for both head and tail groups are the same. From the coarse grain model, there are two and eight interaction sites for the head and tail groups, respectively [15], which contribute to the total energy of the system. Further, the head group is assumed to be represented as a flat plane, while the tail group is described as a rectangular box with a tail length ℓ . The mean atomic surface density for the head group and the mean atomic volume density for the tail group are based on the work of Baowan et al. [1].

The Lennard-Jones parameters for gold nanoparticles are taken from the work of Pu et al. [19]. Since gold adopts a face-centred-cubic (FCC) crystal structure where there are four atoms occupied in a unit cell, the mean atomic volume density for the gold nanoparticle can be determined using the atomic radius of 1.44 Å. The parameters used in this model are given in Table 1.

TABLE 1. Numerical values of constants used in the model.

Well depth of Au atoms within gold nanoparticle (meV)	$\epsilon_1 = 1.691$
Well depth of atoms within the head group (meV)	$\epsilon_2 = 35.24$
Well depth of atoms within the tail group (meV)	$\epsilon_3 = 35.24$
van der Waals radius of Au atoms within gold nanoparticle (Å)	$\sigma_1 = 2.934$
van der Waals radius of atoms within the head group (Å)	$\sigma_2 = 4.70$
van der Waals radius of atoms within the tail group (Å)	$\sigma_3 = 4.70$
Length of lipid tail group (Å)	$\ell = 15$
Mean atomic volume density for gold nanoparticle (\mathring{A}^{-3})	$\eta_{\rm g} = 0.1675$
Mean atomic surface density for head group lipid bilayer (\mathring{A}^{-2})	$\eta_{\text{head}} = 0.0308$
Mean atomic volume density for tail group lipid bilayer (\mathring{A}^{-3})	$\eta_{\text{tail}} = 0.1231/\ell$

3. Interaction energy of system

Here the energy behaviour for a gold nanoparticle of radius a moving through a circular hole in a lipid bilayer of radius b is considered. Further, the gold nanoparticle is assumed to be a dense sphere. Also, the lipid bilayer is assumed to be an infinite plane consisting of two head groups and two tail groups with a separation distance of $\delta = 3.36$ Å between the two layers [1] (see Figure 2). The total energy between a lipid bilayer and a spherical nanoparticle comprises the interaction for:

- (i) two head groups and a spherical nanoparticle,
- (ii) two tail groups and a spherical nanoparticle.

First, the volume integral for a spherical nanoparticle interacting with a single atom is considered and described in Section 3.1. Then the interaction energy between a sphere and a flat plane, and that between a sphere and a box, are presented in Sections 3.2 and 3.3, respectively.

3.1. Volume integral of a sphere interacting with single atom The model formation for the interaction energy between a sphere and a point is shown in Figure 1. Then the integral I_n defined by (2.1) becomes

$$I_n = \int_{-\pi}^{\pi} \int_0^a \int_0^{\pi} \frac{r^2 \sin \phi}{(r^2 + \xi^2 + 2r\xi \cos \phi)^n} \, d\phi \, dr \, d\theta,$$

where $\rho^2 = r^2 + \xi^2 + 2r\xi\cos\phi$ and ξ is the distance from the single atom to the centre of the sphere. On making a substitution $t = r^2 + \xi^2 + 2r\xi\cos\phi$ and, since I_n is independent of θ ,

$$I_n = \frac{\pi}{\xi} \int_0^a \int_{(\xi - r)^2}^{(\xi + r)^2} r \frac{1}{t^n} dt dr$$

$$= \frac{\pi}{\xi (n - 1)} \int_0^a r \left[\frac{1}{(\xi - r)^{2(n - 1)}} - \frac{1}{(\xi + r)^{2(n - 1)}} \right] dr.$$

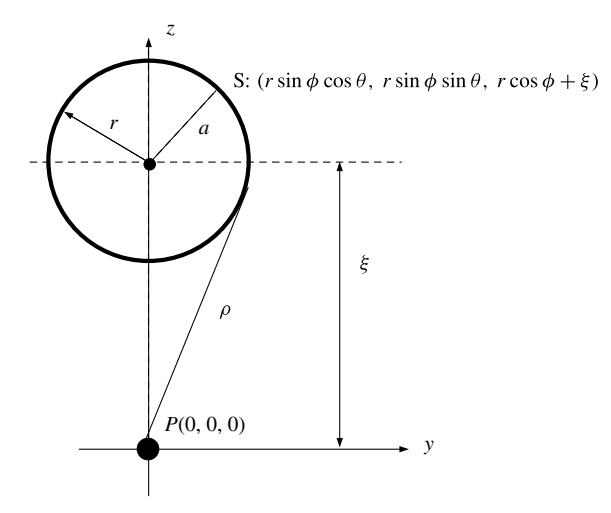


FIGURE 1. Model formation for a sphere interacting with an atom where the single atom is assumed to be located at the origin.

Finally, using integration by parts,

$$I_n = \frac{\pi}{\xi(n-1)} \left[-\frac{a}{(3-2n)} \left\{ \frac{1}{(\xi-a)^{2n-3}} + \frac{1}{(\xi+a)^{2n-3}} \right\} - \frac{1}{(3-2n)(4-2n)} \left\{ \frac{1}{(\xi-a)^{2n-4}} - \frac{1}{(\xi+a)^{2n-4}} \right\} \right].$$

For n = 3 and 6, placing fractions over common denominators, expanding and reducing to fractions in terms of powers of $(\xi^2 - a^2)$ yield

$$I_3 = \frac{4}{3}\pi a^3 \frac{1}{(\xi^2 - a^2)^3},\tag{3.1}$$

$$I_6 = \frac{2\pi a^3}{45} \left[\frac{30}{(\xi^2 - a^2)^6} + \frac{216a^2}{(\xi^2 - a^2)^7} + \frac{432a^4}{(\xi^2 - a^2)^8} + \frac{256a^6}{(\xi^2 - a^2)^9} \right].$$
(3.2)

Therefore, the total interaction energy between the volume of a spherical nanoparticle and a single atom is given by

$$E_{\rm sp} = \eta_{\rm g}(-AI_3 + BI_6),$$

where η_g is the mean volume density of the gold nanoparticle.

For convenience, define the integral

$$J_n = \int_{S_2} \frac{1}{(\xi^2 - a^2)^n} dS_2, \tag{3.3}$$

where n is a positive integer corresponding to the degree of the polynomials in (3.1) and (3.2).

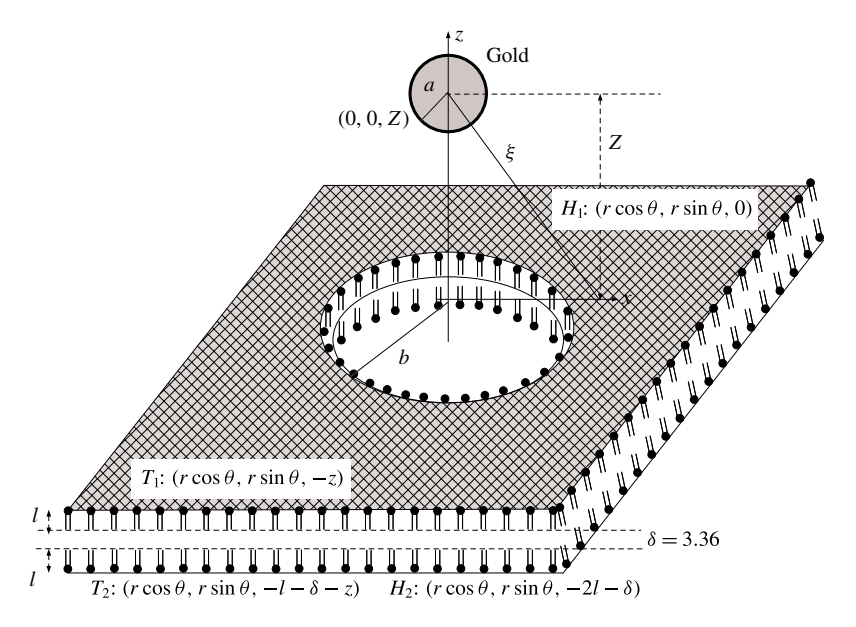


FIGURE 2. Model formation for a sphere interacting with bilayer where the hole in H_1 is assumed to be located at z = 0.

3.2. Interaction energy between a sphere and two head groups The model formation for a spherical gold nanoparticle interacting with a lipid bilayer is depicted in Figure 2. Here H_1 is defined as the head group located on the xy-plane and H_2 as the other head group located at $z = -2\ell - \delta$. Then the interaction energy between the head group H_1 and the sphere is determined. A typical point of H_1 has coordinates $(r\cos\theta, r\sin\theta, 0)$, where $r \in (b, \infty)$ and b is the radius of the hole. The centre of the gold nanoparticle is assumed to be located on the z-axis at (0, 0, Z), where Z represents the perpendicular distance from the upper surface to the centre of the sphere, and at the mid-plane of the bilayer $Z = -\ell - \delta/2$. Therefore, the distance from the centre of the nanoparticle to a typical point on the infinite plane is given by $\xi^2 = r^2 + Z^2$, and the integral in (3.3) becomes

$$J_n = \int_0^{2\pi} \int_h^{\infty} \frac{r}{(r^2 + Z^2 - a^2)^n} dr d\theta = \frac{\pi}{(n-1)(Z^2 + b^2 - a^2)^{n-1}}.$$

Hence, the interaction energy between the head group H_1 and the nanoparticle is

$$E_H(Z) = 2 \left[\eta_g \eta_{head} \left\{ -\frac{4}{3} \pi a^3 A J_3 + \frac{2\pi a^3 B}{45} (30 J_6 + 216 a^2 J_7 + 432 a^4 J_8 + 256 a^6 J_9) \right\} \right], \tag{3.4}$$

where the factor 2 comes from the number of interaction sites on the head group based on the Martini force field [15].

The interaction energy between the head group H_2 and the spherical gold nanoparticle can be obtained in precisely the same way by substituting $Z + 2\ell + \delta$ for Z in (3.4), where δ is the equilibrium spacing between the two layers of the lipid given by 3.36 Å [1].

3.3. Interaction energy between a sphere and two tail groups On assuming that the tail group can be modelled as a rectangular box, the interaction energy between the two tail groups and the spherical gold nanoparticle can be determined. Here T_1 is defined as the tail group connected to the head group H_1 , and H_2 as the other tail group which is connected to the head group H_2 . A typical point of H_1 has coordinates $(r\cos\theta, r\sin\theta, -z)$, where $H_2 \in (0, \ell)$, and $H_3 \in (0, \ell)$ is the tail length. The distance between the centre of the nanoparticle and the surface of the tail group $H_3 \in (0, \ell)$ and $H_3 \in (0, \ell)$ are $H_3 \in (0, \ell)$ and $H_3 \in (0, \ell)$ are $H_3 \in (0, \ell)$ and $H_3 \in (0, \ell)$ are $H_3 \in (0, \ell)$ and $H_3 \in (0, \ell)$ and $H_3 \in (0, \ell)$ and $H_3 \in (0, \ell)$ are $H_3 \in (0, \ell)$ and $H_3 \in (0, \ell)$ and $H_3 \in (0, \ell)$ are $H_3 \in (0, \ell)$ and $H_3 \in (0, \ell)$ and $H_3 \in (0, \ell)$ and $H_3 \in (0, \ell)$ are $H_3 \in (0, \ell)$ and $H_3 \in (0, \ell)$ and $H_$

$$J_n = \int_0^{2\pi} \int_0^{\ell} \int_b^{\infty} \frac{r}{[r^2 + (Z+z)^2 - a^2]^n} dr dz d\theta$$
$$= \frac{\pi}{(n-1)} \int_0^{\ell} \frac{1}{[b^2 + (Z+z)^2 - a^2]^{n-1}} dz.$$

Next, the substitution $Z + z = \sqrt{b^2 - a^2} \tan \phi$ yields

$$J_n = \frac{\pi}{(n-1)(b^2 - a^2)^{n-3/2}} \int_{\tan^{-1}(Z/\sqrt{b^2 - a^2})}^{\tan^{-1}((Z+\ell)/\sqrt{b^2 - a^2})} \cos^{2n-4} \phi \, d\phi \tag{3.5}$$

for n = 3, 6, 7, 8 and 9. The above integral can be found in the work of Gradshteyn and Ryzhik [10, p. 153, 2.513.3], which is

$$\int \cos^{2p} \phi \, d\phi = \frac{1}{2^{2p}} \left[\binom{2p}{p} \phi + \sum_{k=0}^{p-1} \binom{2p}{k} \frac{\sin(2(p-k)\phi)}{p-k} \right],$$

where $\binom{x}{y}$ is the usual binomial coefficient and p = n - 2.

The total interaction energy between the tail group T_1 and the spherical gold nanoparticle is

$$E_T(Z) = 8 \left[\eta_g \eta_{\text{tail}} \left\{ -\frac{4}{3} \pi a^3 A J_3 + \frac{2\pi a^3 B}{45} (30 J_6 + 216 a^2 J_7 + 432 a^4 J_8 + 256 a^6 J_9) \right\} \right], \tag{3.6}$$

where in this case J_n is defined by (3.5) and the factor 8 is the number of the interaction sites of the lipid tail group [15]. The interaction energy for the tail group T_2 and the spherical gold nanoparticle can be obtained by precisely the same technique on replacing Z by $Z + \ell + \delta$ in (3.6).

4. Numerical results

The total interaction between a gold nanoparticle and a lipid bilayer with a hole radius b is given by

$$E^{\text{total}} = E_H(Z) + E_H(Z + 2\ell + \delta) + E_T(Z) + E_T(Z + \ell + \delta),$$

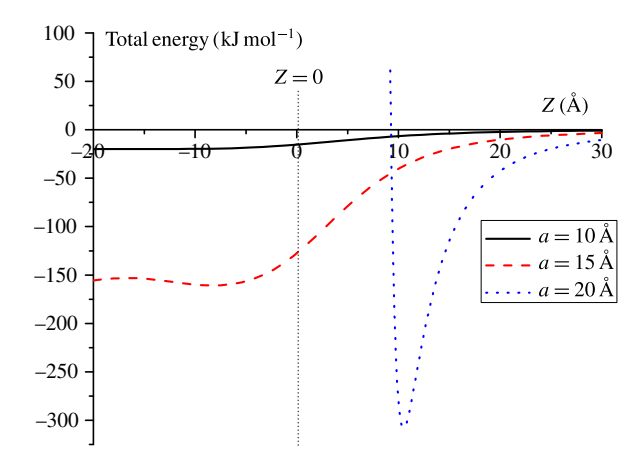


FIGURE 3. Energy profile versus the distance Z for the particles of radii a = 10, 15 and 20 Å, where b is fixed to be 20 Å (Colour available online).

where E_H and E_T are defined in (3.4) and (3.6), respectively. Here, three sizes of the spherical gold nanoparticles are considered, where their radii are 10, 15 and 20 Å. The energy profiles for these three cases are depicted in Figure 3, where the hole radius b is fixed to be 20 Å. The equilibrium positions for the particles of radii 10 and 15 Å are observed to be in the bilayer while the particle of radius 20 Å cannot pass into the bilayer.

The relation between the minimum energy locations Z_{\min} and the circular hole radius b is graphically shown in Figure 4. A positive value of Z_{\min} indicates that the spherical gold nanoparticle is located above the lipid bilayer, while a negative value of Z_{\min} shows that the nanoparticle penetrates into the bilayer. The penetration behaviours of the three cases are similar, and there are two regions which need to be examined.

In the first region, the particles behave like hard spheres, and they do not penetrate into the bilayer until the hole radii in the bilayer are larger than the critical values 12.65, 17.62 and 22.60 Å of b_c for the particle radii 10, 15 and 20 Å, respectively. These values come from the physical particle radii plus the van der Waals repulsive region around the atoms. The three curves in this region are quarter-circles with the radii b_c ; then a simple curve fitting can be used. Further, the curve fittings for these cases are determined and they are given by

$$a = 10,$$
 $Z_{\min} = (12.649^2 - b^2)^{1/2};$
 $a = 15,$ $Z_{\min} = (17.620^2 - b^2)^{1/2};$
 $a = 20,$ $Z_{\min} = (22.603^2 - b^2)^{1/2}.$

In the second region, the particles penetrate into the bilayer and, as b increases further, the particles eventually find the equilibrium position located at the mid-plane of the bilayer, which is at Z = -16.68 Å. Note that this finding is similar to a previous work by the author [1]. The ranges for the hole radii in the second region are

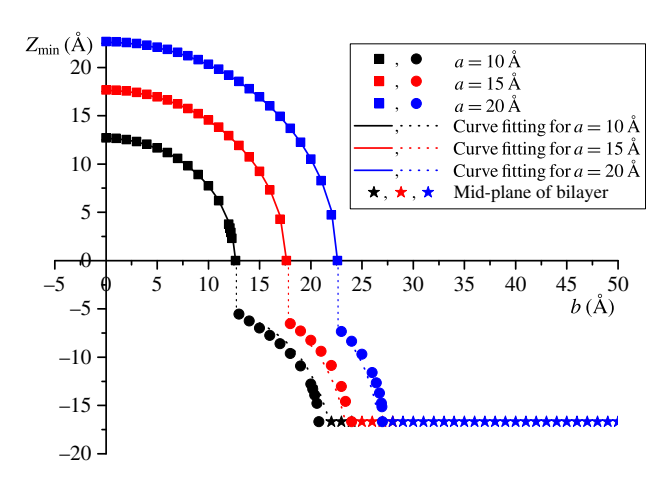


FIGURE 4. Relation between equilibrium location Z_{min} and hole radius b where the radii of gold nanoparticles are assumed to be a = 10, 15 and 20 Å (Colour available online).

12.65 Å < b < 20.79 Å, 17.62 Å < b < 23.14 Å and 22.60 Å < b < 27.02 Å for particle radii a = 10, 15 and 20 Å, respectively. The following curve fittings for the second region are obtained from the rational nonlinear fit using OriginPro 8:

$$a = 10 \text{ Å}, \quad Z_{\min} = (-0.365 + 0.014b)^{-1}, \quad R^2 = 0.986;$$

 $a = 15 \text{ Å}, \quad Z_{\min} = (-0.434 + 0.016b)^{-1}, \quad R^2 = 0.999;$
 $a = 20 \text{ Å}, \quad Z_{\min} = (-0.594 + 0.020b)^{-1}, \quad R^2 = 0.967.$

Note that the dotted line joining region 1 and region 2 shows the jump behaviour of the nanoparticles.

This result agrees well with the work of Lin et al. [14], where the gold nanoparticle does not pass through the lower layer of the lipid. In order to induce the uptake process into the cell, charged nanoparticles may be used to disrupt the hydrophilic head group in forming a vesicle; then an endocytosis process may occur.

5. Summary

The continuous approach and the Lennard-Jones potential function were employed to determine the penetration behaviour for three spherical gold nanoparticles of different radii through a lipid hole. A circular hole is assumed to be in the bilayer and the particles are initiated at rest above the bilayer. Both surface and volume integrals are evaluated to calculate the total nonbonded interaction energy of the system. An analytical expression is obtained in terms of the particle radius a, the hole radius b and the perpendicular distance from the centre of the particle to the bilayer surface a.

In all the three cases, there are similar regions for the penetration behaviour. In the first region, the nanoparticle behaves like a hard sphere. As the circular hole radius in the bilayer increases, the particle penetrates the bilayer and relocates inside the

layer until the radius acquires a critical value, which for the three cases considered are b = 20.79, 23.14 and 27.02 Å corresponding to the particle radii a = 10, 15 and 20 Å, respectively. Once the spherical gold nanoparticles enter the bilayer under no additional applied external force and charge, they tend to remain at the mid-point of the bilayer rather than penetrating further into the cell.

Acknowledgements

The author thanks Dr Barry J. Cox and Professor James M. Hill for many helpful comments on this work. The author is also grateful for the support of the Thailand Research Fund (RSA5880003).

References

- D. Baowan, B. J. Cox and J. M. Hill, "Instability of C₆₀ fullerene interacting with lipid bilayer", J. Mol. Model. 18 (2012) 549–557; doi:10.1007/s00894-011-1086-4.
- [2] D. Baowan, H. Peuschel, A. Kraegeloh and V. Helms, "Energetics of liposomes encapsulating silica nanoparticles", J. Mol. Model. 19 (2013) 2459–2472; doi:10.1007/s00894-013-1784-1.
- [3] O. Berger, O. Edholm and F. Jahnig, "Molecular dynamics simulations of a fluid bilayer of dipalmitoylphosphatidylcholine at full hydration, constant pressure and constant temperature", *Biophys. J.* 72 (1997) 2002–2013; doi:10.1016/S0006-3495(97)78845-3.
- [4] R. Bhattacharya, C. R. Patra, A. Earl, S. Wang, K. Katarya, L. Lu, J. N. Kizhakkedathu, M. J. Yaszemski, P. R. Greipp, D. Mukhopadhyay and P. Mukherjee, "Attaching folic acid on gold nanoparticles using noncovalent interaction via different polyethylene glycol backbones and targeting of cancer cells", *Nanomedicine* 3 (2007) 224–238; doi:10.1016/j.nano.2007.07.001.
- [5] P. C. Chen, S. C. Mwakwari and A. K. Oyelere, "Gold nanoparticles: from nanomedicine to nanosensing", *Nanotechnol. Sci. Appl.* 1 (2008) 45–66; http://www.ncbi.nlm.nih.gov/pmc/articles/PMC3781743.
- [6] B. D. Chithrani, A. A. Ghazani and W. C. W. Chan, "Determining the size and shape dependence of gold nanoparticle uptake into mammalian cells", *Nano Lett.* 6 (2006) 662–668; doi:10.1021/nl052396o.
- [7] V. L. Colvin, "The potential environmental impact of engineered nanomaterials", *Nat. Biotechnol.* **21** (2003) 1166–1170; doi:10.1038/nbt875.
- [8] R. DeVane, A. Jusufi, W. Shinoda, C.-C. Chiu, S. O. Nielsen, P. B. Moore and M. L. Klein, "Parametrization and application of a coarse grained force field for benzene/fullerene interactions with lipids", *J. Phys. Chem. B* 114 (2010) 16364–16372; doi:10.1021/jp1070264.
- [9] P. Ghosh, G. Han, M. De, C. K. Kim and V. M. Rotello, "Gold nanoparticles in delivery applications", Adv. Drug Deliv. Rev. 60 (2008) 1307–1315; doi:10.1016/j.addr.2008.03.016.
- [10] I. S. Gradshteyn and I. M. Ryzhik, *Table of integrals, series, and products*, 7th edn, (Academic Press, San Diego, MA, 2007).
- [11] J. O. Hirschfelder, C. F. Curtiss and R. B. Bird, Molecular theory of gases and liquids (John Wiley, New York, 1954).
- [12] P. K. Jain, I. H. El-Sayed and M. A. El-Sayed, "Au nanoparticles target cancer", Nano Today 2 (2007) 18–29; doi:1016/S1748-0132(07)70016-6.
- [13] B. A. Lewis and D. M. Engelman, "Lipid bilayer thickness varies linearly with acyl chain length in fluid phosphatidylcholine vesicles", *J. Mol. Biol.* 166 (1983) 211–217; doi:10.1016/S0022-2836(83)80007-2.
- [14] J. Lin, H. Zhang, Z. Chen and Y. Zheng, "Penetration of lipid membranes by gold nanoparticles: insights into cellular uptake, cytotoxicity and their relationship", ACS Nano 4 (2010) 5421–5429; doi:10.1021/nn1010792.

- [15] S. J. Marrink, A. H. de Vries and A. E. Mark, "Coarse grained model for semiquantitative lipid simulations", J. Phys. Chem. B 108 (2004) 750–760; doi:10.1021/jp036508g.
- [16] A. Nel, T. Xia, L. M\u00e4dler and N. Li, "Toxic potential of materials at the nanolevel", Science 311 (2006) 622–627; doi:10.1126/science.1114397.
- [17] D. Pissuwan, T. Niidome and M. B. Cortie, "The forthcoming applications of gold nanoparticles in drug and gene delivery systems", *J. Control. Release* 149 (2011) 65–71; doi:10.1016/j.jconrel.2009.12.006.
- [18] D. Pissuwan, S. M. Valenzuela, M. C. Killingsworth, X. Xu and M. B. Cortie, "Targeted destruction of murine macrophage cells with bioconjugated gold nanorods", *J. Nanopart. Res.* 9 (2007) 1109–1124; doi:10.1007/s11051-007-9212-z.
- [19] Q. Pu, Y. Leng, X. Zhao and P. T. Cummings, "Molecular simulations of stretching gold nanowires in solvents", *Nanotechnology* 18 (2007) 424007; doi:10.1088/0957-4484/18/42/424007.
- [20] W. Rawicz, K. C. Olbrich, T. McIntosh, D. Needham and E. Evans, "Effect of chain length and unsaturation on elasticity of lipid bilayers", *Biophys. J.* 79 (2000) 328–339; doi:10.1016/S0006-3495(00)76295-3.
- [21] J. C. Shelley, M. Y. Shelley, R. C. Reeder, S. Bandyopadhyay, P. B. Moore and M. L. Klein, "Simulations of phospholipids using a coarse grain model", J. Phys. Chem. B 105 (2001) 9785–9792; doi:10.1021/jp011637n.
- [22] W. Shinoda, R. DeVane and M. L. Klein, "Zwitterionic lipid assemblies: molecular dynamics studies of monolayers, bilayers, and vesicles using a new coarse grain force field", *J. Phys. Chem. B* 114 (2010) 6836–6849; doi:10.1021/jp9107206.
- [23] T. Thomas, K. Thomas, N. Sadrieh, N. Savage, P. Adair and R. Bronaugh, "Research strategies for safety evaluation of nanomaterials, part VII: evaluating consumer exposure to nanoscale materials", *Toxicol. Sci.* 91 (2006) 14–19; doi:10.1093/toxsci/kfj129.
- [24] E. J. Wallace and M. S. P. Sansom, "Carbon nanotube/detergent interactions via coarse-grained molecular dynamics", *Nano Lett.* 7 (2007) 1923–1928; doi:10.1021/nl070602h.
- [25] K. Yang and Y.-Q. Ma, "Computer simulation of the translocation of nanoparticles with different shapes across a lipid bilayer", Nat. Nanotechnol. 5 (2010) 579–583; doi:10.1038/nnano.2010.141.

Review

Advances in Mechanical Engineering

Advances in Mechanical Engineering 2016, Vol. 8(11) 1–16 © The Author(s) 2016 DOI: 10.1177/1687814016677022 aime.sagepub.com



Mathematical modeling of interaction energies between nanoscale objects: A review of nanotechnology applications

Duangkamon Baowan^{1,2} and James M Hill³

Abstract

In many nanotechnology areas, there is often a lack of well-formed conceptual ideas and sophisticated mathematical modeling in the analysis of fundamental issues involved in atomic and molecular interactions of nanostructures. Mathematical modeling can generate important insights into complex processes and reveal optimal parameters or situations that might be difficult or even impossible to discern through either extensive computation or experimentation. We review the use of applied mathematical modeling in order to determine the atomic and molecular interaction energies between nanoscale objects. In particular, we examine the use of the 6-12 Lennard-Jones potential and the continuous approximation, which assumes that discrete atomic interactions can be replaced by average surface or volume atomic densities distributed on or throughout a volume. The considerable benefit of using the Lennard-Jones potential and the continuous approximation is that the interaction energies can often be evaluated analytically, which means that extensive numerical landscapes can be determined virtually instantaneously. Formulae are presented for idealized molecular building blocks, and then, various applications of the formulae are considered, including gigahertz oscillators, hydrogen storage in metal-organic frameworks, water purification, and targeted drug delivery. The modeling approach reviewed here can be applied to a variety of interacting atomic structures and leads to analytical formulae suitable for numerical evaluation.

Keywords

Mathematical modeling, nanotechnology, Lennard-Jones potential function, continuous approximation, molecular interaction

Date received: 3 March 2016; accepted: 13 September 2016

Academic Editor: Michal Kuciej

Introduction

For the past two decades, nanotechnology has been a major focus in science and technology. However, in various areas of physics, chemistry, and biology, both past and current research involving interacting atomic structures are predominantly either experimental or computational in nature. Both experimental work and large-scale computation, perhaps using molecular dynamics simulations, can often be expensive and time-consuming. On the other hand, applied mathematical modeling often produces analytical formulae giving rise to virtually instantaneous numerical data. This can

significantly reduce the time taken in the trial-and-error processes leading to applications and which in turn significantly decreases the research cost. Here, applied

Department of Mathematics, Faculty of Science, Mahidol University, Bangkok, Thailand

²Centre of Excellence in Mathematics, CHE, Bangkok, Thailand
³School of Information Technology & Mathematical Sciences, University of South Australia, Mawson Lakes, SA, Australia

Corresponding author:

Duangkamon Baowan, Centre of Excellence in Mathematics (CHE), Si Ayutthaya Road, Bangkok 10400, Thailand. Email: duangkamon.bao@mahidol.ac.th mathematical modeling in nanotechnology is reviewed, and particularly, the work of the present authors and their colleagues in the use of classical mathematical modeling procedures to investigate the mechanics of interacting nanoscale systems for various applications, including nano-oscillators, metal-organic frameworks (MOFs), molecular selective separation, and drug delivery.

Throughout, the dominant mechanisms behind these nanoscale systems are assumed to arise from atomic and molecular interactions that can be modeled by the 6-12 Lennard-Jones potential function (see equation (4)), and further simplifications are made by adopting the continuous or continuum assumption. This approximation assumes that two interacting molecules can be replaced by two surfaces or two regions, for which the discrete atomic structure is averaged over the surface or the volume with a constant atomic surface density or a constant atomic volume density, respectively. Basically, the continuous assumption gives an average result, and it is much better suited to those situations involving well-defined surfaces with evenly distributed atoms, such as graphene, carbon nanotubes, or carbon fullerenes. In each of these instances, there exists a uniform distribution of atoms, and the continuous approximation might be most accurate. In the case of non-evenly distributed atomic structures, a hybrid approach is adopted, which deals with the isolated atoms individually, and the continuous approximation is adopted for the remainder. For example, a methane molecule CH₄ is assumed to be replaced by a spherical surface of a certain radius with a constant hydrogen atomic surface density, together with a single carbon atom located at the center of the spherical surface. 1,2

In this review, we comment that we do not include the mechanics of dislocations in metallic materials or the use of the Cauchy–Born rule to bridge interactions since the modeling here assumes that there is no deformation of any surface due to the van der Waals interactions. We refer the reader to Van der Giessent and Needleman³ for a comprehensive study of plastic discrete dislocations and to Biner and Morris⁴ for a computational simulation of the discrete dislocation method. Furthermore, a review of the Cauchy–Born rule can be found in Ericksen.⁵

In the following section, both the 6-12 Lennard-Jones potential function and the continuous approximation are introduced. In the section thereafter, analytical expressions are presented for the interaction energies of the basic molecular building blocks, namely, points, lines, planes, rings, spheres, and cylinders, all deduced utilizing the 6-12 Lennard-Jones potential function together with the continuous approximation. In the section on the mechanics of nanostructures, the mechanics of the so-called gigahertz oscillators is reviewed, including the determination of the energy

and force distributions of this nanostructured device. The development of a mathematical model of MOFs for gas storage is presented in the section thereafter. In the next section, the modeling approach is reviewed for molecular selectivity and separation for water purification, ion separation, and biomolecule selection. In the targeted drug delivery section, we present a review of applied mathematical modeling for targeted drug delivery. A brief overall summary is presented in the final section of this article.

Lennard-Jones atomic interaction potential and the continuous approach

For two separate non-bonded molecular structures, the interaction energy E can be evaluated either directly using a discrete atom—atom formulation or approximately using the continuous approach. Thus, the non-bonded interaction energy may be obtained either as a summation of the individual interaction energies between each atomic pair, namely

$$E = \sum_{i} \sum_{j} \Phi(\rho_{ij}) \tag{1}$$

where $\Phi(\rho_{ij})$ is the potential function for atoms i and j located a distance ρ_{ij} apart on two distinct molecular structures, assuming that each atom on the two molecules has a well-defined coordinate position. Alternatively, the continuous approximation assumes that the atoms are uniformly distributed over the entire surface of the molecule, and the double summation in equation (1) is replaced by a double integral over the surface of each molecule, thus

$$E = \eta_1 \eta_2 \iint \Phi(\rho) dS_1 dS_2 \tag{2}$$

where η_1 and η_2 represent the mean surface densities of atoms on the two interacting molecules, and ρ is the distance between the two typical surface elements dS_1 and dS_2 located, respectively, on the two interacting molecules. Note that the mean atomic surface density is determined by dividing a number of atoms which make up the molecule by the surface area of the molecule. The continuous approximation is rather like taking the average or mean behavior, and in the limit of a large number of atoms, the continuous approximation approaches the energy arising from the discrete model.

The hybrid discrete—continuous approach applies to the modeling of irregularly shaped molecules, such as drugs, and constitutes an alternative approximation to determine the interaction energy. The hybrid approach is represented by elements of both equations (1) and (2) and can be effective when a symmetrical molecule is interacting with a molecule comprising asymmetrically Baowan and Hill 3

located atoms. In this case, the interaction energy is given as follows

$$E = \sum_{i} \eta \int \Phi(\rho_{i}) dS \tag{3}$$

where η is the surface density of atoms on the symmetrical molecule, and ρ_i is the distance between a typical surface element dS on the continuously modeled molecule and atom i in the molecule which is modeled as discrete. Again, $\Phi(\rho_i)$ is the potential function, and the energy is obtained by summing overall atoms in the drug or the molecule which is represented discretely.

The continuous approach is an important approximation, and Girifalco et al.⁶ state that

From a physical point of view the discrete atom-atom model is not necessarily preferable to the continuum model. The discrete model assumes that each atom is the center of a spherically symmetric electron distribution while the continuum model assumes that the electron distribution is uniform over the surface. Both of these assumptions are incorrect and a case can even be made that the continuum model is closer to reality than a set of discrete Lennard-Jones centers.

One such example is a C₆₀ fullerene, in which the molecule rotates freely at high temperatures so that the continuous distribution averages out the effect. Qian et al. suggest that the continuous approach is more accurate for the case where the "C nuclei do not lie exactly in the center of the electron distribution, as is the case for carbon nanotubes." However, one of the constraints of the continuous approach is that the shape of the molecule must be reasonably well defined in order to evaluate the integral analytically, and therefore, the continuous approach is mostly applicable to highly symmetrical structures, such as cylinders, spheres, and cones. Hodak and Girifalco⁸ point out that for nanotubes, the continuous approach ignores the effect of chirality, so that effectively nanotubes are only characterized by their diameters. For the graphitebased and C₆₀-based potentials, Girifalco et al.⁶ state that calculations using the continuous and discrete approximations give similar results, such that the difference between equilibrium distances for the atomatom interactions is less than 2%. Hilder and Hill⁹ undertake a detailed comparison of the continuous approach, the discrete atom-atom formulation and a hybrid discrete-continuous formulation, for a range of molecular interactions involving a carbon nanotube, including interactions with another carbon nanotube and the three fullerenes C_{60} , C_{70} , and C_{80} . In the hybrid approach, only one of the interacting molecules is discretized, while the other is considered to be continuous. The hybrid discrete-continuous formulation enables non-regular-shaped molecules to be described and is

particularly useful for drug delivery systems which employ carbon nanotubes as carriers and discussed subsequently. The Hilder and Hill⁹ investigation obtains estimates of the anticipated percentage errors which may occur between the various approaches in a specific application. Although, it is shown that the interaction energies for the three approaches can differ on average by at most 10%, while the forces can differ by at most 5%, with the exception of the C_{80} fullerene. For the C_{80} fullerene, while the intermolecular forces and the suction energies are shown to be in reasonable overall agreement, the pointwise energies may be significantly different. This is perhaps due to the differences in modeling the geometry of the C₈₀ fullerene, noting that the suction energies involve integrals of the energy, and therefore, any error or discrepancy in the pointwise energy tends to be smoothed out to give reasonable overall agreement for the former quantities.

The continuum or continuous approximation has been successfully applied to a number of systems, including the interaction energy between nanostructures of various types and shapes, namely, carbon full-erenes, 6,10,11 carbon nanotubes, 6,12–21 carbon nanotube bundles, 22–24 carbon nanotori, 25–30 carbon nanocones, 31–34 carbon nanostacked cups, 35 fullerene–nanotube, 8,36–46 and TiO₂ nanotubes. 47–49 Moreover, this method has also been used in systems involving proteins and enzymes, 50–52 DNA, 52–55 lipid bilayer and lipid nanotube, 56–58 water molecule, 59–64 benzene, 2,65–69 methane, 2,3,70–75 ions, 75–79 and gas storage and porous aromatic frameworks.

The Lennard-Jones potential function $\Phi(\rho)$ which accounts for the interaction of two non-bonded atoms can be written in the following form

$$\Phi(\rho) = -\frac{A}{\rho^6} + \frac{B}{\rho^{12}} = 4\varepsilon \left[-\left(\frac{\sigma}{\rho}\right)^6 + \left(\frac{\sigma}{\rho}\right)^{12} \right]$$
(4)

where $A = 4\varepsilon\sigma^6$ and $B = 4\varepsilon\sigma^{12}$ are positive constants which are referred to as the Lennard-Jones constants. They are empirically determined and correspond to the constants of attraction and repulsion, respectively. Furthermore, σ is the van der Waals diameter, and ε denotes the energy well depth. The equilibrium distance ρ_0 is given by $\rho_0 = 2^{1/6}\sigma = [(2B)/A]^{1/6}$, where $\varepsilon = A^2/(4B)$, as shown in Figure 1. Moreover, when experimental information on particular atomic interactions is lacking, it is possible to use the so-called empirical combining laws or mixing rules, 89 which have no theoretical basis but are nevertheless used in many calculations. Thus, if the parameters ε and σ are known for the self-interactions of two distinct atomic species designated by 1 and 2, then the parameters for atomic species 1 interacting with atomic species 2 are assumed to be given by the geometric and arithmetic means,

Site-site	σ (Å)	ε (kcal/mol)	A (eVÅ ⁶)	B (eVÅ ¹²)
H	3.1950	0.0152	1.4023	745.8187
0	3.4046	0.0957	12.9264	10,065.7103
N	3.6621	0.0774	16.1917	19,527.3227
С	3.8983	0.0951	28.9469	50,795.2337
В	4.0200	0.0950	34.7736	73,379.6427
Р	4.1500	0.3200	141.7777	362,131.6551
Si	4.2700	0.3100	162.9665	493,896.0409
Ti	4.5400	0.0550	41.7703	182,882.5525
Fe	4.5400	0.0550	41.7703	182,882.5525
Zn	4.5400	0.0550	41.7703	182,882.5525

Table 1. Numerical values for the Lennard-Jones constants taken from Mayo et al. 90

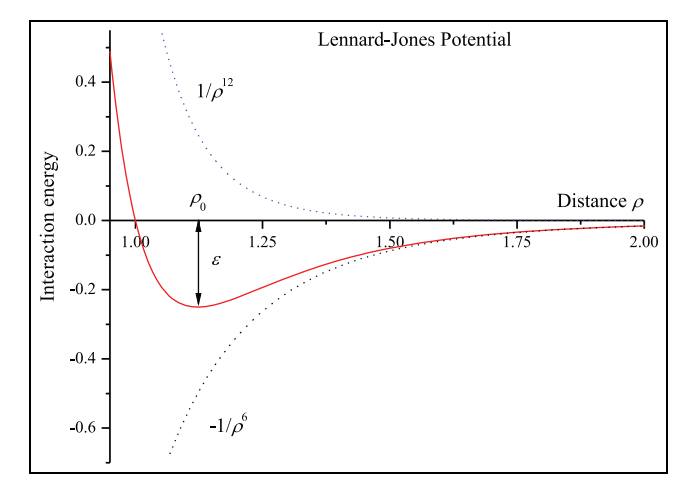


Figure 1. Lennard-Jones potential.

namely, $\varepsilon_{12} = (\varepsilon_1 \varepsilon_2)^{1/2}$ and $\sigma_{12} = (\sigma_1 + \sigma_2)/2$. Following the work by Mayo et al.⁹⁰ and Rappe et al.,⁹¹ some illustrative numerical values for the Lennard-Jones constants are given in Table 1.

When the Lennard-Jones potential function $\Phi(\rho)$ is used in the context of the integral formulation of equation (2), we observe that the attractive term ρ^{-6} and the repulsive term ρ^{-12} can be separated and integrated independently. Furthermore, the two terms only vary in the coefficients A and B and the magnitude of the index, applying to the distance variable ρ . Accordingly, for convenience, the Lennard-Jones potential function $\Phi(\rho)$ is expressed in the following form

$$\Phi(\rho) = -AI_3(\rho) + BI_6(\rho) \tag{5}$$

where $I_n(\rho) = \rho^{-2n}$, and in the following section, integrals of the following form

$$I = \iint_{S_1 S_2} I_n(\rho) dS_2 dS_1 \tag{6}$$

must be evaluated. In many instances, integrals of this type can be given explicitly in terms of the

hypergeometric function F(a, b; c; z) which is a standard function of mathematical analysis that can be readily evaluated from algebraic packages such as Maple and MATLAB. There are many important results relating to the hypergeometric function, and we refer the reader to Erdélyi et al. ⁹² and Bailey, ⁹³ but the principal formula required for the determination of interaction energies is the integral representation

$$F(a,b;c;z) = \frac{\Gamma(c)}{\Gamma(b)\Gamma(c-b)} \int_{0}^{1} t^{b-1} (1-t)^{c-b-1} (1-tz)^{-a} dt$$
(7)

provided that $\Re(c) > \Re(b) > 0$ and $|\arg(1-z)| < \pi$.

Analytical expressions for idealized molecular building blocks

In this section, the approach adopted by Thornton and colleaugues^{80–82} and Lim et al.⁸⁷ is summarized using idealized building blocks to represent the interactions of both simple and more complicated geometries of nanostructures yielding simple and elegant analytical models. First, the analytical representations of the van der Waals interaction between an atom and the building blocks, which are represented by standard geometrical shapes such as points, lines, planes, rings, spheres, and cylinders are determined. At first sight, such a dramatically simplified modeling approach may seem geometrically severe, but in many situations, it has been shown to provide the major contribution to the interaction energy of the actual structure.

Interaction of two atomic points

Given the coordinates of two atoms, $\mathbf{P} = (x_p, y_p, z_p)$ and $\mathbf{Q} = (x_q, y_q, z_q)$, the Lennard-Jones potential between the two atoms can be obtained by substituting the parameter ρ into equation (4) which is the distance between the two atoms and is given as follows

Baowan and Hill 5

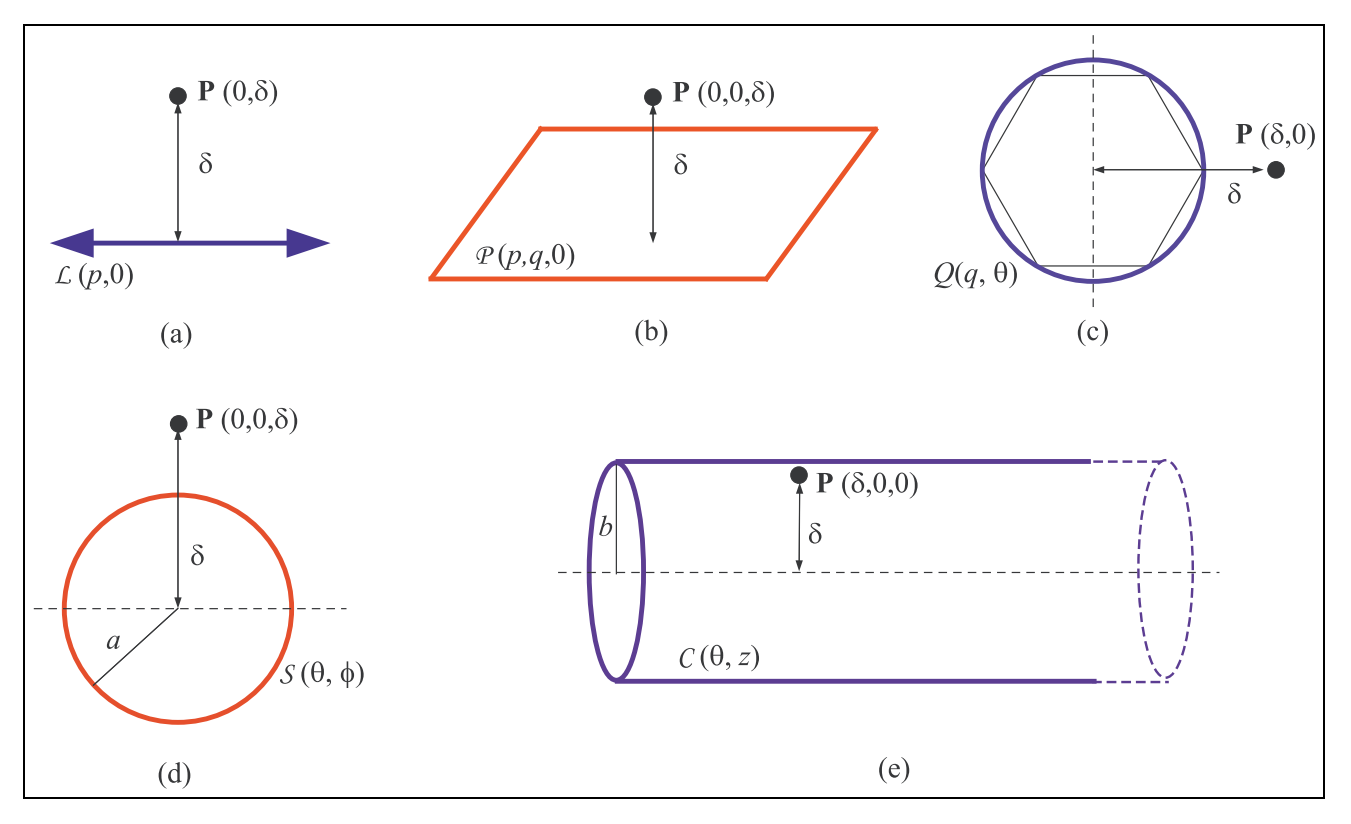


Figure 2. Interaction of atoms with idealized building blocks: (a) point with line, (b) point with plane, (c) point with ring, (d) point with spherical surface, and (e) point with infinitely long right-cylindrical surface.

$$\rho^2 = (x_q - x_p)^2 + (y_q - y_p)^2 + (z_q - z_p)^2$$

Interaction of atomic point with atomic line

The perpendicular (closest) distance between an atomic point and an atomic line is denoted by δ . The line parametrically by $\mathcal{L}(p) = (p,0)a$ and the point $\mathbf{P} = (0,\delta)$ are defined, as illustrated in Figure 2(a). Note that the line element is given by dp, and therefore, the integral of interest is given as follows

$$I = \int_{-\infty}^{\infty} \left(p^2 + \delta^2 \right)^{-n} dp$$

On making a change of variable and substituting $p = \delta \tan \psi$, the integral becomes as follows

$$I = \delta^{1-2n} \int_{-\pi/2}^{\pi/2} \cos^{2n-2} \psi d\psi$$
 (8)

which can then be evaluated using

$$\int_{0}^{\pi/2} \sin^{p} \theta \cos^{q} \theta d\theta = \frac{1}{2} B\left(\frac{p+1}{2}, \frac{q+1}{2}\right)$$
 (9)

to obtain

$$I = \delta^{1-2n}B(n-1/2, 1/2) \tag{10}$$

Interaction of atomic point with atomic plane

This situation is relevant to modeling nanostructures as it corresponds to the case of an individual atom interacting with a graphene sheet. Again, the perpendicular spacing between the point and the plane is assumed to be δ , and therefore, the plane $\mathcal{P}(p,q) = (p,q,0)$ and the point $\mathbf{P} = (0,0,\delta)$ are defined, as shown in Figure 2(b). In this case, the area element of the plane is given by dpdq, and therefore, the integral required to evaluate I is given as follows

$$I = \int_{-\infty}^{\infty} \int_{-\infty}^{\infty} \left(p^2 + q^2 + \delta^2 \right)^{-n} dp dq$$
 (11)

The substitution $p = \sqrt{q^2 + \delta^2} \tan \psi$ is made and proceeded as in the previous section to produce the following

$$I = \mathbf{B}\left(n - \frac{1}{2}, \frac{1}{2}\right) \int_{-\infty}^{\infty} (q^2 + \delta^2)^{1/2 - n} dq$$

On making a further substitution of $q = \delta \tan \phi$, the integral becomes as follows

$$I = \delta^{2-2n} B\left(n - \frac{1}{2}, \frac{1}{2}\right) B\left(n - 1, \frac{1}{2}\right) = \frac{\pi}{(n-1)\delta^{2n-2}}$$

Interaction of atomic point with atomic ring

The interaction of a point with a ring can be categorized into two cases which are as follows: (1) the point is interacting with the ring from the side and (2) the point is interacting with the ring from the top or bottom. For the first case, the point **P** is assumed to be located at $(\delta, 0)$. Furthermore, the center of the ring $Q(q, \theta)$ of radius q is assumed to be located at the origin where its coordinates are $Q = (q \cos \theta, q \sin \theta)$, as depicted in Figure 2(c). With the line element $qd\theta$, equation (6) becomes as follows

$$I = \int_{-\pi}^{\pi} \frac{q}{\left[(q - \delta)^2 + 4q\delta \sin^2 (\theta/2) \right]^n} d\theta$$

On making the substitution $t = \sin^2(\theta/2)$ yields the following

$$I = \frac{2q}{(q-\delta)^n} \int_0^1 t^{-1/2} (1-t)^{-1/2} (1-\mu t)^{-n} dt$$

where $\mu = -4q\delta/(q-\delta)^2$. This integral can be written in a standard hypergeometric form as follows

$$I = \frac{2q}{(q-\delta)^{2n}} \frac{\Gamma(1/2)\Gamma(1/2)}{\Gamma(1)} F\left(n, \frac{1}{2}; 1; \mu\right)$$
$$= \frac{2\pi q}{(q-\delta)^{2n}} F\left(n, \frac{1}{2}; 1; \mu\right)$$

The Pfaff transformation is utilized, ${}^{94}F(a,b;c,z) = (1-z)^{-b}F(c-a,b;c;z/(z-1))$ to produce a terminating hypergeometric series, thus

$$I = \frac{2\pi q}{(q-\delta)^{2n-1}(q+\delta)} F\left(1-n, \frac{1}{2}; 1; \frac{4q\delta}{(q+\delta)^2}\right)$$

In the case of an atomic point **P** with coordinates P = (x, y, z), and assumed to be located either at the top or the bottom of the ring $Q(q, \theta)$, which is assumed to be located at the origin of the *xy*-plane with coordinates $(q \cos \theta, q \sin \theta, 0)$, so that

$$\rho^2 = (x - q\cos\theta)^2 + (y - q\sin\theta)^2 + z^2$$
$$= \beta - \alpha q\cos(\theta - \theta_0)$$

where $\beta = x^2 + y^2 + z^2 + q^2$, $\alpha = \sqrt{x^2 + y^2}$, and $\theta_0 = \arctan(y/x)$. Following the work by Tran-Duc et al., ⁶⁷I becomes as follows

$$I = \int_{-\pi}^{\pi} \frac{q}{\left[\beta - \alpha q \cos\left(\theta - \theta_{0}\right)\right]^{n}} d\theta$$

$$= \frac{2\pi q}{\left(\beta - \alpha q\right)^{n}} F\left(n, \frac{1}{2}; 1; \frac{2\alpha q}{(\alpha q - \beta)}\right)$$
(12)

Interaction of atomic point with atomic spherical surface

The atomic point with Cartesian coordinates $\mathbf{P} = (0, 0, \delta)$ is considered, which is at a distance δ from the center of an atomic spherical surface of radius a, parameterized using the spherical coordinates $S(\theta, \phi) = (a, \theta, \phi)$, as indicated in Figure 2(d). In terms of these coordinates, the integral required to evaluate equation (6) is given as follows

$$I = a^2 \int_{-\pi}^{\pi} \int_{0}^{\pi} \frac{\sin \theta}{\left[a^2 \sin^2 \theta + (a \cos \theta - \delta)^2\right]^n} d\theta d\phi$$

Since the integrand in this case is independent of ϕ , the integration involving ϕ can be effected immediately and then by re-organizing the denominator to deduce

$$I = 2\pi a^2 \int_{0}^{\pi} \frac{\sin \theta}{\left[\delta^2 + a^2 - 2\delta a \cos \theta\right]^n} d\theta \tag{13}$$

which on making the substitution $t = \delta^2 + a^2 - 2\delta a \cos \theta$ becomes as follows

$$I = \frac{\pi a}{\delta} \int_{(\delta - a)^2}^{(\delta + a)^2} \frac{dt}{t^n} = \frac{\pi a}{\delta (1 - n)} \left[\frac{1}{t^{n-1}} \right]_{(\delta - a)^2}^{(\delta + a)^2}$$
$$= \frac{\pi a}{\delta (n - 1)} \left[\frac{1}{(\delta - a)^{2(n-1)}} - \frac{1}{(\delta + a)^{2(n-1)}} \right]$$

Interaction of atomic point with infinite atomic cylindrical surface

Here, the interaction of an arbitrary atomic point **P** with an atomic cylindrical surface \mathcal{C} of radius b and assumed to be infinite in length is determined. The cylinder is represented parametrically by the coordinates $\mathcal{C}(\theta,z)=(b,\theta,z)$, where $-\pi < \theta \le \pi$ and $-\infty < z < \infty$. Due to the rotational and translational symmetry of the problem, the point **P** in Cartesian coordinates is given by $(\delta,0,0)$, where $0 \le \delta < b$, as indicated in Figure 2(e). Accordingly, the distance from **P** to a typical surface element on \mathcal{C} is given as follows

$$\rho^{2} = (b\cos\theta - \delta)^{2} + b^{2}\sin^{2}\theta + z^{2}$$
$$= \delta^{2} + b^{2} - 2\delta b\cos\theta + z^{2}$$
$$= (b - \delta)^{2} + 4\delta b\sin^{2}(\theta/2) + z^{2}$$

Baowan and Hill 7

so that, the following integral must be evaluated

$$I = b \int_{-\infty - \pi}^{\infty} \frac{\pi}{\left[(b - \delta)^2 + 4\delta b \sin^2 \left(\frac{\theta}{2} \right) + z^2 \right]^n} d\theta dz$$

By defining $\lambda^2 = (b - \delta)^2 + 4\delta b \sin^2(\theta/2)$ and making the substitution $z = \lambda \tan \psi$ gives the following

$$I = b \int_{-\pi/2}^{\pi/2} \cos^{2n-2} \psi d\psi \int_{-\pi}^{\pi} \frac{1}{\lambda^{2n-1}} d\theta$$
$$= bB \left(n - \frac{1}{2}, \frac{1}{2} \right) \int_{-\pi}^{\pi} \frac{1}{\lambda^{2n-1}} d\theta$$

Now on making the further substitution $t = \sin^2(\theta/2)$ yields the following

$$I = \frac{2b}{(b-\delta)^{2n-1}} B\left(n - \frac{1}{2}, \frac{1}{2}\right)$$

$$\times \int_{0}^{1} t^{-1/2} (1-t)^{-1/2} (1-\mu t)^{1/2-n} dt$$
(14)

where $\mu = -4b\delta/(b-\delta)^2$. This integral is now in the Euler form as follows

$$\begin{split} I &= \frac{2b}{(b-\delta)^{2n-1}} B\bigg(n - \frac{1}{2}, \frac{1}{2}\bigg) \frac{\Gamma(1/2)\Gamma(1/2)}{\Gamma(1)} \\ &\times F\bigg(n - \frac{1}{2}, \frac{1}{2}; 1; \mu\bigg) \\ &= \frac{2\pi b}{(b-\delta)^{2n-1}} B\bigg(n - \frac{1}{2}, \frac{1}{2}\bigg) F\bigg(n - \frac{1}{2}, \frac{1}{2}; 1; \mu\bigg) \end{split}$$

Note that in terms of the usual parameters of the hypergeometric function where c=2b, and by employing a quadratic transformation (see Erdélyi et al. 92 equation (24) on page 64), the integral I yields the following

$$\begin{split} I &= \frac{2\pi b}{(b-\delta)^{2n-1}} B\bigg(n - \frac{1}{2}, \frac{1}{2}\bigg) \bigg(\frac{b-\delta}{b}\bigg)^{2n-1} \\ &\times F\bigg(n - \frac{1}{2}, n - \frac{1}{2}; 1; \frac{\delta^2}{b^2}\bigg) \\ &= \frac{2\pi}{b^{2n-2}} B\bigg(n - \frac{1}{2}, \frac{1}{2}\bigg) F\bigg(n - \frac{1}{2}, n - \frac{1}{2}; 1; \frac{\delta^2}{b^2}\bigg) \end{split}$$

Next, the total interaction of an atomic point P, which is offset from the axis by a distance δ , and a cylindrical surface \mathcal{C} of radius b are considered where $\delta > b$. In this case, the calculation follows along similar lines to the above except that the terms are rearranged so as to pick up a different solution of the

hypergeometric equation, which is a solution with the argument inverse to that given in the previous section.

The same cylinder defined in cylindrical coordinates by $C(\theta, z) = (b, \theta, z)$, where $-\pi < \theta \le \pi$, and $-\infty < z < \infty$ is determined. The atomic point with Cartesian coordinates $\mathbf{P} = (\delta, 0, 0)$ is defined, but in this case, $\delta > b$. Following the above steps, an expression for the distance ρ , from the point \mathbf{P} to an arbitrary area element on the surface of the cylinder C is as follows

$$\rho^{2} = (\delta - b)^{2} + 4\delta b \sin^{2}(\theta/2) + z^{2}$$

In a similar manner to that described above, the integral *I* is of the following form

$$I = \frac{2\pi b}{(\delta - b)^{2n-1}} B\left(n - \frac{1}{2}, \frac{1}{2}\right) F\left(n - \frac{1}{2}, \frac{1}{2}; 1; -\frac{4\delta b}{(\delta - b)^2}\right)$$

whereupon on again employing the quadratic transformation

$$I = \frac{2\pi b}{\delta^{2n-1}} B\bigg(n - \frac{1}{2}, \frac{1}{2}\bigg) F\bigg(n - \frac{1}{2}, n - \frac{1}{2}; 1; \frac{b^2}{\delta^2}\bigg)$$

Some important mathematical formulae are derived which may be exploited to calculate the interaction energy between two nanostructures. Analytical expressions for an atomic point (i.e. a single atom) with various shaped molecules have been determined. In more complicated atomic configurations involving two or more molecules, another surface integral of the atomic point must be evaluated to determine the total interaction energy of the system. In the following sections, a number of nanotechnology applications are surveyed which have exploited these formulae to determine the properties of the systems.

Mechanics of nanostructures

Nanostructures such as carbon nanotubes, nanopeapods, nanocones, and carbon onions exhibit outstanding physical and mechanical properties such as their high strength, high flexibility, and low weight, and they provide a basis for the creation of many novel nanodevices. One particular application which has attracted much attention is the nano-oscillator, 12,37,95,96 which is able to generate frequencies in the gigahertz range, 12 and which may form the basis of a number of ultrahigh-frequency devices in the computer industry. Since the discovery of ultra low friction by Cumings and Zettl, 95 double-walled carbon nanotube oscillators have been widely studied using both molecular dynamics simulations and experiments. 12,13,96-98 In addition, carbon nanotubes have received much attention for medical applications, especially their use as nanocontainers for drug and gene delivery. In particular, a well-known self-assembled hybrid carbon nanostructure, so-called nanopeapods, may be regarded as a model for possible drug carriers, where the carbon nanotube can be thought of as the nanocontainer, and the C₆₀ molecular chain can be considered as the drug molecule. ⁹⁹ Nanocones have received less attention in the literature, primarily because only a small amount are produced in the production process. ¹⁰⁰ However, the narrow vertex of the cone makes an ideal candidate as a nanoprobe in scanning tunneling microscopes. ¹⁰¹

The Lennard-Jones potential together with the continuous approximation has been successfully employed in a number of studies to determine the van der Waals interaction energy and the force between two interacting non-bonded nanostructures. In particular, several authors determine the molecular interaction between a fullerene and carbon nanotubes. 8,36-46 Girifalco³⁶ determines the interaction energy between two C₆₀ fullerenes and extends the study in Girifalco et al.6 to find the energy between two identical parallel carbon nanotubes of infinite length and between a carbon nanotube and a C₆₀ fullerene. Girifalco et al.⁶ also provide the value of the interaction constants in the Lennard-Jones potential for carbon atoms in graphene-graphene, C₆₀-C₆₀, and C₆₀-graphene. Furthermore, Hodak and Girifalco⁸ propose an energy formula for universal graphitic systems including the interaction of an ellipsoid inside a single-walled carbon nanotube. In general, it is possible to combine both the continuous and discrete approaches to model the interaction between two nanostructures. As shown in both Hilder and Hill⁹ and Verberck and Michel, 102 the single-walled carbon nanotube is modeled continuously, while the fullerene is modeled as a discrete atomic structure.

Cox et al.^{38,39} have proposed the important notions of suction and acceptance energies for the encapsulation behavior of an atom and a C₆₀ fullerene when sucked inside a carbon nanotube. The suction energy is defined as the total work performed by the van der Waals interactions on an atom or molecule entering the carbon nanotube. The acceptance energy is the total work performed by van der Waals interactions on the atom or molecule entering the nanotube, up to the point that the van der Waals force once again becomes attractive. 38 The forces acting on the atom or a C_{60} fullerene interacting with carbon nanotube of finite length can be approximated by two equal and opposite Dirac delta functions operating at the extremities of the tubes. as shown in Figure 3. Once the atom or molecule is encapsulated inside the tube, these forces tend to keep them oscillating inside, and this is the physical basis of the nano-oscillator.

Cox et al. 40,43,44 also study the mechanics of spherical and spheroidal fullerenes entering carbon nanotubes. Particularly, Figure 4 shows the energy profiles for spheroidal C₇₀ and C₈₀ fullerenes interacting with carbon nanotubes for various offset distances ε and tilt angles ψ , and two distinct and approximately equal local minima are observed. Baowan et al.42 determine the encapsulation mechanics of the C₆₀ into a carbon nanotube where the C_{60} is initiated outside the tube in the absence of any applied external forces.⁴² Once a number of C₆₀ fullerenes are encapsulated inside the tube, two patterns emerge which are termed zigzag and spiral, 41 and the composite nanostructures are referred to as nanopeapods. Moreover, the spiral motion of carbon atoms and C₆₀ fullerenes inside single-walled carbon nanotubes is investigated by Chan et al.45 and Chan and Hill.46

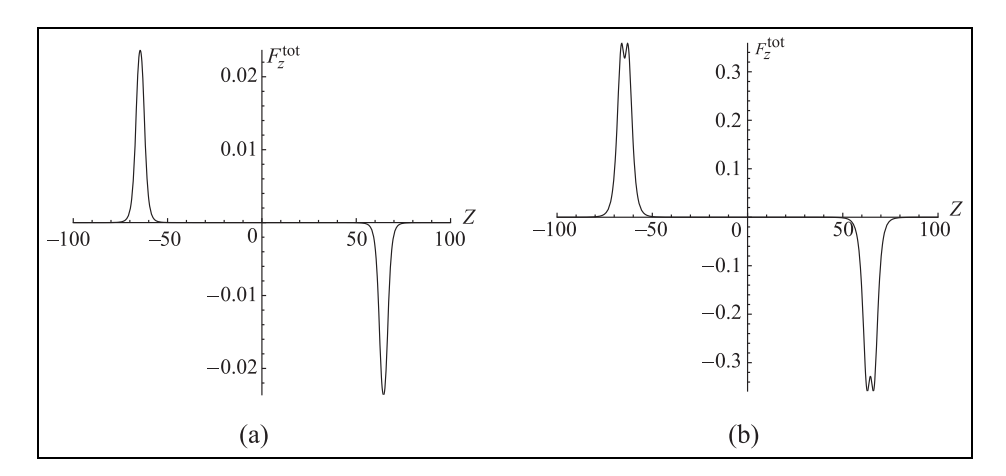


Figure 3. Plot of forces for (a) atom oscillating inside (6, 6) carbon nanotube and (b) C_{60} fullerene oscillating inside (10, 10) carbon nanotube.

Schematic representation reproduced from Cox et al.³⁹ (authors are allowed to re-use parts of their own work in derivative works without seeking the Royal Society's permission).

Baowan and Hill 9

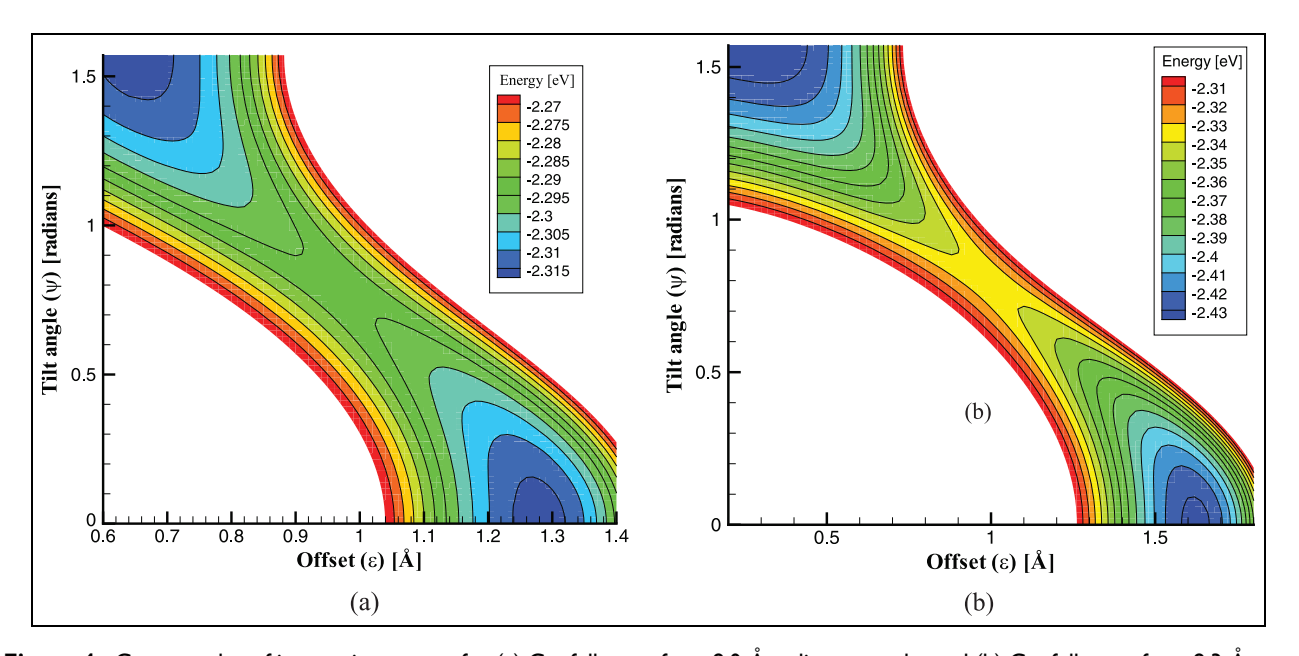


Figure 4. Contour plot of interaction energy for (a) C₇₀ fullerene for a 8.0-Å radius nanotube and (b) C₈₀ fullerene for a 8.3-Å radius nanotube, showing two distinct and approximately equal local minima. Schematic representation reproduced from Cox et al.⁴⁴ (DOI:10.1088/1751-8113/41/23/235209) ©IOP Publishing. Reproduced by permission of IOP Publishing. All rights reserved.

For two concentric cylindrical carbon nanotubes, Zheng and Jiang¹² determine the van der Waals restoring force between the inner and outer shells of a multiwalled carbon nanotube and subsequently predict a gigahertz frequency of the oscillatory motion. Baowan and colleagues 14,15 determine analytical expressions for the suction energy and offset configurations of doublewalled carbon nanotubes and also predict the gigahertz frequency for the nanotube oscillators. A similar approach has been adopted by Cox¹⁶ to model the behavior of forced double-walled nanotube oscillators. Ansari and colleagues^{18–20} consider the effects of geometrical parameters on the force distributions for the oscillatory behavior of double-walled carbon nanotubes. The effect of capped ends of double-walled carbon nanotubes is also studied by Baowan, 17 and the effect of tube radii is investigated by Tiangtrong and Baowan.²¹

Ruoff and Hickman¹⁰³ consider the interaction between a spherical fullerene and a graphite sheet. For spherical carbon onions $C_{N_1}@C_{N_2}$ ($N_2 > N_1$), Iglesias-Groth et al.¹⁰⁴ also adopt the Lennard-Jones potential and the continuous approximation to determine the interlayer interaction. Using the formula of Iglesias-Groth et al.,¹⁰⁴ Guérin¹⁰⁵ obtains the interaction energy between the interlayer of carbon onions which is in excellent agreement to that obtained from a discrete atom–atom summation model given in Lu and Yang.¹⁰⁶ Furthermore, Baowan et al.¹⁰ predict the interlayer spacing for each shell of the carbon onions. Moreover, they observe that the equilibrium spacing

decreases as the shell is further away from the inner core, and this is due to the decreasing curvature for larger spheroids. Thamwattana et al. 11 also exploit the Lennard-Jones potential and the continuous approximation to focus on various interactions involving a full-erene and other carbon nanostructures, and analytical expressions are obtained. The study by Thamwattana et al. 11 confirms that molecules are likely to be at a certain distance apart in order to minimize the total interaction energy.

Henrard et al.¹⁰⁷ use a similar technique to that proposed by Girifalco³⁶ and obtain the potential for bundles of single-walled carbon nanotubes. Cox and colleagues^{22–24} study extensively the mechanics of carbon atoms and nanotubes oscillating in carbon nanotube bundles and again utilizing the Lennard-Jones potential together with the continuous approximation, and the results obtained can be used to predict the oscillator bundle configuration which optimizes the suction energy and therefore leads to the maximum frequency oscillator.

The equilibrium configurations of carbon atoms and C₆₀ fullerenes inside carbon nanotori have been determined by Hilder and Hill,^{25–27} Chan and colleagues,^{28,29} and Sumetpipat et al.³⁰ Even though complicated analytical expressions are derived, the energy profiles are easily obtained utilizing algebraic packages such as Maple. Furthermore, the interaction energy between two nanocones has been investigated by Baowan and Hill^{31–33} and Ansari et al.,³⁴ where the spacing between the two cone surfaces is determined to be 3 Å. The

equilibrium arrangement between two carbon nanostacked cups, which are truncated cones that are found as the hollow cores of carbon nanofibers, ^{108–112} is determined by Baowan et al.³⁵ again using the Lennard-Jones potential and the continuous approach.

MOFs and gas storage

MOFs comprise metal atoms or clusters that are linked periodically by organic molecules to establish an array such that each atom forms part of an internal surface. MOFs have delivered the highest surface areas and hydrogen storage capacities for any physisorbent and are shown to be the most practically promising material for gas storage. ¹¹³ Exposed metal sites ^{114,115} pore sizes, ¹¹⁶ and ligand chemistries ^{117,118} have been found to be the most effective routes for increasing the hydrogen enthalpy of adsorption within MOFs. The MOF adsorbent that presently holds the record for gravimetric hydrogen storage capacity at room temperature is the first structurally characterized beryllium-based framework, Be-BTB (benzene tribenzoate). Be-BTB has a Brunauer–Emmett–Teller (BET) ¹¹⁹ surface area of 4400 m²g⁻¹ and can adsorb 2.3 wt% hydrogen at 298 K and 100 bar. ¹²⁰ We refer the reader to Furukawa et al. ¹²¹ for a comprehensive review of the chemistry and the applications of MOFs.

The so-called Topologically Integrated Mathematical Thermodynamic Adsorption Model (TIMTAM), as proposed by Thornton and colleagues, 81,82 assumes the ideal building blocks described in the section on analytical expressions for idealized molecular building blocks to represent the cavity of the structure, and then, these expressions are exploited to calculate the potential energy interactions between the gas and the adsorbate. The major advantage of the TIMTAM approach is that it provides analytical formulae that are computationally instantaneous, and therefore, many distinct scenarios can be rapidly investigated which evidently serves to accelerate material design.⁸¹ A schematic representation for MgC₆₀@MOF for a MOF cavity impregnated with magnesium-decorated C_{60} is shown in Figure 5, where the TIMTAM model is utilized to determine the energy level in the cavity for the magnesium atom. 81 Moreover, the same approach has also been proved as a useful technique to investigate the effect of pore size in MOFs. 80–82,86,87

Furthermore, Chan and Hill⁸⁴ investigate the storage of hydrogen molecules inside graphene-oxide frameworks comprising two parallel graphenes rigidly separated by perpendicular ligands. These authors find 6.33 wt% for GOF-28 at a temperature of 77 K and a pressure of 1 bar which is consistent with several experimental and other computational results. Based on the assumption of no steric hindrance and a small

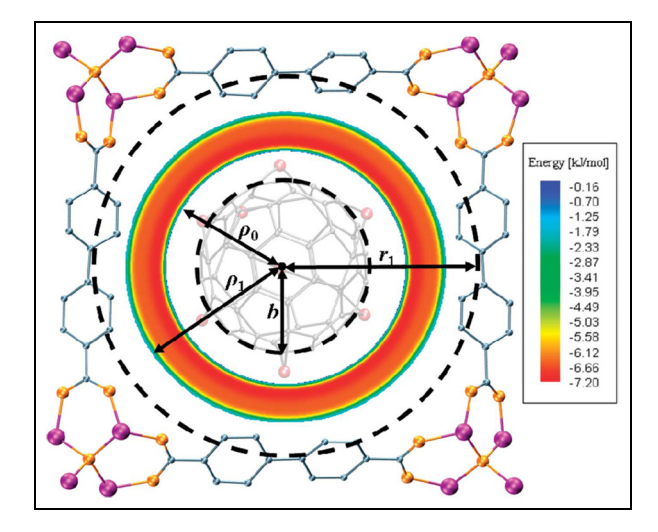


Figure 5. Model for $C_{60}@MOF$ where Mg atom locates within cavity surface at radius r_1 , ρ is distance between gas molecule and center of cavity, and b denotes radius of C_{60} . The color bar indicates the energy value of Mg $C_{60}@MOF$. Reprinted with permission from Thornton et al. Copyright 2009 American Chemical Society.

electronic barrier, Chan and Hill⁸³ model the interaction of a rigidly suspended benzene molecule within a MOF, which is then used as a building block in more complex MOFs.

For the specific gas molecule, benzene, Tran-Duc and colleagues^{65–69} extensively investigate the equilibrium configuration of benzene dimer adsorbed on graphene sheet, C₆₀ fullerene, and carbon nanotubes. They obtain an analytical expression as a function of the distance between the gas molecule and the material surfaces and the rotational configuration of the benzene itself. This analysis might be exploited to improve the design of the gas storage system.⁶⁹ For methane, Adisa et al.^{1,2,70–73} investigate the encapsulation and packing of methane in various carbon nanostructures such as spherical fullerenes, nanotubes, and nanobundles. In terms of clean energy and the effect on the environment, the theoretical study⁷³ indicates a promising future using natural gas storage in molecular structures.

Molecular selective and separation

Water molecule has a simple chemical structure and is often a basic unit in many biomolecules. The determination of water separation can be envisaged as the first step in a study of the selective separation of more complicated molecules. Hilder and Hill⁵⁹ determine the maximum velocity for a single water molecule entering a carbon nanotube, and their model predicts that the radius of the carbon nanotube must be at least 3.464 Å

Baowan and Hill

for acceptance of a water molecule, and that a radius of 3.95 Å provides the maximum uptake or suction energy. Chan and Hill⁶¹ utilize the same mathematical technique to investigate the transport of water through carbon nanotubes and suggest that their results rapidly reduce the computational time for the full numerical calculation. As an alternative for molecular selectivity, Garalleh et al.⁶²⁻⁶⁴ determine the interaction energy between water and various other biomolecules.

Ions are atoms or molecules in which the total number of electrons does not equal the total number of protons, giving the atom a net positive or negative electrical charge. On using the applied mathematical approach, Chan and Hill^{75,76} investigate the interaction energy between various types of atoms and ions, namely, Mn²⁺, Au, Pt, Na¹⁺, and Li¹⁺ on graphene sheet. These authors determine the equilibrium position for the atom/ion on the surface of the graphene sheet and the minimum intermolecular spacing between two graphene sheets. Furthermore, carbon nanotubes have been used to facilitate the transport and separation of atoms and ions. 77,78 Similarly, Rahmat et al. 79 determine the suction and the acceptance behavior of C₆₀ molecule, Li⁺, Na⁺, Rb⁺, and Cl⁻ ions and ionwater clusters into peptide nanotubes. A critical tube radius of 8.5 Å is determined such that all the ions are accepted into the peptide nanotubes, whereas the C_{60} is

rejected. This work has many potential applications involving ion separation, including drug delivery systems and high-performance alkali batteries using nanomaterials as components.

The selective separation of biomolecules is a critical process in food, biomedical, and pharmaceutical industries. Baowan and Thamwattana⁵⁰ utilize the Lennard-Jones potential function and the continuous approximation to separate trypsin and lysozyme using mesoporous silica. These authors predict that the silica pores with radii lying in the range 17.23 and 21.24 Å will only allow lysozyme to be encapsulated. Using the same approach, Thamwattana et al.⁵¹ investigate three model configurations for bovine serum albumin to be encapsulated inside carbon nanotubes, as indicated in Figure 6. They conclude that a critical radius of pore or tube is crucial for the design to facilitate maximum loading of proteins and drug molecules.

The far more complicated biomolecule DNA has been examined by Alshehri et al., 52-55 who determine equilibrium positions of a DNA strand absorbed onto a graphene sheet or encapsulated inside a carbon nanotube. These authors find that a space of approximately 20 Å is required for the absorption of DNA onto the graphene sheet. 53 Moreover, they observe that double-stranded DNA is encapsulated inside a single-walled carbon nanotube of radius larger than 12.30 Å, and

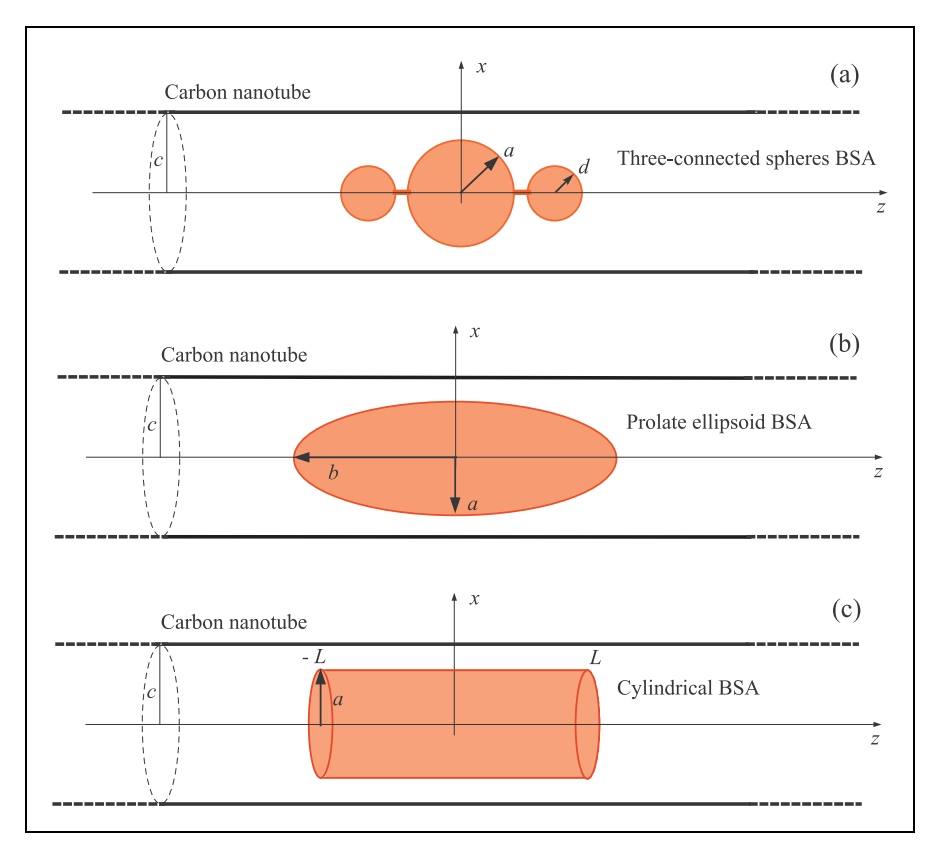


Figure 6. Three possible configurations for bovine serum albumin encapsulated in a carbon nanotube and modeled: (a) as three-connected spheres, (b) as a prolate-ellipsoid, and (c) as a right-cylinder.

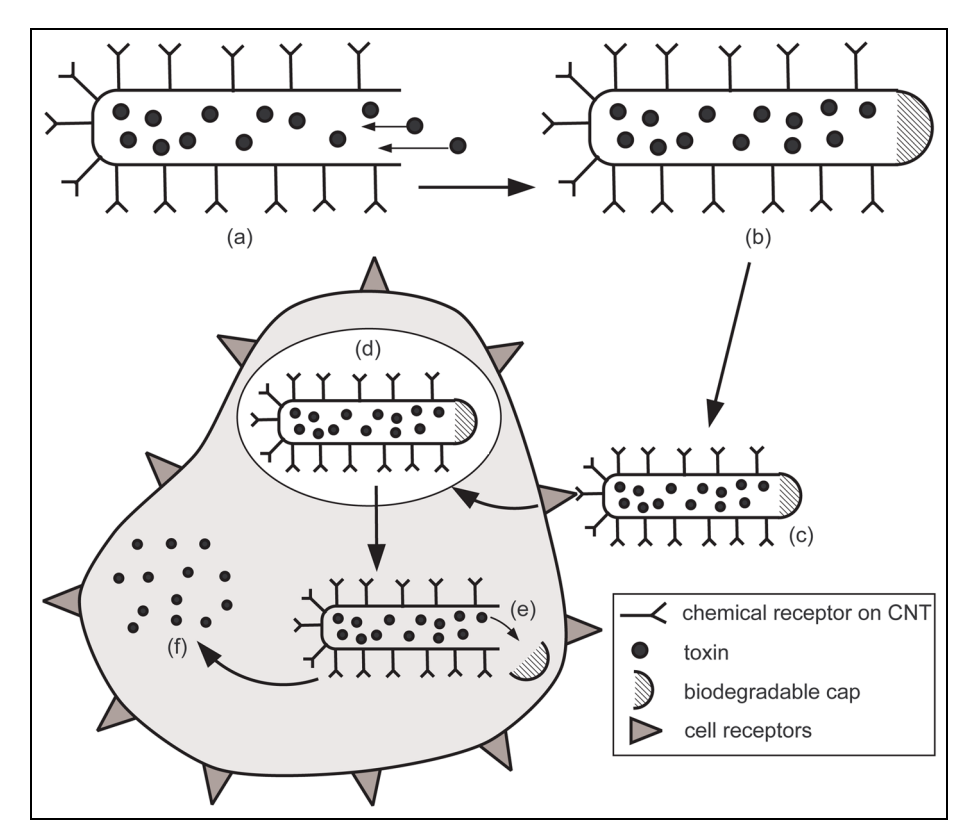


Figure 7. Outline of proposed drug delivery process: (a) nanotube surface is functionalized with a chemical receptor and drug molecules are encapsulated, (b) open end is capped, (c) nanocapsule is ingested and locates to target site due to functionalized surface, (d) cell internalizes capsule, for example, by receptor-mediated endocytosis, (e) cap is removed or biodegrades inside cell, and (f) drug molecules are released.

Schematic representation reproduced with permission from Hilder and Hill.¹³¹ Copyright 2009 Wiley-VCH Verlag GmbH & Co. KGaA, Weinheim.

they show that the optimal radius of the single-walled carbon nanotube to enclose a double-stranded DNA is 12.8 Å. 52,54,55 Furthermore, since lipid bilayers, lipid nanotubes, and liposomes are potential candidates for use in molecular separation, Baowan et al. 56 determine the penetration and encapsulation of C₆₀ fullerene through/in lipid bilayer family. Furthermore, the penetration and encapsulation of silica nanoparticles are examined in Baowan et al. 57 and silver and gold nanoparticles in Baowan and Thamwattana. 58 Although electrostatic interaction energy may arise from hydrophobic layers of the lipid, these authors show that the dominant energy contribution originates from the van der Waals interactions.

Targeted drug delivery

The prospect that nanocapsules may realize the "magic bullet" concept, as first proposed at the beginning of the 20th century by the Nobel Prize winner Paul Ehrlich (1854–1915), generated immense interest in their development. The ideal drug carrier, or "magic bullet," is envisaged as a transporter of drugs or other molecular cargo to a specific site in the body which then

unloads the cargo in a controlled manner. Although this notion may sound like science fiction, the advent of nanotechnology means that it is rapidly becoming scientific fact. Despite the prominence of carbon nanotubes in the broader area of nanotechnology, the field of nanotube biotechnology is in its infancy, and there is still much work that needs to be accomplished before specific products can be produced. Drug delivery is one of the most promising biomedical applications of nanotechnology, and as stated by Hillebrenner et al.¹²⁵ in a review of template-synthesized nanotubes for biomedical delivery applications, "The future challenges for nanotubes as drug delivery vehicles are substantial but not insurmountable."

Again following the Lennard-Jones potential function and the continuous approximation approach, Hilder and Hill determine the energy behavior and suction characteristics in the encapsulation of various drugs into nanotubes including cisplatin, 126,127 paclitaxel, and doxorubicin 128 and into other nanotubes such as boron nitride, silicon, and boron carbide. 129 Their results predict an appropriate tube size that gives rise to the optimum encapsulation mechanics for a prescibed drug molecule. Moreover, Hilder and Hill 130

Baowan and Hill

also examine nanosyringes comprising double-walled carbon nanotubes to inject DNA or anticancer drugs directly into the cell. The reader is referred to Hilder and Hill¹³¹ for a comprehensive review on the various models for drug release using a nanotube carrier, as indicated in Figure 7. Ansari et al.¹³² employ both a hybrid discrete–continuum model and molecular dynamics simulation to study the offset of cisplatin in a single-walled carbon nanotube and conclude that the methods give comparable results.

Summary

This review has focused on the use of applied mathematical modeling to determine the mechanical energy behavior of nanostructures. We have concentrated on those applications for which the 6-12 Lennard-Jones potential energy function and the continuous approximation apply. The continuous approximation assumes that the total molecular interaction energy of the system involving a discrete atomic configuration can be approximated by a uniform distribution of atoms, either throughout a region or over a bounding surface. First, analytical expressions for various molecular building blocks are evaluated to provide the major contribution to the interaction energy of the actual complicated atomic configuration. The principal mechanical properties of the nanostructure can then be determined from the energy distribution, which gives rise to the force distribution, equilibrium configurations, and oscillatory behavior. Moreover, this applied mathematical approach has been illustrated to determine the gas storage characteristics of MOFs. The same approach has also been successfully applied to both organic and inorganic molecules, including systems of biomolecules involving protein and enzyme selective separation and targeted drug delivery. In summary, although this robust mathematical approach has already been successfully exploited in many applications, its most important future role will likely be either as a component or as the first iteration in large-scale computational calculations to determine the molecular interaction energy of complex atomic configurations, and such use will significantly increase computational efficiency.

Acknowledgements

The authors gratefully acknowledge the Endeavour Research Scheme for the provision of two postdoctoral fellowships for D.B. D.B. is also grateful for the support of the Thailand Research Fund (RSA5880003). The authors also wish to acknowledge all their numerous colleagues involved in this work.

Declaration of conflicting interests

The author(s) declared no potential conflicts of interest with respect to the research, authorship, and/or publication of this article.

Funding

The author(s) disclosed receipt of the following financial support for the research, authorship, and/or publication of this article: Much of the research was supported by the Australian Research Council.

References

- Adisa OO, Cox BJ and Hill JM. Encapsulation of methane in nanotube bundles. *Micro Nano Lett* 2010; 5: 291–295.
- Adisa OO, Cox BJ and Hill JM. Methane storage in spherical fullerenes. J Nanotechnol Eng Med 2013; 3: 041002.
- 3. Van der Giessent E and Needleman A. Discrete dislocation plasticity: a simple planar model. *Model Simul Mater Sc* 1995; 3: 689–735.
- Biner SB and Morris JR. A two-dimensional discrete dislocation simulation of the effect of grain size on strengthening behaviour. *Model Simul Mater Sc* 2002; 10: 617–635.
- Ericksen JL. On the Cauchy–Born rule. Math Mech Solids 2008; 13: 199–220.
- Girifalco LA, Hodak M and Lee RS. Carbon nanotubes, buckyballs, ropes, and a universal graphitic potential. *Phys Rev B* 2000; 62: 13104–13110.
- Qian D, Liu WK, Subramoney S, et al. Effect of interlayer potential on mechanical deformation of multiwalled carbon nanotubes. *J Nanosci Nanotechno* 2003; 3: 185–191.
- Hodak M and Girifalco LA. Fullerenes inside carbon nanotubes and multi-walled carbon nanotubes: optimum and maximum sizes. Chem Phys Lett 2001; 350: 405–411.
- Hilder TA and Hill JM. Continuous versus discrete for interacting carbon nanostructures. *J Phys A: Math Theor* 2007; 40: 3851–3868.
- Baowan D, Thamwattana N and Hill JM. Continuum modelling of spherical and spheroidal carbon onions. *Eur Phys J D* 2007; 44: 117–123.
- Thamwattana N, Baowan D and Hill JM. Continuum modelling for interactions between fullerenes and other carbon nanostructures. *J Comput Theor Nanos* 2009; 6: 972–984.
- Zheng Q and Jiang Q. Multiwalled carbon nanotubes as gigahertz oscillators. *Phys Rev Lett* 2002; 88: 045503.
- 13. Zheng Q, Liu JZ and Jiang Q. Excess van der Waals interaction energy of a multiwalled carbon nanotube with an extruded core and the induced core oscillation. *Phys Rev B* 2002; 65: 245409.
- Baowan D and Hill JM. Force distribution for doublewalled carbon nanotubes and gigahertz oscillators. Z Angew Math Phys 2007; 58: 857–875.

- Baowan D, Thamwattana N and Hill JM. Suction energy and offset configuration for double-walled carbon nanotubes. *Commun Nonlinear Sci* 2008; 13: 1431–1447.
- Cox BJ. Model and behaviour of forced double-walled nanotube oscillators. *Dynam Cont Dis Ser B* 2012; 19: 543–557.
- 17. Baowan D. On the effect of capping the ends of carbon nanotubes used for drug delivery. *Dynam Cont Dis Ser B* 2012; 19: 613–619.
- Ansari R and Motevalli B. On new aspects of nested carbon nanotubes as gigahertz oscillators. J Vib Acoust 2011; 133: 051003.
- Ansari R and Motevalli B. The effects of geometrical parameters on force distributions and mechanics of carbon nanotubes: a critical study. *Commun Nonlinear Sci* 2009; 14: 4246–4263.
- Ansari R, Rajabiehfard R and Arash B. Thermal buckling of multiwalled carbon nanotubes using a semianalytical finite element approach. *J Therm Stresses* 2011; 34: 817–834.
- Tiangtrong P and Baowan D. Encapsulation behaviours of nanoparticles entering two-section carbon nanotubes. *J Math Chem* 2014; 52: 489–503.
- Cox BJ, Thamwattana N and Hill JM. Mechanics of fullerenes oscillating in carbon nanotube bundles. *J Phys A: Math Theor* 2007; 40: 13197–13208.
- Cox BJ, Thamwattana N and Hill JM. Mechanics of nanotubes oscillating in carbon nanotube bundles. P Roy Soc A: Math Phy 2008; 464: 691–710.
- 24. Thamwattana N, Cox BJ and Hill JM. Oscillation of carbon molecules inside carbon nanotube bundles. *J Phys: Condens Mat* 2009; 21: 144214.
- 25. Hilder TA and Hill JM. Oscillating carbon nanotori along carbon nanotubes. *Phys Rev B* 2007; 75: 125415.
- Hilder TA and Hill JM. Orbiting atoms and C₆₀ fullerenes inside carbon nanotori. J Appl Phys 2007; 101: 064319.
- Hilder TA and Hill JM. Orbiting nanosectors inside carbon nanotori. Micro Nano Lett 2007; 2: 50–53.
- Chan Y, Thamwattana N, Cox GM, et al. Mechanics of nanoscale orbiting systems. *J Math Chem* 2009; 46: 1271–1291.
- Chan Y, Cox BJ and Hill JM. Carbon nanotori as traps for atoms and ions. *Physica B* 2012; 407: 3479–3483.
- 30. Sumetpipat K, Lee RKF, Cox BJ, et al. Carbon nanotori and nanotubes encapsulating carbon atomic-chains. *J Math Chem* 2014; 52: 1817–1830.
- Baowan D and Hill JM. Nested boron nitride and carbon-boron nitride nanocones. *Micro Nano Lett* 2007; 2: 46–49.
- 32. Baowan D and Hill JM. Equilibrium locations for nested carbon nanocones. *J Math Chem* 2008; 43: 1489–1504.
- Baowan D and Hill JM. Gigahertz oscillators constructed from carbon nanocones inside carbon nanotubes. *J Com*put Theor Nanos 2008; 5: 302–310.
- Ansari R, Alisafaei F, Alipour A, et al. On the van der Waals interaction of carbon nanocones. *J Phys Chem Solids* 2012; 73: 751–756.
- 35. Baowan D, Cox BJ and Hill JM. Equilibrium configurations for carbon nano-stacked cups. *J Comput Theor Nanos* 2011; 8: 616–623.

- 36. Girifalco LA. Molecular properties of fullerene in the gas and solid phases. *J Phys Chem* 1992; 96: 858–861.
- Qian D, Liu WK and Ruoff RS. Mechanics of C₆₀ in nanotubes. *J Phys Chem B* 2001; 105: 10753–10758.
- Cox BJ, Thamwattana N and Hill JM. Mechanics of atoms and fullerenes in single-walled carbon nanotubes.
 Acceptance and suction energies. P R Soc A 2007; 463: 461–477.
- Cox BJ, Thamwattana N and Hill JM. Mechanics of atoms and fullerenes in single-walled carbon nanotubes.
 II. Oscillatory behaviour. P R Soc A 2007; 463: 477–494.
- Cox BJ, Thamwattana N and Hill JM. Mechanics of spheroidal fullerenes and carbon nanotubes for drug and gene delivery. Q J Mech Appl Math 2007; 60: 231–253.
- 41. Baowan D, Thamwattana N and Hill JM. Zigzag and spiral configurations for fullerenes in carbon nanotubes. *J Phys A: Math Theor* 2007; 40: 7543–7556.
- 42. Baowan D, Thamwattana N and Hill JM. Encapsulation of C₆₀ fullerenes into single-walled carbon nanotubes: fundamental mechanical principles and conventional applied mathematical modeling. *Phys Rev B* 2007; 76: 155411.
- 43. Cox BJ, Thamwattana N and Hill JM. Spherical and spheroidal fullerenes entering carbon nanotubes. *Curr Appl Phys* 2008; 8: 249–252.
- 44. Cox BJ, Thamwattana N and Hill JM. Orientation of spheroidal fullerenes inside carbon nanotubes with potential applications as memory devices in nano-computing. *J Phys A: Math Theor* 2008; 41: 235209.
- 45. Chan Y, Thamwattana N and Hill JM. Spiral motion of carbon atoms and C60 fullerenes inside single-walled carbon nanotubes. *Int J Theor Appl Multiscale Mech* 2009; 1: 176–193.
- 46. Chan Y and Hill JM. Some novel plane trajectories for carbon atoms and fullerenes captured by two fixed parallel carbon nanotubes. *Eur Phys J D* 2010; 59: 367–374.
- 47. Baowan D, Triampo W and Triampo D. Encapsulation of TiO2 nanoparticles into single-walled carbon nanotubes. *New J Phys* 2009; 11: 093011.
- 48. Baowan D, Triampo D and Triampo W. Modeling of Titania nanoparticle accumulation at the open end of single-walled carbon nanotubes prior to TiO2 encapsulation. *J Comput Theor Nanos* 2010; 7: 1926–1930.
- 49. Sukchom W, Chayantrakom K, Satiracoo P, et al. Three possible encapsulation mechanics of TiO2 nanoparticles into single-walled carbon nanotubes. *J Nanomater* 2011; 2011: 1–8.
- Baowan D and Thamwattana N. Modelling selective separation of trypsin and lysozyme using mesoporous silica. *Micropor Mesopor Mat* 2013; 176: 209–214.
- Thamwattana N, Baowan D and Cox BJ. Modelling bovine serum albumin inside carbon nanotubes. RSC Adv 2013; 3: 23482–23488.
- 52. Alshehri MH, Cox BJ and Hill JM. Interaction of double-stranded DNA inside single-walled carbon nanotubes. *J Math Chem* 2012; 50: 2512–2526.
- 53. Alshehri MH, Cox BJ and Hill JM. DNA adsorption on graphene. *Eur Phys J D* 2013; 67: 226.
- 54. Alshehri MH, Cox BJ and Hill JM. Determination of optimal nanotube radius for single-strand

Baowan and Hill 15

- deoxyribonucleic acid encapsulation. *Micro Nano Lett* 2014; 9: 113–118.
- 55. Alshehri MH, Cox BJ and Hill JM. Offset configurations for single- and double-strand DNA inside single-walled carbon nanotubes. *Eur Biophys J* 2014; 43: 25–33.
- Baowan D, Cox BJ and Hill JM. Instability of C₆₀ fullerene interacting with lipid bilayer. *J Mol Model* 2012; 18: 549–557.
- Baowan D, Peuschel H, Kraegeloh A, et al. Energetics of liposomes encapsulating silica nanoparticles. *J Mol Model* 2013; 19: 2459–2472.
- Baowan D and Thamwattana N. Modelling encapsulation of gold and silver nanoparticles inside lipid nanotubes. *Physica A* 2014; 396: 149–154.
- Hilder TA and Hill JM. Maximum velocity for a single water molecule entering a carbon nanotube. *J Nanosci Nanotechnol* 2009; 9: 1403–1407.
- Baowan D and Thamwattana N. Modelling adsorption of a water molecule into various pore structures of silica gel. J Math Chem 2011; 49: 2291–2307.
- 61. Chan Y and Hill JM. A mechanical model for single-file transport of water through carbon nanotube membranes. *J Membrane Sci* 2011; 372: 57–65.
- 62. Garalleh HA, Thamwattana N, Cox BJ, et al. Modelling carbon dioxide molecule interacting with aquaglyceroporin and aquaporin-1 channels. *J Math Chem* 2013; 51: 2317–2327.
- Garalleh HA, Thamwattana N, Cox BJ, et al. Modelling interaction between ammonia and nitric oxide molecules and aquaporins. *J Math Chem* 2013; 51: 2020–2032.
- Garalleh HA, Thamwattana N, Cox BJ, et al. Modelling van der waals interaction between water molecules and biological channels. *J Comput Theor Nanos* 2013; 10: 2722–2731.
- 65. Tran-Duc T, Thamwattana N, Cox BJ, et al. Adsorption of polycyclic aromatic hydrocarbons on graphite surfaces. *Comp Mater Sci* 2010; 49: S307–S312.
- Tran-Duc T, Thamwattana N, Cox BJ, et al. General model for molecular interactions in a benzene dimer. *Math Mech Solids* 2010; 15: 782–799.
- 67. Tran-Duc T, Thamwattana N, Cox BJ, et al. Modelling the interaction in a benzene dimer. *Philos Mag* 2010; 90: 1771–1785.
- 68. Tran-Duc T, Thamwattana N, Cox BJ, et al. Encapsulation of a benzene molecule into a carbon nanotube. *Comp Mater Sci* 2011; 50: 2720–2726.
- Thamwattana N, Tran-Duc T and Baowan D. Modelling interactions between a PBB and fullerenes. *J Math Chem* 2013; 51: 1001–1022.
- Adisa OO, Cox BJ and Hill JM. Encapsulation of methane molecules into carbon nanotubes. *Physica B* 2011; 406: 88–93.
- 71. Adisa OO, Cox BJ and Hill JM. Packing configurations for methane storage in carbon nanotubes. *Eur Phys J B* 2011; 79: 177–184.
- 72. Adisa OO, Cox BJ and Hill JM. Modelling the surface adsorption of methane on carbon nanostructures. *Carbon* 2011; 49: 3212–3218.
- 73. Adisa OO, Cox BJ and Hill JM. Methane storage in molecular nanostructures. *Nanoscale* 2012; 4: 3295–3307.

- Baowan D. Modelling of carbon dioxide: methane separation using titanium dioxide nanotubes. *J Math Chem* 2012; 50: 300–309.
- 75. Chan Y and Hill JM. Modelling interaction of atoms and ions with graphene. *Micro Nano Lett* 2010; 5: 247–250.
- Chan Y and Hill JM. Lithium ion storage between graphenes. Nanoscale Res Lett 2011; 6: 203.
- Chan Y and Hill JM. Modeling on ion rejection using membranes comprising ultra-small radii carbon nanotubes. Eur Phys J B 2012; 85: 56.
- 78. Chan Y and Hill JM. Ion selectivity using membranes comprising functionalized carbon nanotubes. *J Math Chem* 2013; 51: 1258–1273.
- 79. Rahmat F, Thamwattana N and Cox BJ. Modelling peptide nanotubes for artificial ion channels. *Nanotechnology* 2011; 22: 445707.
- 80. Thornton AW, Hilder T, Hill AJ, et al. Predicting gas diffusion regime within pores of different size, shape and composition. *J Membrane Sci* 2009; 336: 101–108.
- 81. Thornton AW, Nairn KM, Hill JM, et al. Metal-organic frameworks impregnated with magnesium-decorated full-erenes for methane and hydrogen storage. *J Am Chem Soc* 2009; 131: 10662–10669.
- Thornton AW, Furman SA, Nairn KM, et al. Analytical representation of micropores for predicting gas adsorption in porous materials. *Micropor Mesopor Mat* 2013; 167: 188–197.
- 83. Chan Y and Hill JM. Dynamics of benzene molecules situated in metal-organic frameworks. *J Math Chem* 2011; 49: 2190–2209.
- Chan Y and Hill JM. Hydrogen storage inside grapheneoxide frameworks. *Nanotechnology* 2011; 22: 305403.
- 85. Adisa OO, Cox BJ and Hill JM. Open carbon nanocones as candidates for gas storage. *J Phys Chem C* 2011; 115: 24528–24533.
- Konstas K, Taylor JW, Thornton AW, et al. Lithiated porous aromatic frameworks with exceptional gas storage capacity. *Angew Chem* 2012; 124: 6743–6746.
- 87. Lim WX, Thornton AW, Hill AJ, et al. High performance hydrogen storage from Be-BTB metal-organic framework at room temperature. *Langmuir* 2013; 29: 8524–8533.
- 88. Tran-Duc T, Thamwattana N and Baowan D. Modelling gas storage capacity for porous aromatic frameworks. *J Comput Theor Nanos* 2014; 11: 234–241.
- 89. Hirschfelder JO, Curtiss CF and Bird RB. *Molecular the-ory of gases and liquids*. Hoboken, NJ: John Wiley & Sons, 1954.
- Mayo SL, Olafson BD and Goddard WA. DREIDING: a generic force field for molecular simulations. *J Phys Chem* 1990; 94: 8897–8909.
- Rappe AK, Casewit CJ, Colwell KS, et al. UFF, a full periodic table force field for molecular mechanics and molecular dynamics simulations. *J Am Chem Soc* 1992; 114: 10024–10035.
- 92. Erdélyi A, Magnus W, Oberhettinger F, et al. *Higher transcendental functions*. New York: McGraw-Hill, 1953, pp.59–62.
- 93. Bailey WN. *Generalized Hypergeometric Series*. New York: Hafner publishing company, 1972.

- Gradshteyn IS and Ryzhik IM. Table of Integrals, Series, and Products. 6th ed. Cambridge, MA: Academic Press, 2000.
- Cumings J and Zettl A. Low-friction nanoscale linear bearing realized from multiwall carbon nanotubes. Science 2000; 289: 602–604.
- Legoas SB, Coluci VR, Braga SF, et al. Moleculardynamics simulations of carbon nanotubes as gigahertz oscillators. *Phys Rev Lett* 2003; 90: 055504.
- Rivera JL, McCabe C and Cummings PT. Oscillatory behavior of double-walled nanotubes under extension: a simple nanoscale damped spring. *Nano Lett* 2003; 3: 1001–1005.
- 98. Rivera JL, McCabe C and Cummings PT. The oscillatory damped behaviour of incommensurate double-walled carbon nanotubes. *Nanotechnology* 2005; 16: 186–198.
- Otani M, Okada S and Oshiyama A. Energetics and electronic structures of one-dimensional fullerene chains encapsulated in zigzag nanotubes. *Phys Rev B* 2003; 68: 125424.
- Sattler K. Scanning tunneling microscopy of carbon nanotubes and nanocones. *Carbon* 1995; 33: 915–920.
- Charlier JC and Rignanese GM. Electronic structure of carbon nanocones. *Phys Rev Lett* 2001; 86: 5970–5973.
- 102. Verberck B and Michel KH. Nanotube field of C60 molecules in carbon nanotubes: atomistic versus continuous approach. *Phys Rev B* 2006; 74: 045421.
- 103. Ruoff RS and Hickman AP. Van der Waals binding of fullerenes to a graphite plane. J Phys Chem 1993; 97: 2494–2496
- 104. Iglesias-Groth S, Breton J and Girardet C. An analytical approach for the interlayer interaction in spherical buck-yonions. *Chem Phys Lett* 1997; 264: 351–358.
- 105. Guérin H. Interaction energy between shells of spherical carbon onions. *J Phys B: At Mol Opt Phys* 1997; 30: L481–L485.
- 106. Lu JP and Yang W. Shape of large single- and multiple-shell fullerenes. *Phys Rev B* 1994; 49: 11421–11424.
- 107. Henrard L, Hernández E, Bernier P, et al. Van der Waals interaction in nanotube bundles: consequences on vibrational modes. *Phys Rev B* 1999; 60: R8521–R8524.
- 108. Endo M, Kim YA, Hayashi T, et al. Structural characterization of cup-stacked-type nanofibers with an entirely hollow core. *Appl Phys Lett* 2002; 80: 1267–1269.
- 109. Shiratori Y, Hiraoka H, Takeuchi Y, et al. One-step formation of aligned carbon nanotube field emitters at 400°C. *Appl Phys Lett* 2003; 82: 2485–2487.
- 110. Endo M, Kim YA, Ezaka M, et al. Selective and efficient impregnation of metal nanoparticles on cupstacked-type carbon nanofibers. *Nano Lett* 2003; 3: 723–726.
- 111. Endo M, Kim YA, Hayashi T, et al. Microstructural changes induced in "stacked cup" carbon nanofibers by heat treatment. *Carbon* 2003; 41: 1941–1947.
- 112. Kim YA, Hayashi T, Naokawa S, et al. Comparative study of herringbone and stacked-cup carbon nanofibers. *Carbon* 2005; 43: 3005–3008.
- 113. Rowsell JLC and Yaghi OM. Metal-organic frameworks: a new class of porous materials. *Micropor Mesopor Mat* 2004; 73: 3–14.

- 114. Kubas GJ. Fundamentals of H2 binding and reactivity on transition metals underlying hydrogenase function and H2 production and storage. Chem Rev 2007; 107: 4152–4205.
- 115. Schnobrich JK, Koh K, Sura KN, et al. A framework for predicting surface areas in microporous coordination polymers. *Langmuir* 2010; 26: 5808–5814.
- Lin X, Jia J, Zhao X, et al. High H2 adsorption by coordination-framework materials. *Angew Chem Int Ed Engl* 2006; 45: 7358–7364.
- 117. Watanabe T and Sholl DS. Accelerating applications of metal-organic frameworks for gas adsorption and separation by computational screening of materials. *Langmuir* 2012; 28: 14114–14128.
- Furukawa H, Ko N, Go YB, et al. Ultrahigh porosity in metal-organic frameworks. Science 2010; 329: 424–428.
- Brunauer S, Emmett PH and Teller E. Adsorption of gases in multimolecular layers. J Am Chem Soc 1938; 60: 309–319.
- 120. Sumida K, Hill MR, Hiroke S, et al. Synthesis and hydrogen storage properties of Be₁₂(OH)₁₂(1,3,5benzenetribenzoate)₄. *J Am Chem Soc* 2009; 131: 15120–15121.
- Furukawa H, Cordova KE, O'Keeffe M, et al. The chemistry and applications of metal-organic frameworks. *Science* 2013; 341: 1230444.
- 122. Dimitrakakis GK, Tylianakis E and Froudakis GE. Pillared graphene: a new 3-D network nanostructure for enhanced hydrogen storage. *Nano Lett* 2008; 8: 3166–3170.
- 123. Ghosh A, Subrahmanyam KS, Krishna KS, et al. Uptake of H2 and CO2 by graphene. *J Phys Chem C* 2008; 112: 15704–15707.
- Srinivas G, Zhu Y, Piner R, et al. Synthesis of graphenelike nanosheets and their hydrogen adsorption capacity. *Carbon* 2010; 48: 630–635.
- 125. Hillebrenner H, Buyukserin F, Stewart JD, et al. Template synthesized nanotubes for biomedical delivery applications. *Nanomedicine* 2006; 1: 39–50.
- 126. Hilder TA and Hill JM. Modelling the encapsulation of the anticancer drug cisplatin into carbon nanotubes. *Nanotechnology* 2007; 18: 275704.
- 127. Hilder TA and Hill JM. Carbon nanotubes as drug delivery nanocapsules. Curr Appl Phys 2008; 8: 258–261.
- 128. Hilder TA and Hill JM. Probability of encapsulation of paclitaxel and doxorubicin into carbon nanotubes. *Micro Nano Lett* 2008; 3: 41–49.
- 129. Hilder TA and Hill JM. Theoretical comparison of nanotube materials for drug delivery. *Micro Nano Lett* 2008; 3: 18–24.
- Hilder TA and Hill JM. Double-walled carbon nanotubes as nanosyringes. *J Comput Theor Nanos* 2008; 5: 2153–2159.
- 131. Hilder TA and Hill JM. Modeling the loading and unloading of drugs into nanotubes. *Small* 2009; 5: 300–308.
- 132. Ansari R, Kazemi E, Mahmoudinezhad E, et al. Preferred position and orientation of anticancer drug cisplatin during encapsulation into single-walled carbon nanotubes. *J Nanotechnol Eng Med* 2012; 3: 010903.

RSC Advances



PAPER



Cite this: RSC Adv., 2016, 6, 46658

Received 24th January 2016 Accepted 4th May 2016

DOI: 10.1039/c6ra02126c

www.rsc.org/advances

Mathematical methods on atomic force microscope cantilever systems

Kanes Sumetpipat, a Duangkamon Baowan, a Barry J. Coxb and James M. Hillc

The ever increasing demand to analyse substrates means that an improved theoretical understanding is necessary for atomic force microscope cantilevers. In this study, we utilize fundamental mathematical modelling, comprising the Lennard-Jones potential and techniques involving the calculus of variations, to obtain the energy equations arising from the probe and the substrate, leading to the deflection equations of the cantilever. Here we assume a silicon tip and the substrate surface is assumed to be a graphene sheet. Based on an energy calculation, the most stable system occurs where the probe is 0.206 nm away from the substrate, and this value exists independently of the size and tilt angle of the probe. For the deflection of the cantilever, we apply the calculus of variations to the separate domains, considering derivatives up to third order at the connection point. The deflection behaviour of a V shaped plate depends primarily on its length, and the spring constants of various cantilevers are calibrated from the deflection equations. In comparison to the zeroth order method of previous studies, our method predicts a 30–50% difference in the value of their spring constants. Moreover, we observe the bending behaviour of cantilever systems by considering the energy between the probe and the substrate together with the bending energy in the cantilever, and we find that the maximum bending distance at the tip is in the range between 0.09 nm and 0.2 nm.

1 Introduction

Atomic force microscope (AFM) cantilevers can be used to measure the properties of substrate surfaces in the nanometer to micrometer range, and are becoming increasingly adopted in many diverse areas requiring an ever increasing accuracy. The operating modes of AFM cantilevers can be divided into three main categories which are the contact mode, the tapping mode, and the non-contact mode, and each mode has different advantages and applications. AFM cantilevers may be used to scan either rigid bodies, or liquid surfaces, or biological materials and can clarify shapes and response characteristics in various environments. For example, Kasas *et al.*¹ use an AFM in biological systems to investigate the RNA, collagen fiber, virus and kidney cells, and Franz *et al.*² employ an AFM to study the mechanics of cell adhesion.

There have been numerous investigations on AFM cantilever properties.³ The most important aspect of any AFM cantilever is the accuracy of the measurements involving elasticity, geometric shape, temperature, spring constant including adhesive force, type of substrate and the loading position. To

obtain this data and minimize any errors in measurement, many interesting techniques have been proposed, such as uncertainty analysis, focused curve analysis, focused ion beam with spatial marker, where the shape of the cantilever and the tip, and the spring calibration constant are the two main aspects of the investigations.4-7 Sader et al.8 propose a theoretical model to determine the spring constant for isosceles trapezoidal and V-shaped thin plates. Based on the well-known elastic strain equations for an arbitrary thin plate,9 these authors derive the deflection equations for such cantilevers. The deflection equations are solved using a zeroth order method and a second order method where the former method assumes a solution in one variable. Their results show that both methods give similar results in determining the spring constant and they are in a good agreement as compared to a finite element calculation. Moreover, their second order method can also be used for more general cantilever geometries.

Cleveland *et al.*¹⁰ also derive the spring constant for AFM cantilevers, and measure the resonant frequency of tungsten spheres with different masses with a force loading at the end. The spring constants obtained in their study are in agreement with the theoretical result shown in.¹¹ Sader *et al.*¹² analyze the effect of air damping and the cantilever position where the force is applied, and the spring constant obtained after considering the air damping term shows excellent agreement with Cleveland *et al.*¹⁰ Sader *et al.*¹² comment that the cantilever thickness and the gold coating also affect the observed frequency.

[&]quot;Department of Mathematics, Faculty of Science, Mahidol University, Centre of Excellence in Mathematics, CHE, Rama VI Rd., Si Ayutthaya Rd, Bangkok 10400, Thailand. E-mail: duangkamon.bao@mahidol.ac.th

^bSchool of Mathematical Sciences, The University of Adelaide, Adelaide, SA 5005, Australia

^cSchool of Information Technology and Mathematical Sciences, University of South Australia, Mawson Lakes, South Australia 5095, Australia

Paper RSC Advances

Besides direct calculation of the spring constant, a number of researchers consider torsional spring constants, because AFM cantilevers might be acted upon by lateral forces during their operation. Green *et al.*¹³ extend the solutions of Sader *et al.*¹⁴ and Cleveland *et al.*¹⁶ to find such torsional spring constants. Hoogenboom *et al.*¹⁵ employ the Fabry–Perot interferometer together with the cantilever to scan the surface of aqueous or liquid environments by considering thermal noise and the frequency of the silicon cantilever. Fukuma *et al.*¹⁶ develop a cantilever system that is more sensitive to the noise so that it can be applied in diverse environments.

Cai *et al.*¹⁷ design the shape of cantilevers to achieve a wide range of frequencies so that small changes in the cantilever probe can be detected. Stevens *et al.*¹⁸ utilize the nanotube as a probe and report that the image resolution of the general silicon tip and nanotube tip are similar. Further, the nanotube can give better accuracy of the image height than the general silicon tip. There are also other studies that calibrate the spring constant and propose new techniques for cantilever use and we direct the interested reader to the following studies.^{19–28}

Even though the literature contains many results from experiments on AFM cantilevers, further analytical and theoretical methods are required to better explain the function of the cantilevers. In this work, we study the cantilever system by employing classical mathematical modelling techniques to calculate forces and energies of the system, and involving two procedures. Firstly, we discuss the energy between the probe and the surface that is being scanned. Assuming only van der Waals forces, we utilize the Lennard-Jones potential to determine the energy of the system, where the probe is assumed to be a conical shape, and the surface is modelled as an infinite flat plane. Secondly, we discuss the bending of the cantilever to calculate the potential energy including its spring constant. The cantilever geometry considered in this work is the isosceles trapezoidal shape both with and without an isosceles trapezoidal hole. We then combine the results of these two calculations to determine the total energy of the system.

The calculation of the interaction between the probe and the surface and the calculation of the deflecting cantilever are presented in Section 2. Additionally, the basic formulae for the molecular interactions and the calculus of variations formulae are also detailed in this section. Results for the mechanical system for the AFM cantilever are discussed in Section 3, and finally, we give some concluding remarks in Section 4.

2 Mathematical derivations

2.1 Interaction between tip and surface

We employ a Lennard-Jones potential to determine the energy between two non-bonded molecules. The Lennard-Jones potential may be expressed in two equivalent forms

$$\Phi(
ho) = 4\varepsilon \left[-\left(rac{\sigma}{
ho}
ight)^6 + \left(rac{\sigma}{
ho}
ight)^{12}
ight] = -rac{A}{
ho^6} + rac{B}{
ho^{12}},$$

where ε is the well depth, σ is the van der Waals diameter and ρ is the distance between atoms. We note that, $A=4\varepsilon\sigma^6$ and B=

 $4\varepsilon\sigma^{12}$ are the attractive and repulsive constants, respectively. For two different atoms, we employ the empirical mixing rules for ε and σ which are $\varepsilon=(\varepsilon_1\varepsilon_2)^{1/2}$ and $\sigma=(\sigma_1+\sigma_2)/2$, where the numerals 1 and 2 refer to the two atomic species. For two molecules, the total energy can be obtained by summing all atomic pairs from the two molecules. However, the number of atoms in the systems considered in this paper are very large and we calculate the total energy via a continuous approximation assuming that the atoms are uniformly distributed over the materials. Hence, the total interaction energy may be approximated as an integral

$$E=\eta_1\eta_2{\int_{S_1}}\int_{S_2}\Phi(
ho)\mathrm{d}S_2\mathrm{d}S_1,$$

where η_1 and η_2 are the mean surface or the mean volume densities of the materials, and S_1 and S_2 are the surface or volume elements.

2.1.1 Interaction between a point and a plane surface. We start by calculating the energy between a point and a plane surface. The surface is assumed to be an infinite plane and located at z=0. The distance between the point and such a plane is denoted by ω , and the coordinates of the point are $(0,0,\omega)$ as shown in Fig. 1. Thus, the total interaction energy has the form

$$E_{\rm pp} = \eta_{\rm p} \int_{-\infty}^{\infty} \int_{-\infty}^{\infty} \Phi(\rho) \mathrm{d}x \mathrm{d}y,$$

which we write as

$$E_{\rm pp} = \eta_{\rm p}(-AI_3 + BI_6),$$

where η_p is the mean surface density of the plane, and

$$I_n = \int_{-\infty}^{\infty} \int_{-\infty}^{\infty} \rho^{-2n} dx dy = \int_{-\infty}^{\infty} \int_{-\infty}^{\infty} (x^2 + y^2 + \omega^2)^{-n} dx dy.$$

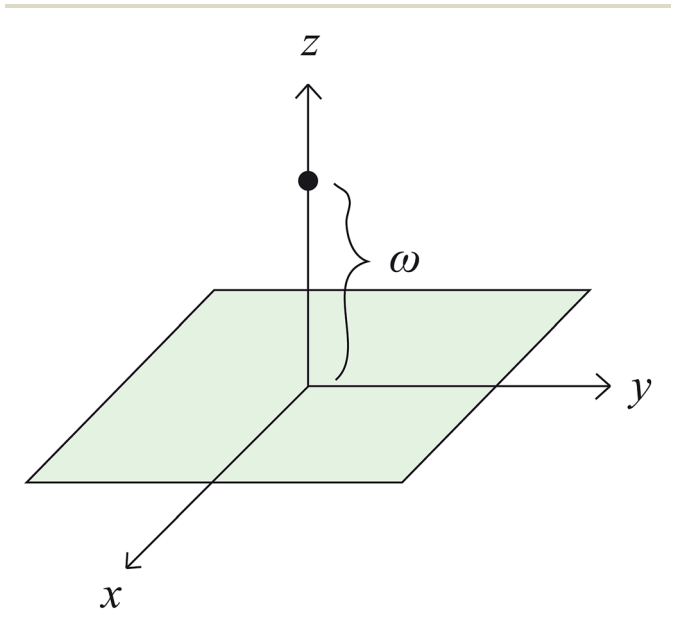


Fig. 1 Configuration of point and plane surface.

RSC Advances Paper

We make the substitution $x = \sqrt{y^2 + \omega^2} \tan(\psi)$ to obtain

$$I_n = B(n-1/2,1/2) \int_{-\infty}^{\infty} (y^2 + \omega^2)^{1/2-n} dy,$$

where B(m, n) is the beta function, and then let $y = \omega \tan(\psi)$ to deduce

$$I_n = \omega^{2(1-n)} B(n-1,1/2) B(n-1/2,1/2) = \frac{\pi}{n-1} \omega^{2(1-n)}, \quad (1)$$

so that we have

$$E_{
m pp} = \eta_{
m p} \Big[- A \Big(rac{\pi}{2\omega^4} \Big) + B \Big(rac{\pi}{5\omega^{10}} \Big) \Big].$$

2.1.2 Interaction between a cone and a plane surface. Next, we consider the energy between a cone and a plane surface as illustrated in Fig. 2. We assume that the right-circular cone is given by the equation,

$$\frac{x^2}{k^2} + \frac{y^2}{k^2} = z^2.$$

Assume also that is the plane is located below the vertex of the cone at a distance ε , so that the distance between any point of the cone located on the *z*-axis and the plane is $\omega = z + \varepsilon$. The cone base area that is parallel to the plane at a height $\omega = z + \varepsilon$ has the area $A_z = \pi k^2 z^2$, and the cone angle is denoted by α , so $\tan(\alpha/2) = k$. Let the integral J_n be defined by

$$J_n = \int_0^\infty I_n A_z dz,$$

where I_n is defined by (1), then we may deduce

$$E_{\rm cp} = \eta_{\rm p} \eta_{\rm c} (-AJ_3 + BJ_6).$$

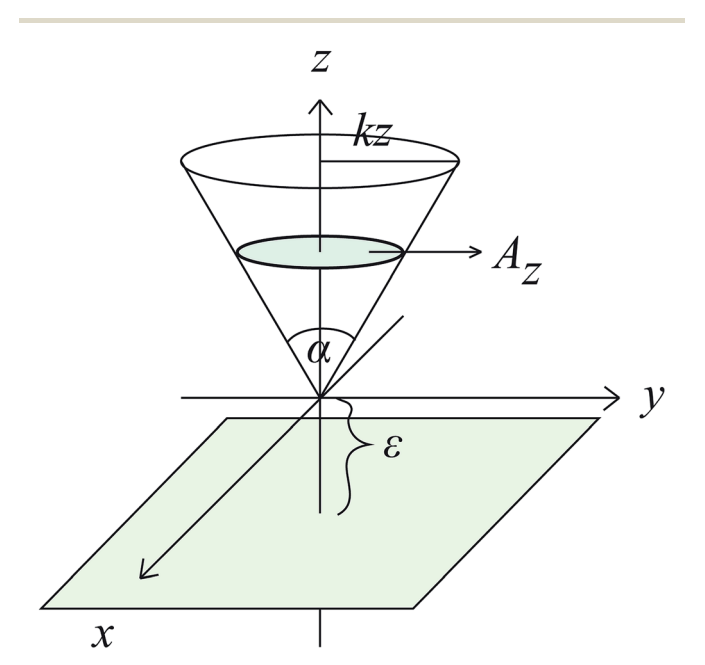


Fig. 2 Configuration of right cone and plane surface.

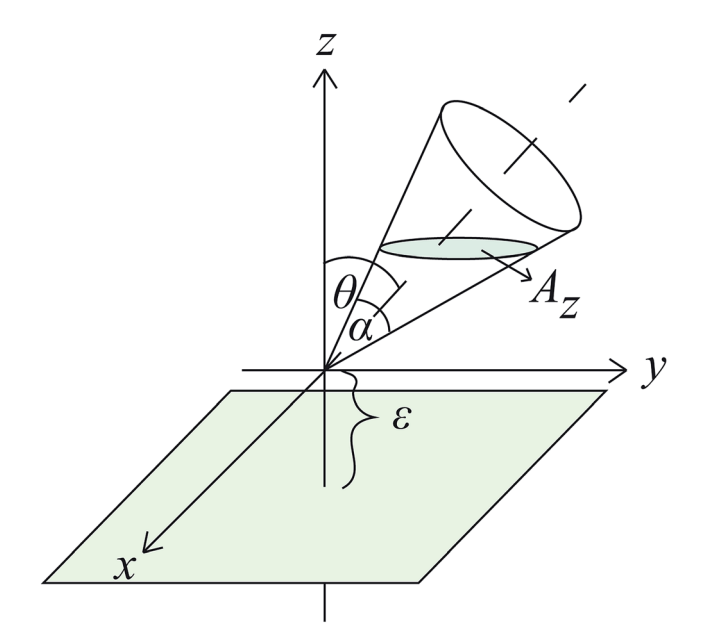


Fig. 3 Configuration of tilted cone and plane surface.

For the right cone, we may have

$$\begin{split} J_n^{\text{right}} &= \frac{\pi}{n-1} \int_0^\infty (z+\varepsilon)^{2(1-n)} \pi k^2 z^2 \mathrm{d}z \\ &= \frac{\pi^2 k^2}{(n-1)\varepsilon^{2(n-1)}} \int_0^\infty \frac{z^2}{(z/\varepsilon+1)^{2(n-1)}} \mathrm{d}z \\ &= \frac{\pi^2 k^2}{(n-1)\varepsilon^{2n-5}} B(2n-5,3). \end{split}$$

The tilted cone system can be established by rotating the right cone through an angle θ as shown in Fig. 3, so that we have

$$x_N = x$$
, $y_N = y \cos \theta - z \sin \theta$, $z_N = y \sin \theta + z \cos \theta$.

From the equation for a right cone, we substitute the relations for x, y and z to obtain

$$(x/k)^2 + [(v\cos\theta - z\sin\theta)/k]^2 = (v\sin\theta + z\cos\theta)^2$$
.

from which we may deduce

$$(x/k)^2 + Gv^2 - Hv = F.$$

where

$$G = \frac{\cos^2 \theta}{k^2} - \sin^2 \theta, H = z \sin(2\theta) \left(1 + \frac{1}{k^2} \right),$$
$$F = z^2 \left(\cos^2 \theta - \frac{\sin^2 \theta}{k^2} \right).$$

The equation for the tilted cone may be written in the elliptic form given by

$$\frac{x^2}{k^2 GW} + \frac{(y - H/2G)^2}{W} = 1,$$

Paper RSC Advances

where $W = (F/G) + (H^2/4G^2)$. Thus, the cone base area parallel to the plane at location z is $A_z = \pi k \sqrt{GW} \sqrt{W} = \pi kW \sqrt{G}$, and we write $W\sqrt{G} = Xz^2$, that $X = (W\sqrt{G})_{z=1}$, and

$$J_n^{\text{tilt}} = \frac{\pi}{n-1} \int_0^\infty (z+\varepsilon)^{2(1-n)} \pi k X z^2 dz$$
$$= \frac{\pi^2 k X}{(n-1)\varepsilon^{2(n-1)}} \int_0^\infty \frac{z^2}{(z/\varepsilon+1)^{2(n-1)}} dz.$$

Similarly for the case of the right cone, the integral $J_n^{\rm tilt}$ becomes

$$J_n^{\text{tilt}} = \frac{\pi^2 kX}{(n-1)\varepsilon^{2n-5}} B(2n-5,3),$$

and $J_{n(\theta \to 0)}^{\text{tilt}} \to J_{n}^{\text{right}}$. We define ε_{\min} to be the equilibrium distance ε that gives the minimum energy, and both the right cone and the tilted cone systems yield $\varepsilon_{\min} = \left[B/(30A) \right]^{1/6}$ where A and B are the attractive and repulsive Lennard-Jones constants, respectively.

2.2 Calculus of variations method on cantilever plate

Functionals involving the derivatives of higher order have the form

$$v(y(x)) = \int_{x_0}^{x_1} F(x, y(x), y'(x), ..., y^{(n)}(x)) dx,$$

where the integrand F involves derivatives of order n with respect to x. On using the variational calculus, the Euler-Lagrange equation can be obtained as,

$$F_{y} - \frac{\mathrm{d}}{\mathrm{d}x} F_{y'} + \frac{\mathrm{d}^{2}}{\mathrm{d}x^{2}} F_{y''} + \dots + (-1)^{n} \frac{\mathrm{d}^{n}}{\mathrm{d}x^{n}} F_{y^{(n)}} = 0,$$

the general solution of this equation has 2n arbitrary constants which are obtained from the 2n boundary conditions,

$$y(x_0) = y_0, y'(x_0) = y'_0, \dots, y^{(n-1)}(x_0) = y_0^{(n-1)},$$

and this solution provides an extremum for the functional v(y(x)).

2.2.1 Deflection equations. The approximate potential energy *V* for an arbitrary cantilever plate may be given by

$$V = \frac{1}{2} \iint D\left\{ \left(\frac{\partial^2 w}{\partial x^2} + \frac{\partial^2 w}{\partial y^2} \right)^2 - 2(1 - \nu) \left[\frac{\partial^2 w}{\partial x^2} \frac{\partial^2 w}{\partial y^2} - \left(\frac{\partial^2 w}{\partial x \partial y} \right)^2 \right] \right\} dx dy,$$

where w(x, y) is a deflection function, $D = E^*t^3/[12(1 - \nu^2)]$ with Young's modulus E^* , the thickness t, and Poisson's ratio ν . The boundary conditions of this cantilever are w(0, y) = 0, $w_x(0, y) = 0$, $w(L, y) = \delta$, $w_{xx}(L, y) = 0$ and $w_y(0, y) = 0$, where δ denotes the bending distance of the cantilever. The configuration of the cantilever is as shown in Fig. 4. We assume w to depend only on x, w(x), which is assumed to satisfy the prescribed condition on $w_y(0, y)$ and the potential energy function becomes

$$V = \frac{1}{2} \iint Dw''^2 dx dy$$

$$= \frac{D}{2} \int_0^L \int_{mx-C}^{-mx+C} (w'')^2 dy dx - \frac{D}{2} \int_0^\ell \int_{mx-E}^{-mx+E} (w'')^2 dy dx$$

$$= \frac{D}{2} \int_0^\ell 2(w'')^2 (C - E) dx + \frac{D}{2} \int_\ell^L 2(w'')^2 (-mx + C) dx. \quad (2)$$

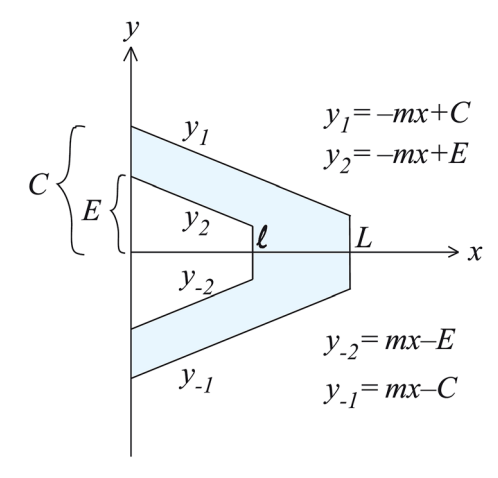


Fig. 4 Cantilever configuration, where y_1 , y_2 , y_{-1} and y_{-2} are linear functions for outside and inside isosceles trapezoid's edges, $\pm m$ are slope of edges, C and E are shown widths, and E are shown lengths.

From the Euler-Lagrange equation of second order

$$F_{w} - \frac{\mathrm{d}}{\mathrm{d}x} F_{w'} + \frac{\mathrm{d}^{2}}{\mathrm{d}x^{2}} F_{w''} = 0,$$

and from the first integral of (2), we may deduce

$$w(x) = T_3 x^3 + T_2 x^2 + T_1 x + T_0, (3)$$

where T_0 , T_1 , T_2 and T_3 are constants, and $0 \le x \le \ell$. Next, by using the Euler–Lagrange equation again for the second integral term in (2), we find

$$w^{(4)}(x) - 2w'''(x)/(\xi - x) = 0, (4)$$

where $\xi = C/m$. On solving (4) using the integrating factor to give $w'''(x) = \lambda/(\xi - x)^2$, we have

$$w(x) = \lambda(\xi - x)(\log|\xi - x| - 1) + K_2x^2 + K_1x + K_0,$$
 (5)

where λ , K_0 , K_1 and K_2 are all constants, and $0 \le x \le \ell$.

Next, we use the boundary conditions to find the unknown constants. Considering w(0) = 0 and w'(0) = 0 in (3) shows that $T_0 = T_1 = 0$, and the solution becomes

$$w(w) = T_3 x^3 + T_2 x^2. (6)$$

The other two conditions, $w(L) = \delta$ and w''(L) = 0, are now applied to (5) to obtain

$$\delta = \lambda(\xi - L)(\log|\xi - L| - 1) + K_2L^2 + K_1L + K_0, \tag{7}$$

$$K_2 = -\lambda/[2(\xi - L)]. \tag{8}$$

We now need to find the constants K_0 , K_1 , K_2 and K_3 assuming that the function K_2 at K_3 is continuous and smooth up to the third derivative; which means, K_3 and K_4 from (5) and (6) must coincide, and the four equations are

RSC Advances Paper

$$T_{3}\ell^{3} + T_{2}\ell^{2} = \lambda(\xi - \ell)(\log|\xi - \ell| - 1) + K_{2}\ell^{2} + K_{1}\ell + K_{0},$$

$$3T_{3}\ell^{2} + 2T_{2}\ell = -\lambda\log|\xi - \ell| + 2K_{2}\ell + K_{1},$$

$$6T_{3}\ell + 2T_{2} = \lambda(\xi - \ell) + 2K_{2},$$

$$T_{3} = \lambda/[6(\xi - \ell)^{2}].$$
(9)

From (7)–(9), both solutions from (5) and (6) may be given by

$$w_1(x) = \frac{\lambda x^3}{6(\xi - \ell)^2} + \frac{\lambda}{2} \left(\frac{1}{(\xi - \ell)} - \frac{1}{(\xi - L)} - \frac{\ell}{(\xi - \ell)^2} \right) x^2, 0 \le x \le \ell,$$
(10)

$$w_{2}(x) = \lambda(\xi - x)(\log|\xi - x| - 1) - \frac{\lambda}{2(\xi - L)}x^{2}$$

$$+\lambda \left(-\frac{\ell^{2}}{2(\xi - \ell)^{2}} + \frac{\ell}{\xi - \ell} + \log|\xi - \ell|\right)x + \lambda(\xi - \ell)$$

$$-\lambda \xi \log|\xi - \ell| - \frac{\lambda \ell^{2}}{2(\xi - \ell)} + \frac{\lambda \ell^{3}}{6(\xi - \ell)^{2}}, \ell \le x \le L, \quad (11)$$

where

$$\begin{split} \lambda &= \delta \bigg[(\xi - L) (\log \lvert \xi - L \rvert - 1) - \frac{L^2}{2(\xi - L)} \\ &+ \bigg(- \frac{\ell^2}{2(\xi - \ell)^2} + \frac{\ell}{\xi - \ell} + \log \lvert \xi - \ell \rvert \bigg) L + (\xi - \ell) - \xi \log \lvert \xi - \ell \rvert \\ &- \frac{\ell^2}{2(\xi - \ell)} + \frac{\ell^3}{6(\xi - \ell)^2} \bigg]^{-1}, \end{split}$$

and where $\xi = C/m$.

2.2.2 Energy and spring constant. The spring constant, k_w , is calculated from the energy per unit area. Here, the force is assumed to be applied to the end of the probe and the distance is taken to be w(L) which we denote by δ . Thus,

$$\begin{split} k_{\rm w} &= \frac{V}{\delta^2} \\ &= \frac{D}{2\delta^2} \left\{ (2C - 2E)\lambda^2 \left[\frac{\ell^3}{3(\xi - \ell)^4} - \frac{\ell^2}{(\xi - \ell)^2} \left(\frac{1}{\xi - \ell} - \frac{1}{\xi - L} \right) \right. \right. \\ &\left. + l \left(\frac{1}{\xi - \ell} - \frac{1}{\xi - L} \right)^2 \right] + 2\lambda^2 (L - \ell) \left(\frac{C}{(\xi - L)^2} - \frac{2m}{\xi - L} \right) \\ &\left. - 2m\lambda^2 \log \left| \frac{\xi - L}{\xi - \ell} \right| - \frac{m\lambda^2 (L^2 - \ell^2)}{(\xi - L)^2} \right\}, \end{split}$$

where V is defined by (2).

3 Results and discussion

The present section is divided into three subsections. In the first subsection, we discuss the interaction between the cone and the plane. Then we consider the bending behaviour of the cantilever system using the calculus of variations, and finally, we combine the two to model the mechanical cantilever system.

3.1 Interaction between cone and plane

Here we assume the cone or the tip to be made from silicon whereas the plane surface is assumed to be a graphene sheet. We choose graphene as an example because our approach assumes a two-dimensional flat surface. Moreover, graphene is a very stable nanomaterial, for which there is little chance to form chemical bonding with the molecules on the tip, and the interaction forces are dominated only by the van der Waals interactions. The constant values $A=7.8497~\mathrm{J~nm^6~mol^{-1}}$ and $B=0.0179~\mathrm{J~nm^{12}~mol^{-1}}$ in Lennard-jones potential are obtained from the silicon and carbon data in Rappé et~al., 29 and the value of the density $\eta_{\rm C}=38.12~\mathrm{nm^{-2}}$ is taken from Cox et~al. 30 The volume density of silicon is obtained by converting the units from kilogram per cubic meter to atom per cubic nanometer, and $\eta_{\rm Si}=49.977~\mathrm{nm^{-3}}$. In this section, we examine the energy between the cone and the plane surface $E_{\rm cp}$ and the equilibrium distance $\varepsilon_{\rm min}$ for various cones is deduced.

From Fig. 5, the energy of the system becomes positive when the vertex of the cone becomes close to the graphene plane. The systems are unstable when ε is less than 0.149 nm, and the equilibrium distance is obtained as $\varepsilon_{\rm min}=0.206$ nm. Our results show that the cone vertex experiences a strong repulsive force, whereas the bulk of the cone makes a much smaller contribution to the energy. Fig. 6 shows that the larger the cone angle α , the lower the energy. In other words, more atoms on the cone give rise to a larger interaction force between the cone and the plane. The smallest cone ($\alpha=\pi/16$ or 11.25°) gives rise to an energy of -1.65×10^{-21} J while the largest one ($\alpha=\pi/4$ or 45°) gives rise to an energy of -29.19×10^{-21} J.

The tilted cone system behaves similarly in terms of the ε value. However, in Fig. 7, the system which has a larger rotational angle θ will have a lower energy. Moreover, the value of ε_{\min} for the tilted cone system is the same as that for the right cone case, that is, 0.206 nm because $\theta + \alpha/2$ is not much greater than $\pi/2$. This means that the closest point between the cone and the plane is at the tip, and therefore the most important parameter is the interspacing ε . We note that the energy of the right cone system can also be obtained from the tilted cone case by using $J_{n(\theta \to 0)}^{\text{tilt}}$. Fig. 8 shows the possible lowest energy of the tilted cone for any θ . From the graph, the cone with $\alpha = \pi/16$ has a difference in energy around 10×10^{-21} J on rotating θ by 1 rad, whereas the cone with $\alpha = \pi/4$ has an energy difference of

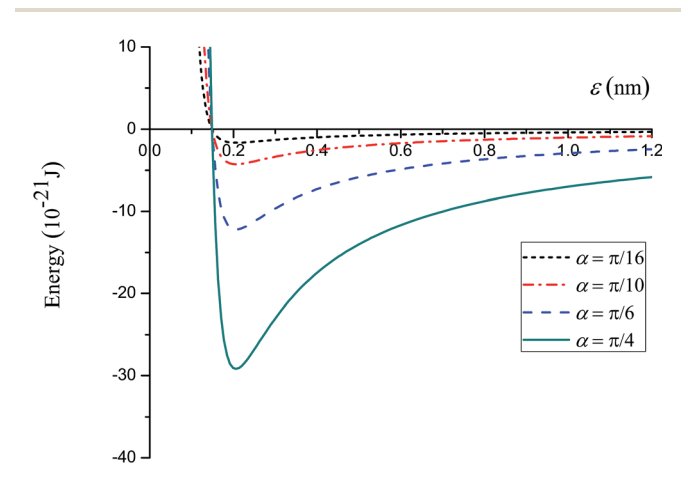


Fig. 5 Energy of right circular cones for various cone angles $\alpha=\pi/16$, $\pi/10$, $\pi/6$ and $\pi/4$.

Paper RSC Advances

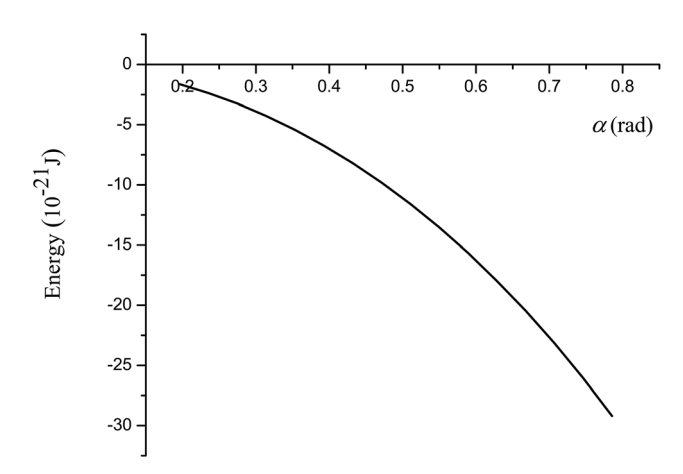


Fig. 6 Relation between energy of right cone and cone angle α at equilibrium distance $\varepsilon_{\min}=0.206$ nm.

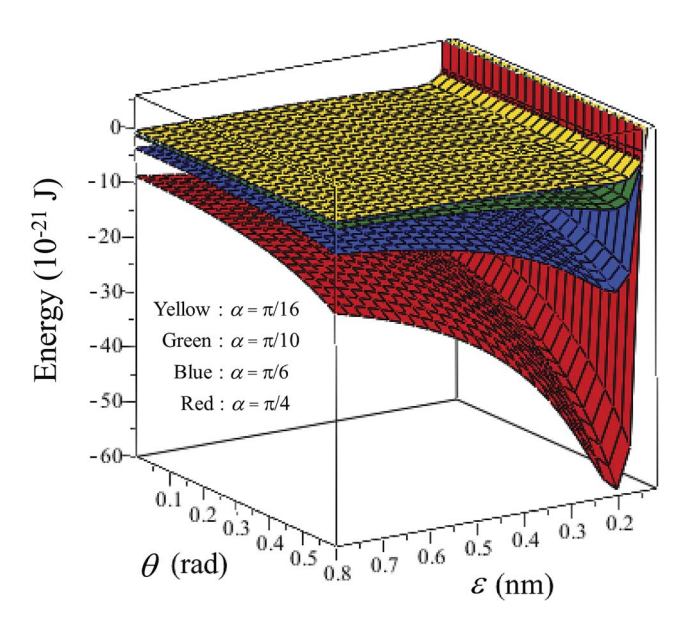


Fig. 7 Energy of tilted cone for various cone angles $\alpha=\pi/16,\,\pi/16,\,\pi/6$ and $\pi/4$.

around 30 \times 10^{-21} J corresponding to rotating θ through 0.6 rad.

3.2 Bending of cantilever

In this section, we consider a triangular cantilever with a triangular hole shape (V shape) in order to compare our results with the results of earlier studies. This means that the slope $m=C/L=E/\ell$ as shown in Fig. 4. Additionally, $w_1(x)$ and $w_2(x)$ from (10) and (11) approach a parabolic function $\delta x^2/L^2$. First of all, we consider the bending behaviour of four cantilevers as shown in Table 1 which are those considered by Sader $et~al.^{12}$ Here, we focus on comparing the predicted values of the spring constants, and we also discuss the spring constant values obtained by the zeroth order method and by our method.

The bending distance of Type 4 cantilever, $\delta_{\rm Type~4}$, is calculated from the bending distance of Type 1 cantilever, $\delta_{\rm Type~1}$,

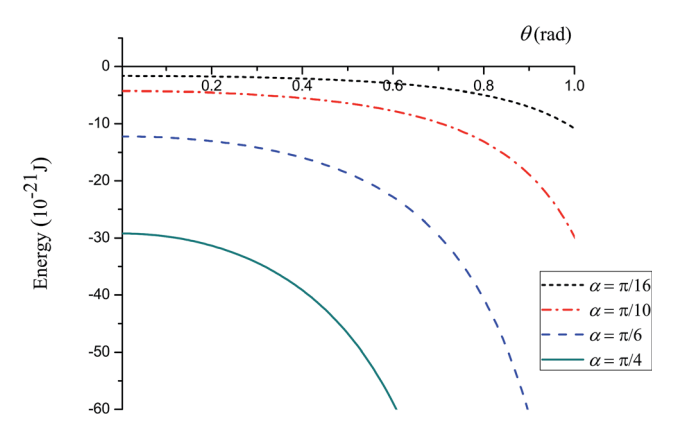


Fig. 8 Energy of tilted cone for $\varepsilon_{\rm min}$ = 0.206 nm and α = π /16, π /10, π /6 and π /4.

Table 1 Size of cantilevers used in this paper, $D_{\nu=0.25} = 0.3029 \times 10^{-8} \, \mathrm{J}$

	L (μ m)	ℓ (μ m)	C (µm)	$E(\mu m)$	m
Type 1	182	107.2	91	53.6	0.5
Type 2	176	139.46	79	62.6	0.4489
Type 3	89.2	61.34	45.15	31.05	0.5062
Type 4	89.4	41.54	45.2	21	0.5056

with the conditions that the deflection distance w(x) is equal (see Fig. 9) and the energy is equal (see Fig. 10). Further, we examine two values of $\delta_{\text{Type 1}}$ which are 0.4 nm and 0.5 nm. We note that these two values of the bending distances are very small compared with the length of cantilever L, and the bending distance δ measured vertically in the x-direction.

From (10) and (11), our bending behaviour does not depend on *D*. So, even for different materials, the same bending profiles

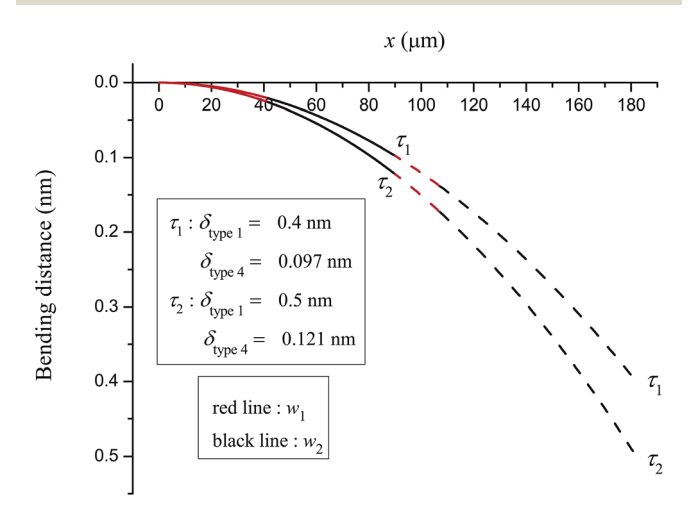


Fig. 9 Behaviour of bending plates of Type 1 and Type 4 cantilevers for equivalent deflection distance and comprising two different examples: $\delta_{\text{Type 1}} = 0.4$ nm for τ_1 and $\delta_{\text{Type 1}} = 0.5$ nm for τ_2 . Note that units of x-axis are micrometers while units of y-axis are nanometers, (dashed line: Type 1 and solid line: Type 4).

RSC Advances Paper

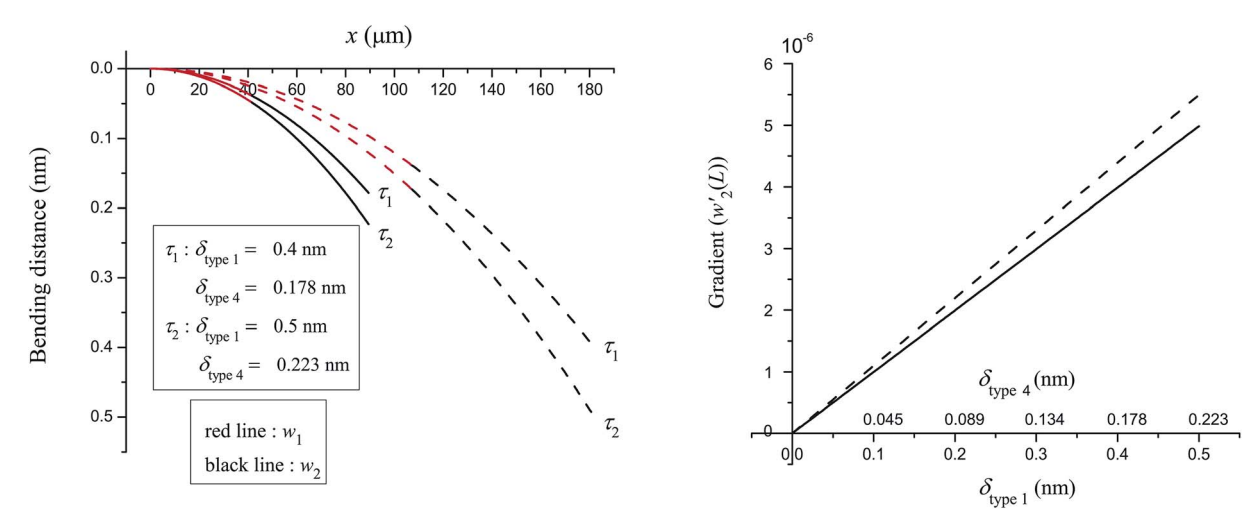


Fig. 10 (left) Behaviour of bending plates of Type 1 and Type 4 cantilevers for equivalent energy comprising two different examples: $\delta_{\text{Type 1}} = 0.4$ nm for τ_1 and $\delta_{\text{Type 1}} = 0.5$ nm for τ_2 . Assuming units of *x*-axis are micrometers while units of *y*-axis are nanometers. (right) Gradient at the end of bending cantilever, (dashed line: Type 1 and solid line: Type 4).

Table 2 Spring constants obtained by four methods, $k_{\rm clv}$ is taken from (ref. 10), $k_{\rm sd}$ is given in (ref. 12), $k_{\rm z}$ is formulated by the zeroth order method presented in (ref. 8), and $k_{\rm w}$ is obtained in this work. We use $D_{\nu=0.25}=0.3029\times 10^{-8}~{\rm J}$ for $k_{\rm z}$ and $k_{\rm w}$

	$k_{ m clv}$	$k_{ m sd}$	$k_{\rm z}$	$k_{ m w}$
Type 1	0.091	0.092	0.102	0.06
Type 2	0.044	0.044	0.05	0.033
Type 3	0.28	0.29	0.333	0.203
Type 4	0.46	0.47	0.536	0.301

(Fig. 9 and 10) will be obtained converging to the parabolic profile $\delta x^2/L^2$. Furthermore, our solutions approach $\delta x^2/L^2$ indicating that the bending behaviour is the same when C and E are different. Moreover, ℓ does not appear in the parabolic solution, that is, the equivalent V-shaped cantilevers with and without holes give the same bending behaviour. This is because our approach ignores the variable y, which is acceptable if

twisting or distortions do not occur in the *y*-direction.⁸ The major factor on the bending behaviour is the length of the cantilever *L*. From Fig. 9, the bending behaviour of Type 1 and Type 4 cantilevers are similar but the parabolae have different deflection magnitudes. In Fig. 10 (left), there is more interesting behaviour showing that Type 1 cantilevers bend more than Type 4 cantilevers with the same energy in the two systems. The ratio of the bending distance between Type 1 and Type 4 cantilevers $\delta_{\text{Type 4}}/\delta_{\text{Type 1}}$ is 0.4458 at the equivalent energy condition. We may infer that a longer cantilever bends more than a shorter one, as expected. Additionally, when we compare the gradient between Type 1 and Type 4 cantilevers as shown in Fig. 10 (right), Type 1 cantilever has the larger gradient as compared to that of Type 4, and therefore, Type 1 would require a larger bending angle θ .

Next, we consider the spring constants, k, presented in Table 2, where $k_{\rm clv}$ is obtained by Cleveland *et al.*, 10 $k_{\rm sd}$ is taken from Sader *et al.*, 12 while $k_{\rm z}$ is obtained by the zeroth order method

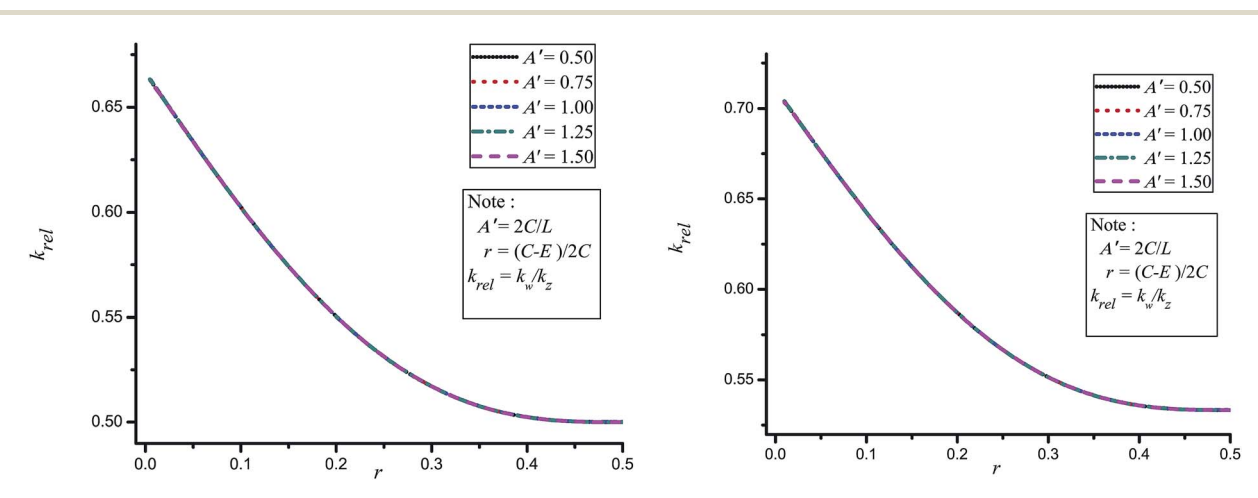


Fig. 11 Relation between $k_{\rm rel}=k_{\rm w}/k_{\rm z}$ and r=(C-E)/2C where (left) $\nu=0$ and (right) $\nu=0.25$.

Paper RSC Advances

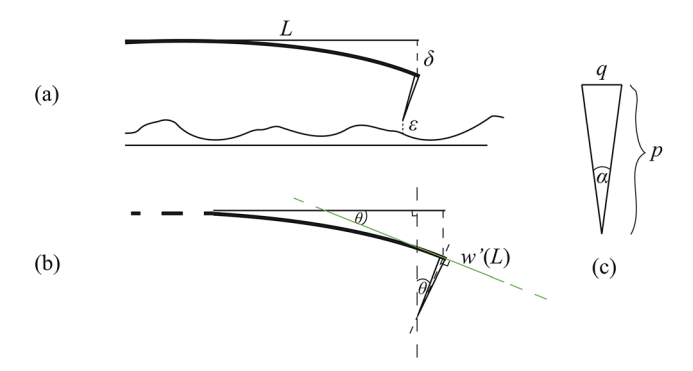


Fig. 12 (a) Geometry of cantilever, (b) relation between θ and $\omega'(L)$ where θ = arctan ($\omega'(L)$), and (c) geometry of cone with height p and base q.

given in (ref. 8) and $k_{\rm w}$ is that obtained in this study. We find that $k_{\rm z}$ is greater than $k_{\rm clv}$ and $k_{\rm sd}$, while $k_{\rm w}$ is less than $k_{\rm clv}$ and $k_{\rm sd}$ for all four types of cantilevers. The differences are due to the different calculations, and as shown in (ref. 12) who discuss the effect of air damping and loading position which also affect the spring constant. We comment that from Table 2, the value of $k_{\rm z}$ is larger than the value of $k_{\rm w}$ by approximately 30–50%. However, Sader *et al.* state that their spring constant $k_{\rm z}$ differs by 13%, $k_{\rm w}$ and when we decrease our $k_{\rm w}$ values by 13%, $k_{\rm w}$ differs from $k_{\rm clv}$ and $k_{\rm sd}$ by approximately 25–36%. This predicted difference is still large for a nano-scaled system where an angstrom change will make a major difference to the overall system.

In Fig. 11, we use A'=2C/L to indicate the different types of cantilevers and r=(C-E)/2C to represent the distance in the x-axis, in order to mimic the situation shown in Fig. 7 of Sader and White. Fig. 11 shows that $k_{\rm w}$ is 30–50% different from $k_{\rm z}$ as obtained in, but for small values of r, $k_{\rm w}$ and $k_{\rm z}$ are comparable. However, the value of $k_{\rm rel}=k_{\rm w}/k_{\rm z}$ is as much as 0.5 for a larger value of r, and it gives a difference of approximately 50%. Moreover, the relation between $k_{\rm rel}$ and r does not depend on A'. We believe that the differences

between the two methods occurs because the potential energy equation is assumed to have only a force applying at the end of the tip and does not have any boundary edge forces. Our method also predicts bending of the plate smoothly up to the third order derivatives at x = l. So, the curvature the cantilever does not arise and is assumed to be small in the zeroth order method. For the case of Poisson's ratio $\nu = 0.25$, the differences are also approximately 30-50%. Moreover, $k_{\rm rel}$ is around 0.53 when r is very large. In comparison with Fig. 7 presented in,8 both Fig. 11 (left) and Fig. 11 (right) are completely different, since Sader's graphs⁸ evidently show different behaviour for each A'. Additionally, when r tends to 0.5, their $k_{\rm rel}$ approaches unity whereas our $k_{\rm rel}$ approaches 0.5. We comment that when r is zero, there is a singular point, and that from a reduction of 13% difference in k_z , our k_w shows a 25-43% difference.

3.3 Mechanical cantilever system

Here, we consider the mechanical performance between the tip and the bending cantilever by employing both solutions obtained from the potential energy calculation and the bending behaviour. Type 1 and Type 4 cantilevers are modelled and investigated, and Fig. 12 shows the geometries of the cantilever and the tip. In Fig. 13, we employ the values $p = 17 \mu m$, $q = 4 \mu m$ so that $\alpha = 0.234$ rad. From the relation $\theta = \arctan(w'(L))$, we can plot energy *versus* bending distance δ and interspacing ε . We consider the negative bending energy $E_{\rm bend}$ because it can be easily compared to the magnitude of the potential energy E_{cp} . The mechanical cantilever operates when $E_{cp} \leq E_{bend}$. For Type 1 cantilever, the farthest bending distance δ is approximately 0.2 nm for which $\varepsilon = 0.206$ nm, and $\theta = 2.18 \times 10^{-6}$ rad, and for Type 4, we have $\delta = 0.09$ nm at $\varepsilon = 0.206$ nm and $\theta = 9.22 \times 10^{-6}$ rad. The energy of each type at maximum δ is approximately -2.35×10^{-21} J. The tip of the cantilever has an initial swing to detect the surface of the substrate and the length units of the cantilever are in micrometers whereas the bending distance units are in nanometers.

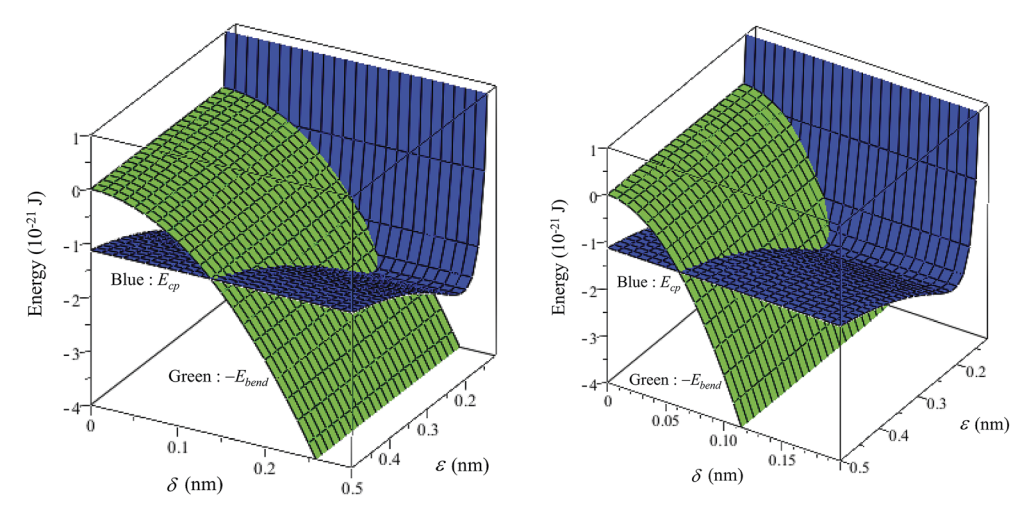


Fig. 13 Energy comparison, E_{cp} for cone and plane, and E_{bend} is potential energy in cantilever, (left) Type 1 and (right) Type 4 cantilevers.

RSC Advances Paper

4 Conclusion

Here a theoretical study of the AFM cantilever system is presented, employing the variational calculus and the Lennard-Jones potential to determine the bending behaviour of the system, and the calculation comprises two procedures. Firstly, we compute the energy between the silicon tip and the graphene plane, assuming the silicon tip is a cone, and it can act both vertical and inclined to the plane. Secondly, we solve the potential equation for the plate to deduce a bending equation, for which the solution describes the bending behaviour, and it can be used to determine the spring constant and the potential energy that is stored in the cantilever beam. We propose that the geometry of the cantilever is an isosceles trapezoid, mainly focusing on an V-shaped cantilever so as to compare our results with those of Sader *et al.*^{8,12} and Cleveland *et al.*¹⁰

In the first procedure, we obtain the energy equations of the right cone and that of the tilted cone. In the case of the tilted cone, when the tilted angle θ is zero, the energy equation gives rise to the energy of the right cone of the same cone angle α . Both cases have an equilibrium distance $\varepsilon_{\rm min}$ at $\left[B/(30A)\right]^{1/6}$. Moreover, the cone angle and the tilted angle do not effect the value of $\varepsilon_{\rm min}$ where it is obtained as 0.206 nm. Both cases are unstable if ε is less than 0.149 nm, and the different values of $\varepsilon_{\rm min}$ occur if and only if we use different materials for the tip and the plane.

In the second procedure, the bending profile tends to a parabola $(\delta/L^2)x^2$. For any given bending distance δ , L will be a dominant parameter that affects the bending profile. On comparison with the spring constant given in (ref. 12), our $k_{\rm w}$ gives a lower value while $k_{\rm z}$ given in (ref. 8) shows larger values for all types of cantilevers. By comparing between $k_{\rm z}$ and $k_{\rm w}$, the results show 30–50% difference and when r increases, this difference increases. Additionally, the 13% difference for $k_{\rm z}$ mentioned in (ref. 8) is reduced, but still gives 25–36% difference for our spring constant.

Finally, on combining the first and the second procedures to observe the energy relation, we choose a cone radius $\alpha=0.234$ rad and use the parameter values given in Table 1. We predict a maximum bending distance δ between 0.2 nm and 0.09 nm corresponding to tilted angles $\theta=2.18\times 10^{-6}$ rad and $\theta=9.22\times 10^{-6}$ rad for Type 1 and Type 4, respectively, and the energies arising from both procedures are -2.35×10^{-21} J.

Our method gives an alternative approach to determine the bending behaviour of the cantilever and the tip response to the surface. This analytical method is relevant in the determination of the distance, energy, and force that are the main considerations in any study of the mechanics of the system. Our approach gives a better understanding of the relations between the substrate surface, the bending distance and the properties of the surface. Moreover, this approach can be applied to any shape of the cantilever and any surface. For a given substrate, we can calculate the appropriate distance between the tip and the sample so as to fix the position of the cantilever to accommodate the bending angle. Further, if we know the surface level from the monitor and we know the bending distance or angle,

we can then predict the molecules on the substrate. In the theoretical analysis, our calculation utilizes the calculus of variation, and coordinate transformation of the atoms to model the cantilever system. The approach may involve some approximations but it gives a numerical solution that is faster than that obtained by computer simulation. Hence, we believe that the approach adopted here might be used in many future studies, not only for the cantilever system but also for any mechanical systems involving a scanning step, so that we might quickly determine a reliable solution by means of a simple mathematical formula.

Acknowledgements

Financial support from the Thailand Research Fund through the Royal Golden Jubilee Ph.D. Program (Grant No. PHD/0062/2555) is acknowledged. DB is also grateful for the support of the Thailand Research Fund (RSA5880003).

References

- 1 S. Kasas, N. H. Thomson, B. L. Smith, P. K. Hansma, J. Miklossy and H. G. Hansma, Biological Applications of the AFM: From Single Molecules to Organs, *International Journal of Imaging Systems and Technology*, 1997, **8**, 151161.
- 2 C. M. Franz and P. H. Puech, Atomic Force Microscopy: A Versatile Tool for Studying Cell Morphology, Adhesion and Mechanics, *Cell. Mol. Bioeng.*, 2008, 1, 289–300.
- 3 G. Binnig, C. F. Quate and C. Gerber, Atomic Force Microscope, *Phys. Rev. Lett.*, 1986, 56, 930–933.
- 4 H. J. Butt, B. Cappella and M. Kappl, Force measurements with the atomic force microscope: technique, interpretation and applications, *Surf. Sci. Rep.*, 2005, **59**, 1–152.
- 5 A. D. Slattery, A. J. Blanch, J. S. Quinton and C. T. Gibson, Accurate measurement of Atomic Force Microscope cantilever deflection excluding tip-surface contact with application to force calibration, *Ultramicroscopy*, 2013, **131**, 46–55.
- 6 R. Wagner, R. Moon, J. Pratt, G. Shaw and A. Raman, Uncertainty quantification in nanomechanical measurements using the atomic force microscope, *Nanotechnology*, 2011, 22, 455703.
- 7 A. D. Slattery, A. J. Blanch, J. S. Quinton and C. T. Gibson, Calibration of atomic force microscope cantilevers using standard and inverted static methods assisted by FIBmilled spatial markers, *Nanotechnology*, 2013, 24, 015710.
- 8 J. E. Sader and L. White, Theoretical analysis of the static deflection of plates for atomic force microscope applications, *J. Appl. Phys.*, 1993, 74, 1–9.
- 9 E. H. Mansfield, *The Bending and Stretching of Plates*, London, Pergamon Press Ltd., 1964.
- 10 J. P. Cleveland, S. Manne, D. Bocek and P. K. Hansma, A nondestructive method for determining the spring constant of cantilevers for scanning force microscopy, *Rev. Sci. Instrum.*, 1993, 64, 403–405.

Paper RSC Advances

11 W. F. Stokey, *Shock and Vibration Handbook*, McGraw-Hill, New York, 1989.

- 12 J. E. Sader, I. Larson, P. Mulvaney and L. R. White, Method for the calibration of atomic force microscope cantilevers, *Rev. Sci. Instrum.*, 1995, **66**, 3789–3798.
- 13 C. P. Green, H. Lioe, J. P. Cleveland, R. Proksch, P. Mulvaney and J. E. Sader, Normal and torsional spring constants of atomic force microscope cantilevers, *Rev. Sci. Instrum.*, 2004, 75, 1988–1996.
- 14 J. E. Sader, Parallel beam approximation for V-shaped atomic force, microscope cantilevers, *Rev. Sci. Instrum.*, 1995, **66**, 4583–4587.
- 15 B. W. Hoogenboom, P. L. T. M. Frederix, D. Fotiadis, H. J. Hug and A. Engel, Potential of interferometric cantilever detection and its application for SFM/AFM in liquids, *Nanotechnology*, 2008, 19, 1–6.
- 16 T. Fukuma, M. Kimura, K. Kobayashi, K. Matsushige and H. Yamada, Development of low noise cantilever deflection sensor for multienvironment frequency modulation atomic force microscopy, *Rev. Sci. Instrum.*, 2005, 76, 053704.
- 17 J. Cai, Q. Xia, Y. Luo, M. Y. Wang and L. Zhang, Optimal Design and Evaluation of Cantilever Probe for Multifrequency Atomic Force Microscopy, 11th World Congress on Structural and Multidisciplinary Optimisation, 2015.
- 18 R. M. D. Stevens, N. A. Frederick, B. L. Smith, G. D. Stucky DEM and P. K. Hansma, Carbon nanotubes as probes for atomic force microscopy, *Nanotechnology*, 2000, **11**, 1–5.
- 19 M. B. Viani, T. E. Schäffer, G. T. Paloczi, L. I. Pietrasanta, B. L. Smith, J. B. Thompson, *et al.*, Fast imaging and fast force spectroscopy of single biopolymers with a new atomic force microscope designed for small cantilevers, *Rev. Sci. Instrum.*, 1999, **70**, 4300–4303.
- 20 G. Schitter, K. J. A. ström, B. E. DeMartini, P. J. Thurner, K. L. Turner and P. K. Hansma, Design and Modeling of a High-Speed AFM-Scanner, *IEEE Transactions on Control Systems Technology*, 2007, vol. 15, pp. 906–915.

- 21 J. D. Li, J. Xie, W. Xue and D. M. Wu, Fabrication of cantilever with self-sharpening nano-silicon-tip for AFM applications, *Microsyst. Technol.*, 2013, **19**, 285–290.
- 22 Y. P. Song, S. Wu, L. Y. Xu, J. M. Zhang, D. J. D. Gonzalez, X. Fu, *et al.*, Calibration of the effective spring constant of ultra-short cantilevers for a high-speed atomic force microscope, *Meas. Sci. Technol.*, 2015, **26**, 1–11.
- 23 C. T. Gibson, D. A. Smith and C. J. Roberts, Calibration of silicon atomic force microscope cantilevers, *Nanotechnology*, 2005, **16**, 234–238.
- 24 J. E. Sader, J. A. Sanelli, B. D. Adamson, J. P. Monty, X. Wei, S. A. Crawford, *et al.*, Spring constant calibration of atomic force microscope cantilevers of arbitrary shape, *Rev. Sci. Instrum.*, 2012, 83, 103705.
- 25 A. D. Slattery, J. S. Quinton and C. T. Gibson, Atomic force microscope cantilever calibration using a focused ion beam, *Nanotechnology*, 2012, 23, 285704.
- 26 S. M. Cook, T. E. Schäffer, K. M. Chynoweth, M. Wigton, R. W. Simmonds and K. M. Lang, Practical implementation of dynamic methods for measuring atomic force microscope cantilever spring constants, *Nanotechnology*, 2006, 17, 2135–2145.
- 27 J. E. Sader, J. Lu and P. Mulvaney, Effect of cantilever geometry on the optical lever sensitivities and thermal noise method of the atomic force microscope, *Rev. Sci. Instrum.*, 2014, **85**, 113702.
- 28 A. D. Slattery, A. J. Blanch, V. Ejov, J. S. Quinton and C. T. Gibson, Spring constant calibration techniques for next-generation fast-scanning atomic force microscope cantilevers, *Nanotechnology*, 2014, 25, 335705.
- 29 A. K. Rappé, C. J. Casewit, K. S. Colwell, W. A. Goddard III and W. M. Skid, UFF, a Full Periodic Table Force Field for Molecular Mechanics and Molecular Dynamics Simulations, *J. Am. Chem. Soc.*, 1992, 114, 10024–10035.
- 30 B. J. Cox, N. Thamwattana and J. M. Hill, Mechanics of atoms and fullerenes in single-walled carbon nanotubes. I. Acceptance and suction energies, *Proc. R. Soc. A*, 2007, **463**, 461–476.



Contents lists available at ScienceDirect

Physica A





Mathematical model for drug molecules encapsulated in lipid nanotube



Sasipim Putthikorn^a, Duangkamon Baowan^{a,b,*}

- ^a Department of Mathematics, Faculty of Science, Mahidol University, Rama VI, Bangkok 10400, Thailand
- ^b Centre of Excellence in Mathematics, CHE, Si Ayutthaya Rd, Bangkok 10400, Thailand

HIGHLIGHTS

- Interaction energy between three shapes of DOX and lipid nanotube is studied.
- Lennard-Jones potential and continuous approximation are utilized to determine such energy.
- We find that a thin cylindrical DOX gives a maximum suction energy among other cases.
- The main results are mathematical expressions.

ARTICLE INFO

Article history:
Received 29 April 2015
Received in revised form 8 November 2015
Available online 22 May 2016

Keywords: Lipid nanotube Doxorubicin Lennard-Jones potential Suction energy

ABSTRACT

Lipid nanotube is considered as a nanocontainer for drug and gene delivery. It is important to understand a basic idea of the encapsulation process. In this paper, we use the Lennard-Jones potential function and the continuous approximation to explain the energy behaviour of three hollow shapes of Doxorubicin (DOX) clusters that are a sphere, a cylinder, and an ellipsoid interacting with the lipid nanotube. On assuming that the surface areas of the three structures are equal, we can find the minimum size of the lipid nanotube that encapsulates DOX inside by determining the suction energy. Moreover, we find that a long cylindrical drug provides the largest suction energy among other structures studied here due to the perfect fit between the cylindrical drug and the cylindrical tube. This investigation is the first step to develop the design of nanocapsule for medical application.

© 2016 Elsevier B.V. All rights reserved.

1. Introduction

One of the health problems occurring around the world is cancer, and there are a number of people who suffer and die from this disease [1,2]. Although cancer is currently cured by chemotherapy, the normal cells of human body are damaged by this treatment. With the emerging of technological innovation, drug delivery application has expensively been developed [3], where nanocarriers can carry drug to targeted cells. There are some advantages of nanocarriers such as to reduce the harmful and to decrease the toxic on healthy cells. In this paper, we employ the lipid nanotube as a carrier to deliver Doxorubicin to the targeted cells.

Doxorubicin (DOX) is used as a chemotherapy drug. Due to the fact that treating by DOX causes damage to human tissue, many researchers attempt to transport DOX to the targeted cells without the side effect. Meng et al. [4] employ mesoporous silica nanoparticle as a drug carrier to deliver DOX and Pgp siRNA to a drug-resistant cancer cell line (KB-V1 cells).

^{*} Corresponding author at: Department of Mathematics, Faculty of Science, Mahidol University, Rama VI, Bangkok 10400, Thailand. E-mail address: duangkamon.bao@mahidol.ac.th (D. Baowan).

Lu et al. [5] use the multi-walled carbon nanotubes (MWCNTs) and iron oxide magnetic nanoparticles to transport DOX to the cancer cells. Their results indicate that DOX encapsulated in MWCNTs can destroy cancer cells more efficient than free DOX. Moreover, Meng et al. [6] utilize single-walled carbon nanotubes (SWNTs) as a drug vehicle to carry DOX to cancer tissue, and they find the highly efficient DOX loading onto SWNTs.

Zhou et al. [7] describe that the lipid nanotube is an open-ended and hollow cylinder consisting of rolled-up bilayer membrane due to the self-assembling of lipid molecules in lipid media. The lipid nanotube has several template-synthesized such as nanotubes [8], concentric tubular hybrids [9], complex helical architectures [10] as well as one-dimensional arrays of quantum dots where its diameter and length can be controlled. Besides, Shimizu [8] finds that dimensions including inner and outer diameters of the lipid nanotube can be controlled by the self-assembly of amphiphilic lipid monomers. Consequently, it may be used as a nanocarrier for the encapsulation of nanomaterials and biomolecules.

Another important topic on the drug delivery system is the drug release. Leo et al. [11] utilize the dynamic dialysis technique to evaluate the drug unload for the doxorubicin (DXR)-gelatin nanoparticle conjugates. Further, Liu et al. [12] study the system of DOX contained inside single-walled carbon nanotube with the poly(ethylene glycol) (PEG) decoration. They report that the complex nanocontainer is sensitive to the acidic solution and the drug can release rapidly. Dali et al. [13] synthesis the supramolecular amphiphilic block copolymers by the formation of multiple hydrogen interactions between adenine-terminated poly(ε -caprolactone) (PCL-A) and uracil-terminated poly(ethylene glycol) (PEG-U) so that the constructed copolymers can self-assemble into the water-stable micelles. These micelles can unload DOX at the pH of 5.0 that is faster than physiological pH. Here as a first step to study the drug delivery system, we focus on the uptake behaviour of the lipid nanotube containing the DOX molecule.

In terms of mathematical model, Baowan et al. [14] study the toxicity of a C_{60} fullerene by investigating the penetration of C_{60} through the lipid bilayer. They use the Lennard-Jones potential function and the continuous approximation to calculate the total energy of the system. In addition, Baowan et al. [15] compute the interaction energy between either gold or silver spherical nanoparticle and the lipid nanotube. Cox et al. [16,17] study the energy behaviour of the spherical and spheroidal fullerenes interacting with the carbon nanotube, and their results demonstrate that those nanoparticles can be encapsulated in the tube.

Here, we employ the same concept proposed by Baowan et al. [14] to investigate the encapsulation of three hollow shapes of the DOX which are a sphere, a cylinder and an ellipsoid entering the lipid nanotube. Further, we focus on the interaction energy between the nanotube and those three shapes with the hollow structure, and determine the optimal radius of the lipid nanotube encapsulating the different shapes of the DOX drug molecule. We comment that due to the complicated chemical structure of the DOX, more sophisticated mathematical derivation is required.

In the following section, the Lennard-Jones potential function and the continuous approximation used to calculate the interaction energy between the DOX and the lipid nanotube are described. The mathematical derivation and the interaction energy of the DOX and the lipid nanotube are presented in Section 3. Finally, the numerical results are reported and the findings are summarized.

2. Interaction energy and continuous approximation

The Lennard-Jones potential function is widely used to approximate the interaction energy between two non-bonded atoms. The Lennard-Jones function is of the form

$$\Phi = -\frac{A}{\rho^6} + \frac{B}{\rho^{12}},\tag{1}$$

where ρ represents the distance between two typical non-bonded atoms, A and B denote attractive and repulsive Lennard-Jones constants, respectively. Since $A=4\epsilon\sigma^6$ and $B=4\epsilon\sigma^{12}$ where ϵ is the well depth and σ is the van der Waals diameter, then (1) can be rewritten as

$$\Phi = 4\epsilon \left[-\left(\frac{\sigma}{\rho}\right)^6 + \left(\frac{\sigma}{\rho}\right)^{12} \right].$$

The interaction energy between two non-bonded molecules may be determined by using the continuous approximation where atoms at discrete locations on the molecule are assumed to be uniformly distributed over the surface or the volume of the molecule. Therefore, the total interaction energy can be written as

$$E = \eta_1 \eta_2 \int_{\Sigma_1} \int_{\Sigma_2} \left(-\frac{A}{\rho^6} + \frac{B}{\rho^{12}} \right) d\Sigma_2 d\Sigma_1,$$

where η_1 and η_2 denote the mean surface or the mean volume densities of atoms on each molecule and ρ is the distance between two typical surface or two typical volume elements d Σ_1 and d Σ_2 . Moreover, we define the integral I_n as

$$I_n = \int_{\Sigma_1} \int_{\Sigma_2} \rho^{-2n} d\Sigma_2 d\Sigma_1, \quad n = 3, 6,$$

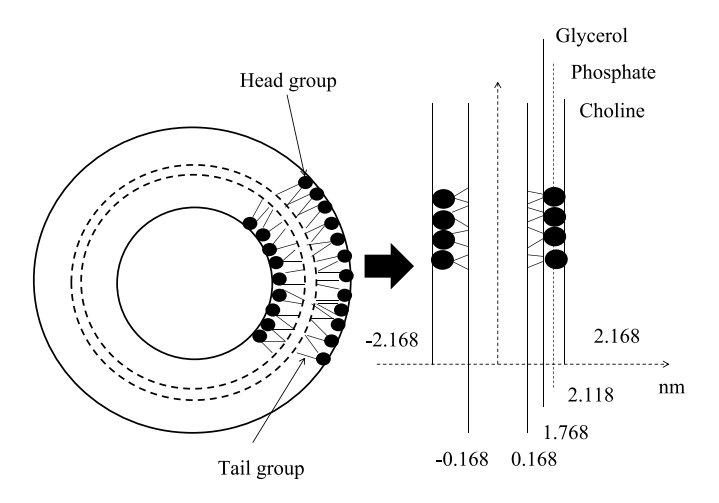


Fig. 1. Schematic of lipid nanotube.

Table 1The values of parameters used in this work.

Atom type	ϵ (kJ/mol)	σ (nm)	η (nm ⁻²)
Q_o	5.000	0.4700	3.13×10^{-4}
Q_a	5.600	0.4700	3.13×10^{-4}
N_a	4.500	0.4700	3.13×10^{-4}
C_1	2.300	0.4700	7.81×10^{-4}

then the total molecular interaction energy can be rewritten as

$$E = \eta_1 \eta_2 (-AI_3 + BI_6). \tag{2}$$

Here, we focus on the radius of the lipid nanotube giving the maximum suction energy. The suction energy proposed by Cox et al. [18] is the total interaction energy on the DOX molecule entering the nanotube. The suction energy is defined by

$$W = \int_{-\infty}^{\infty} F(Z) dZ = -\int_{-\infty}^{\infty} \frac{\partial E}{\partial Z} dZ = E(-\infty) - E(\infty), \tag{3}$$

where E is given by (2).

The loading capacity of drugs or other nanoparticles in vehicle has been investigated using variety of intermolecular interactions, which are reviewed in Ref. [19]. In this study, the interaction energy between DOX and lipid nanotube is dominated by the van der Waals energy because the carrier is not decorated with the special chemical groups that may impact on the interaction energy of the system. We can ignore the electrostatic interaction due to the zero point charge on the DOX in vacuum environment [20]. Further, the van der Waals interaction plays an important role comparing to the electrostatic energy as described in Ref. [21].

The Dipalmitoylphosphatidylcholine (DPPC) lipid is employed as a lipid membrane and its coarse grain structure proposed by Martini et al. [22] is utilized in this work. The lipid nanotube is composed of the head group, the intermediate layer and the tail group. In terms of the head group, there are choline (Q_a) and phosphate (Q_a) groups. A glycerol group (N_a) is an intermediate layer and the carbon chain (C_1) is represented as a tail group. A schematic model of the lipid nanotube is illustrated in Fig. 1, where the head group thickness and tail group thickness are taken to be 0.4 nm and 1.6 nm, respectively. Furthermore, Table 1 shows the value of the well depth ϵ and the van der Waals diameter σ for Q_o , Q_a , N_a and C_1 , which are taken from Martini et al. [22]. The attractive (A) and the repulsive (B) constants can be calculated from the proportional of atoms on the drug molecule and that of atoms on each layer of the lipid nanotube. Hence, an empirical mixing rule is presented to evaluate the constants A and B for the interaction between DOX and each layer of the tube. The constants used in this work can be found in Sumatpipat et al. [23] and restated in Table 2.

In this study, we utilize DOX, of which a chemical formula is $C_{27}H_{29}NO_{11}$, as a drug molecule entering the lipid nanotube. The mean atomic surface of this DOX is 0.3047 nm⁻² [23].

3. Mathematical derivations

Here, we investigate the interaction energy between the three hollow shapes of DOX and the lipid nanotube. In terms of the lipid nanotube, it is assumed to be six layers which are consisted of two head groups, two intermediate layers and two tail groups. The head group and the tail group are considered as a cylinder with thickness *l* while the intermediate layer is modelled as a cylindrical surface. Consequently, the total interaction energy for each shape of the drug comprises:

Table 2Attractive and repulsive constants for DOX interacting with three layers of lipid nanotube taken from Ref. [23].

Type of layer	$A (kJ nm^6 mol^{-1})$	$B(10^{-5} \text{ kJ nm}^6 \text{ mol}^{-1})$
Head (H)	0.01778	6.90489
Intermediate (I)	0.01639	6.36178
Tail (T)	0.01172	4.54817

- 1. Interaction energies between the drug molecule and the two head groups using cylindrical volume integral.
- 2. Interaction energies between the drug molecule and the two intermediate layers using cylindrical surface integral.
- 3. Interaction energies between the drug molecule and the two tail groups using cylindrical volume integral.

In the following subsection, we examine the energy behaviour for a spherical drug molecule. Analytical calculations for a cylindrical shape and an ellipsoidal shape of DOX are given in Sections 3.2 and 3.3, respectively.

3.1. Spherical drug molecule

In the case of a spherical drug molecule, we determine the interaction energy arising from the surface of the drug. In order to obtain the interaction energy between a spherical molecule and the nanotube, we start by considering the energy of a single atom interacting with the surface of a spherical molecule. The interaction energy between a single atom and a spherical surface is defined by

$$E^1 = \eta_s \int_{s} \Phi(\rho) ds,$$

where η_s is the mean surface density of the sphere. In the spherical coordinate, it may deduce

$$E^{1} = \eta_{s} \int_{-\pi}^{\pi} \int_{0}^{\pi} \Phi(\rho) a^{2} \sin \phi d\phi d\theta,$$

where a denotes a radius of a spherical molecule and δ is the distance between a point and a centre of the sphere as shown in Fig. 2. Now, we determine

$$I_n^1 = \int_{-\pi}^{\pi} \int_0^{\pi} \frac{a^2 \sin \phi}{\rho^{2n}} d\phi d\theta, \quad n = 3, 6.$$

The coordinates of a point are given by (0,0,0) while the coordinates of the surface of the sphere are represented by $(a\cos\theta\sin\phi,a\sin\phi,a\cos\phi+\delta)$. Thus, the distance between a surface of a spherical molecule and a point is

$$\rho^2 = (a\cos\theta\sin\phi)^2 + (a\sin\theta\sin\phi)^2 + (a\cos\phi + \delta)^2 = a^2 + \delta^2 + 2a\delta\cos\phi.$$

Here, the integral I_n^1 becomes

$$I_n^1 = \int_{-\pi}^{\pi} \int_0^{\pi} \frac{a^2 \sin \phi}{(a^2 + \delta^2 + 2a\delta \cos \phi)^n} d\phi d\theta$$
$$= 2\pi \int_0^{\pi} \frac{a^2 \sin \phi}{(a^2 + \delta^2 + 2a\delta \cos \phi)^n} d\phi.$$

On letting $u = a^2 + \delta^2 + 2a\delta \cos \phi$, we may deduce

$$I_n^1 = \frac{a\pi}{\delta} \int_{(\delta - a)^2}^{(\delta + a)^2} \frac{1}{u^n} du$$

= $\frac{a\pi}{\delta(n-1)} \left(\frac{1}{(\delta - a)^{2(n-1)}} - \frac{1}{(\delta + a)^{2(n-1)}} \right).$

After substituting n = 3 and n = 6, we obtain the integral I_n^1 expressed in terms of J_m

$$I_3^1[J_m] = 4\pi a^2(J_3 + 2a^2J_4),\tag{4}$$

$$I_6^1[J_m] = \frac{4\pi a^2}{5} (5J_6 + 80a^2J_7 + 336a^4J_8 + 512a^6J_9 + 256a^8J_{10}), \tag{5}$$

where

$$J_m = \frac{1}{(\delta^2 - a^2)^m},\tag{6}$$

and m represents a positive integer of the power of the polynomials shown in (4) and (5).

Next, we determine the interaction energy between a spherical surface of the drug molecule and the tube where another surface or another volume integral for a cylindrical nanotube is evaluated.

 $(a\cos\theta\sin\phi, a\sin\theta\sin\phi, a\cos\phi+\delta)$

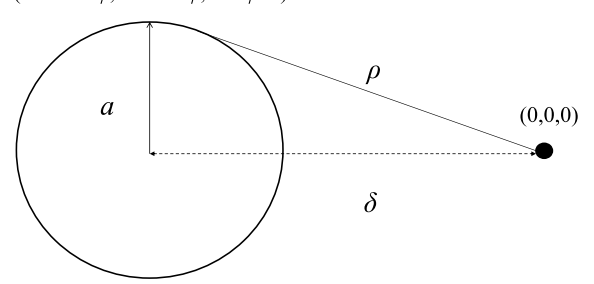


Fig. 2. Spherical surface interacting with single atom.

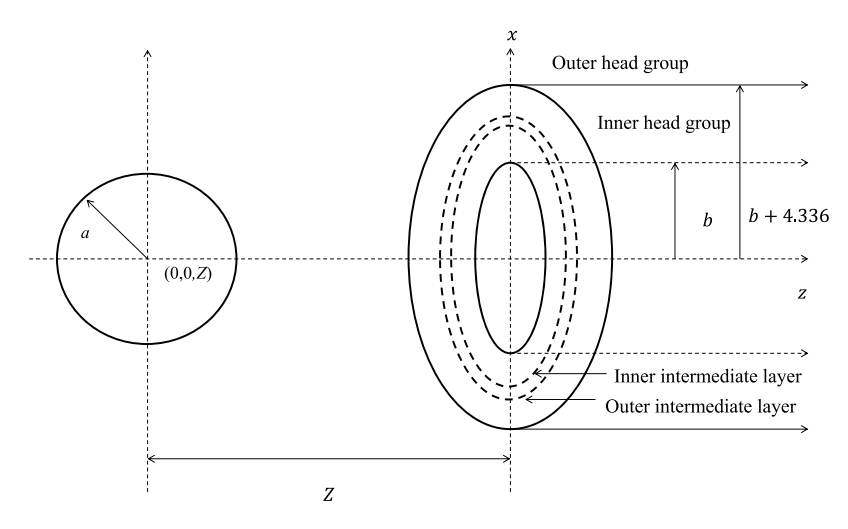


Fig. 3. Spherical molecule entering the lipid nanotube.

3.1.1. Surface integral of a cylindrical tube

In the Cartesian coordinate system, the centre of a sphere is assumed to be located at (0,0,Z) and the typical point on a cylindrical surface of radius b is given by $(b\cos\theta,b\sin\theta,z)$ then the distance $\delta^2=b^2+(z-Z)^2$. A schematic model for this interaction is illustrated in Fig. 3. Thereby, we need to calculate

$$J_m^s = \eta_s^* \int_{-\pi}^{\pi} \int_0^{L_1} \frac{b}{[b^2 + (z - Z)^2 - a^2]^m} dz d\theta$$
$$= 2\eta_s^* b\pi \int_0^{L_1} \frac{1}{[b^2 + (z - Z)^2 - a^2]^m} dz,$$

where η_s^* is the mean surface density of the lipid nanotube and L_1 denotes the length of the tube. We let $z - Z = \sqrt{b^2 - a^2} \tan x$, then we may deduce

$$J_{m}^{s} = 2\eta_{s}^{*}b\pi \int_{-\tan^{-1}\left(\frac{L_{1}-Z}{\sqrt{b^{2}-a^{2}}}\right)}^{\tan^{-1}\left(\frac{L_{1}-Z}{\sqrt{b^{2}-a^{2}}}\right)} \frac{\sqrt{b^{2}-a^{2}}\sec^{2}x}{[b^{2}+(b^{2}-a^{2})\tan^{2}x-a^{2}]^{m}} dx$$

$$= \frac{2\eta_{s}^{*}b\pi}{(b^{2}-a^{2})^{m-1/2}} \int_{-\tan^{-1}\left(\frac{L_{1}-Z}{\sqrt{b^{2}-a^{2}}}\right)}^{\tan^{-1}\left(\frac{L_{1}-Z}{\sqrt{b^{2}-a^{2}}}\right)} \cos^{2(m-1)}x dx. \tag{7}$$

From Gradshteyn and Ryzhik [24] on page 153, we have

$$\int \cos^{2(m-1)} x dx = \frac{1}{2^{2(m-1)}} \left[\binom{2(m-1)}{(m-1)} x + \sum_{k=0}^{m-2} \binom{2(m-1)}{k} \frac{\sin[(2m-2k-2)x]}{(m-k-1)} \right]. \tag{8}$$

On substituting (8) into (7) for any given m, the analytical expansion for J_m^s can be determined.

3.1.2. Volume integral of a cylindrical tube with thickness l

For this case, the integral J_m is of the form

$$J_{m}^{v} = \eta_{v}^{*} \int_{-\pi}^{\pi} \int_{b}^{b+l} \int_{0}^{L_{1}} \frac{r}{[r^{2} + (z - Z)^{2} - a^{2}]^{m}} dz dr d\theta$$
$$= 2\eta_{v}^{*} \pi \int_{b}^{b+l} \int_{0}^{L_{1}} \frac{r}{[r^{2} + (z - Z)^{2} - a^{2}]^{m}} dz dr,$$

where η_v^* denotes the mean volume density of the lipid nanotube and l represents the thickness of the tube. On letting $u = r^2 + (z - Z)^2 - a^2$, the integral J_m^v becomes

$$J_m^v = \frac{\eta_v^* \pi}{(1-m)} \int_0^{L_1} \left(\frac{1}{[(b+l)^2 + (z-Z)^2 - a^2]^{m-1}} - \frac{1}{[b^2 + (z-Z)^2 - a^2]^{m-1}} \right) dz.$$

Next, we substitute $z-Z=\sqrt{(b+l)^2-a^2}\tan x$ to the first term and $z-Z=\sqrt{b^2-a^2}\tan x$ to the second term, hence, the integral J_m^v is

$$J_{m}^{v} = \frac{\eta_{v}^{*}\pi}{(1-m)} \left[\frac{1}{[(b+l)^{2} - a^{2}]^{m-3/2}} \int_{-\tan^{-1}\left(\frac{L_{1}-Z}{\sqrt{(b+l)^{2}-a^{2}}}\right)}^{\tan^{-1}\left(\frac{L_{1}-Z}{\sqrt{(b+l)^{2}-a^{2}}}\right)} \cos^{2(m-2)} x dx - \frac{1}{(b^{2} - a^{2})^{m-3/2}} \int_{-\tan^{-1}\left(\frac{L_{1}-Z}{\sqrt{b^{2}-a^{2}}}\right)}^{\tan^{-1}\left(\frac{L_{1}-Z}{\sqrt{b^{2}-a^{2}}}\right)} \cos^{2(m-2)} x dx \right],$$

which can be analytically calculated using (8).

Finally, we need to consider the suction energy defined by (3), and on taking a limit of the interaction energy from $Z = -\infty$ to $Z = \infty$, the suction energy is obtained.

3.2. Cylindrical drug molecule

We are interested in both the cylindrical surface area and the two circular ends of the cylindrical drug molecule. Here, the total length of the cylindrical drug molecule is denoted by $2L_2$, the radius of the drug is assumed to be a, and there are four configurations of the cylindrical shape studied here.

3.2.1. Cylindrical surface area of drug molecule

The centre of the drug molecule is assumed to be located at (0,0,Z). In the Cartesian coordinates, atoms on a cylindrical surface of the drug and a lipid nanotube of radius b are given by $(a\cos\theta_1,a\sin\theta_1,z_1)$ and $(b\cos\theta_2,b\sin\theta_2,z_2)$, respectively. Now, the distance ρ between the two surface elements is given by

$$\rho^2 = (b\cos\theta_2 - a\cos\theta_1)^2 + (b\sin\theta_2 - a\sin\theta_1)^2 + (z_2 - z_1)^2$$

= $(b - a)^2 + (z_2 - z_1)^2 + 4ab\sin^2\left(\frac{\theta_2 - \theta_1}{2}\right)$.

The schematic model for this system is shown in Fig. 4. Using cylindrical surface integral, the interaction energy between a cylindrical surface of the drug and that of the tube is given by

$$E_1^{2s} = ab\eta_s \eta_s^* \int_{S_1} \int_{S_2} \Phi(\rho) dS_2 dS_1,$$

where again η_s is the mean surface density of the drug and η_s^* represents the mean surface density of the tube. Next, we define

$$I_n^2 = \int_{-\pi}^{\pi} \int_{-\pi}^{\pi} \int_0^{L_1} \int_{Z-L_2}^{Z+L_2} \frac{\mathrm{d}z_1 \mathrm{d}z_2 \mathrm{d}\theta_1 \mathrm{d}\theta_2}{\left[(b-a)^2 + (z_2 - z_1)^2 + 4ab \sin^2\left(\frac{\theta_2 - \theta_1}{2}\right) \right]^n}.$$
 (9)

To evaluate the above integral I_n^2 , we let $\omega^2=(b-a)^2+4ab\sin^2\left(\frac{\theta_2-\theta_1}{2}\right)$ and define

$$I_n^{2*} = \int_0^{L_1} \int_{Z-L_2}^{Z+L_2} \frac{\mathrm{d} z_1 \mathrm{d} z_2}{[\omega^2 + (z_2 - z_1)^2]^n}.$$

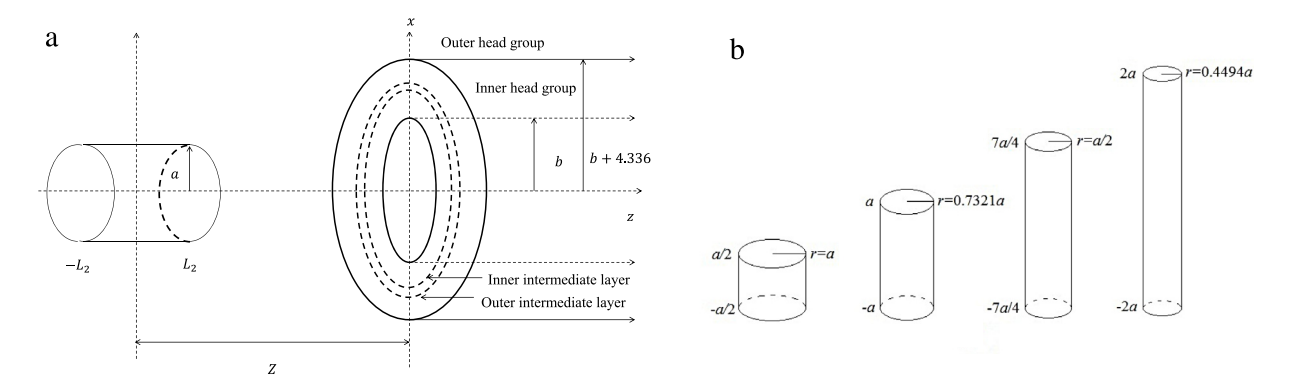


Fig. 4. (a) Cylindrical molecule entering the lipid nanotube and (b) four possible structures of cylindrical drug molecule.

On setting $z_2 - z_1 = \omega \tan \psi$, we acquire

$$I_n^{2*} = \int_{Z-L_2}^{Z+L_2} \int_{-\tan^{-1}\left(\frac{z_1}{\omega}\right)}^{\tan^{-1}\left(\frac{L_1-z_1}{\omega}\right)} \frac{\omega \sec^2 \psi}{(\omega^2 + \omega^2 \tan^2 \psi)^n} d\psi dz_1 = \frac{1}{\omega^{2n-1}} \int_{Z-L_2}^{Z+L_2} \int_{-\tan^{-1}\left(\frac{z_1}{\omega}\right)}^{\tan^{-1}\left(\frac{L_1-z_1}{\omega}\right)} \cos^{2(n-1)} \psi d\psi dz_1,$$

which may be analytically determined by using (8). For n = 3, we have

$$\begin{split} I_3^{2*} &= \frac{1}{\omega^5} \int_{z-L_2}^{z+L_2} \left[\frac{3}{8} \tan^{-1} \left(\frac{L_1 - z_1}{\omega} \right) + \frac{3}{8} \tan^{-1} \left(\frac{z_1}{\omega} \right) + \frac{3\omega(L_1 - z_1)}{8[\omega^2 + (L_1 - z_1)^2]} \right. \\ &\quad + \frac{3\omega z_1}{8(\omega^2 + z_1^2)} + \frac{\omega^3(L_1 - z_1)}{4[\omega^2 + (L_1 - z_1)^2]^2} + \frac{\omega^3 z_1}{4(\omega^2 + z_1^2)^2} \right] \! dz_1. \end{split}$$

On substituting $t_1=rac{L_1-z_1}{\omega}$ and $t_2=rac{z_1}{\omega}$, and changing the integration variable, we may deduce

$$\begin{split} I_3^{2*} &= \frac{1}{\omega^4} \left[\frac{3(L_1 + L_2 - Z)}{8\omega} \tan^{-1} \left(\frac{L_1 + L_2 - Z}{\omega} \right) - \frac{\omega^2}{8[\omega^2 + (L_1 + L_2 - Z)^2]} \right. \\ &\quad \left. - \frac{3(L_1 - L_2 - Z)}{8\omega} \tan^{-1} \left(\frac{L_1 - L_2 - Z}{\omega} \right) + \frac{\omega^2}{8[\omega^2 + (L_1 - L_2 - Z)^2]} + \frac{3(Z + L_2)}{8\omega} \tan^{-1} \left(\frac{Z + L_2}{\omega} \right) \right. \\ &\quad \left. - \frac{\omega^2}{8[\omega^2 + (Z + L_2)^2]} - \frac{3(Z - L_2)}{8\omega} \tan^{-1} \left(\frac{Z - L_2}{\omega} \right) + \frac{\omega^2}{8[\omega^2 + (Z - L_2)^2]} \right]. \end{split}$$

In the case of I_6^{2*} , we utilize the same technique as described for I_3^{2*} to obtain

$$\begin{split} I_6^{2*} &= \frac{1}{\omega^{10}} \bigg[\frac{63(L_1 + L_2 - Z)}{256\omega} \tan^{-1} \bigg(\frac{L_1 + L_2 - Z}{\omega} \bigg) - \frac{21\omega^2}{256[\omega^2 + (L_1 + L_2 - Z)^2]} - \frac{21\omega^4}{640[\omega^2 + (L_1 + L_2 - Z)^2]^2} \\ &- \frac{3\omega^6}{160[\omega^2 + (L_1 + L_2 - Z)^2]^3} - \frac{\omega^8}{80[\omega^2 + (L_1 + L_2 - Z)^2]^4} - \frac{63(L_1 - L_2 - Z)}{256\omega} \tan^{-1} \bigg(\frac{L_1 - L_2 - Z}{\omega} \bigg) \\ &+ \frac{21\omega^2}{256[\omega^2 + (L_1 - L_2 - Z)^2]} + \frac{21\omega^4}{640[\omega^2 + (L_1 - L_2 - Z)^2]^2} + \frac{3\omega^6}{160[\omega^2 + (L_1 - L_2 - Z)^2]^3} \\ &+ \frac{\omega^8}{80[\omega^2 + (L_1 - L_2 - Z)^2]^4} + \frac{63(Z + L_2)}{256\omega} \tan^{-1} \bigg(\frac{Z + L_2}{\omega} \bigg) - \frac{21\omega^2}{256[\omega^2 + (Z + L_2)^2]} \\ &- \frac{21\omega^4}{640[\omega^2 + (Z + L_2)^2]^2} \\ &- \frac{3\omega^6}{160[\omega^2 + (Z + L_2)^2]^3} - \frac{\omega^8}{80[\omega^2 + (Z + L_2)^2]^4} - \frac{63(Z - L_2)}{256\omega} \tan^{-1} \bigg(\frac{Z - L_2}{\omega} \bigg) + \frac{21\omega^2}{256[\omega^2 + (Z - L_2)^2]} \\ &+ \frac{21\omega^4}{640[\omega^2 + (Z - L_2)^2]^2} + \frac{3\omega^6}{160[\omega^2 + (Z - L_2)^2]^3} + \frac{\omega^8}{80[\omega^2 + (Z - L_2)^2]^4} \bigg]. \end{split}$$

Finally, there are other two integrals for I_3^2 and I_6^2 that must be determined which are

$$C_m = \int_{-\pi}^{\pi} \int_{-\pi}^{\pi} \frac{\mathrm{d}\theta_1 \mathrm{d}\theta_2}{\omega^m (\omega^2 + G_i^2)^n},$$

$$D_m = \int_{-\pi}^{\pi} \int_{-\pi}^{\pi} \frac{1}{\omega^m} \tan^{-1} \left(\frac{G_i}{\omega}\right) \mathrm{d}\theta_1 \mathrm{d}\theta_2, \quad i = 1, 2, 3, 4,$$

where m and n denote the positive integers, $\omega^2 = (b-a)^2 + 4ab \sin^2\left(\frac{\theta_2 - \theta_1}{2}\right)$ and $G_1 = Z + L_2$, $G_2 = Z - L_2$, $G_3 = L_1 + L_2 - Z$, and $G_4 = L_1 - L_2 - Z$. On letting

$$C_m^* = \int_{-\pi}^{\pi} \frac{\mathrm{d}\theta_2}{\left[\mu + \nu \sin^2\left(\frac{\theta_2 - \theta_1}{2}\right)\right]^{m/2} \left[\mu + \nu \sin^2\left(\frac{\theta_2 - \theta_1}{2}\right) + G_i^2\right]^n},$$

where $\mu = (b-a)^2$ and $\nu = 4ab$, we can show that C_m^* is independent of θ_1 which can be demonstrated as

$$\frac{dC_m^*}{d\theta_1} = \int_{-\pi}^{\pi} -\frac{\partial}{\partial \theta_2} \left(\frac{1}{\left[\mu + \nu \sin^2\left(\frac{\theta_2 - \theta_1}{2}\right)\right]^{m/2} \left[\mu + \nu \sin^2\left(\frac{\theta_2 - \theta_1}{2}\right) + G_i^2\right]^n} \right) d\theta_2 = 0.$$

Hence, θ_1 may be given as a constant so we deduce

$$C_m = 8\pi \int_0^{\frac{\pi}{2}} \frac{\mathrm{d}x}{(\omega^*)^m [(\omega^*)^2 + G_i^2]^n}.$$

Similarly, D_m is obtained as

$$D_m = 8\pi \int_0^{\frac{\pi}{2}} \frac{1}{(\omega^*)^m} \tan^{-1} \left(\frac{G_i}{\omega^*} \right) \mathrm{d}x,$$

where $(\omega^*)^2 = (b-a)^2 + 4ab\sin^2 x$. Therefore, once C_m and D_m are substituted back to I_3^2 and I_6^2 defined by (9), we obtain the interaction energy between the surface of the cylindrical drug and the lipid nanotube that is given by

$$E_1^{2s} = ab\eta_s\eta_s^*(-AI_3^2 + BI_6^2).$$

Next, we consider the interaction energy for a cylindrical surface of the drug molecule interacting with the lipid nanotube of thickness *l* that can be given by

$$E_1^{2v} = a\eta_s \eta_v^* \int_V \int_S r \Phi(\rho) dS dV,$$

where η_v^* denotes the mean volume density of the tube and the distance ho becomes

$$\rho^{2} = (r - a)^{2} + (z_{2} - z_{1})^{2} + 4ar \sin^{2} \left(\frac{\theta_{2} - \theta_{1}}{2}\right),$$

where $r \in [b, b+l]$. Now, we need to determine

$$I_n^3 = \int_{-\pi}^{\pi} \int_{-\pi}^{\pi} \int_b^{b+l} \int_0^{L_1} \int_{Z-L_2}^{Z+L_2} \frac{r dz_1 dz_2 dr d\theta_1 d\theta_2}{\left[(r-a)^2 + (z_2 - z_1)^2 + 4ar \sin^2 \left(\frac{\theta_2 - \theta_1}{2} \right) \right]^n}.$$

Similar with the determination described for I_n^2 , we finally obtain

$$\begin{split} I_3^3 &= 8\pi \int_0^{\frac{\pi}{2}} \int_b^{b+l} \frac{r}{\lambda^4} \bigg[\frac{3(L_1 + L_2 - Z)}{8\lambda} \tan^{-1} \bigg(\frac{L_1 + L_2 - Z}{\lambda} \bigg) - \frac{\lambda^2}{8[\lambda^2 + (L_1 + L_2 - Z)^2]} \\ &- \frac{3(L_1 - L_2 - Z)}{8\lambda} \tan^{-1} \bigg(\frac{L_1 - L_2 - Z}{\lambda} \bigg) + \frac{\lambda^2}{8[\lambda^2 + (L_1 - L_2 - Z)^2]} + \frac{3(Z + L_2)}{8\lambda} \tan^{-1} \bigg(\frac{Z + L_2}{\lambda} \bigg) \\ &- \frac{\lambda^2}{8[\lambda^2 + (Z + L_2)^2]} - \frac{3(Z - L_2)}{8\lambda} \tan^{-1} \bigg(\frac{Z - L_2}{\lambda} \bigg) + \frac{\lambda^2}{8[\lambda^2 + (Z - L_2)^2]} \bigg] dr dx, \end{split}$$

and

$$\begin{split} & l_{6}^{3} = 8\pi \int_{0}^{\frac{\pi}{2}} \int_{b}^{b+l} \frac{r}{\lambda^{10}} \bigg[\frac{63(L_{1} + L_{2} - Z)}{256\lambda} \tan^{-1} \bigg(\frac{L_{1} + L_{2} - Z}{\lambda} \bigg) \\ & - \frac{21\lambda^{2}}{256[\lambda^{2} + (L_{1} + L_{2} - Z)^{2}]} - \frac{21\lambda^{4}}{640[\lambda^{2} + (L_{1} + L_{2} - Z)^{2}]^{2}} \\ & - \frac{3\lambda^{6}}{160[\lambda^{2} + (L_{1} + L_{2} - Z)^{2}]^{3}} - \frac{\lambda^{8}}{80[\lambda^{2} + (L_{1} + L_{2} - Z)^{2}]^{4}} - \frac{63(L_{1} - L_{2} - Z)}{256\lambda} \tan^{-1} \bigg(\frac{L_{1} - L_{2} - Z}{\lambda} \bigg) \\ & + \frac{21\lambda^{2}}{256[\lambda^{2} + (L_{1} - L_{2} - Z)^{2}]} + \frac{640[\lambda^{2} + (L_{1} - L_{2} - Z)^{2}]^{2}}{640[\lambda^{2} + (L_{1} - L_{2} - Z)^{2}]^{2}} + \frac{3\lambda^{6}}{160[\lambda^{2} + (L_{1} - L_{2} - Z)^{2}]^{3}} \\ & + \frac{\lambda^{8}}{80[\lambda^{2} + (L_{1} - L_{2} - Z)^{2}]^{4}} + \frac{63(Z + L_{2})}{256\lambda} \tan^{-1} \bigg(\frac{Z + L_{2}}{\lambda} \bigg) \\ & - \frac{21\lambda^{2}}{256[\lambda^{2} + (Z + L_{2})^{2}]} - \frac{21\lambda^{4}}{640[\lambda^{2} + (Z + L_{2})^{2}]^{4}} \\ & - \frac{3\lambda^{6}}{160[\lambda^{2} + (Z + L_{2})^{2}]^{3}} - \frac{\lambda^{8}}{80[\lambda^{2} + (Z + L_{2})^{2}]^{4}} - \frac{63(Z - L_{2})}{256\lambda} \tan^{-1} \bigg(\frac{Z - L_{2}}{\lambda} \bigg) + \frac{21\lambda^{2}}{256[\lambda^{2} + (Z - L_{2})^{2}]} \\ & + \frac{21\lambda^{4}}{640[\lambda^{2} + (Z - L_{2})^{2}]^{2}} + \frac{3\lambda^{6}}{160[\lambda^{2} + (Z - L_{2})^{2}]^{3}} + \frac{\lambda^{8}}{80[\lambda^{2} + (Z - L_{2})^{2}]^{4}} \bigg] drdx. \end{split}$$

There are two integrations that need to be determined which are

$$\begin{split} K_m &= 8\pi \int_0^{\frac{\pi}{2}} \int_b^{b+l} \frac{r}{\lambda^m (\lambda^2 + G_i^2)^n} dr dx, \\ L_m &= 8\pi \int_0^{\frac{\pi}{2}} \int_b^{b+l} \frac{r}{\lambda^m} \tan^{-1} \left(\frac{G_i}{\lambda} \right) dr dx, \quad i = 1, 2, 3, 4, \end{split}$$

where $\lambda^2 = (r-a)^2 + 4ar \sin^2 x$, m and n are the positive integers and again $G_1 = Z + L_2$, $G_2 = Z - L_2$, $G_3 = L_1 + L_2 - Z$, and $G_4 = L_1 - L_2 - Z$. We determine these integrals numerically. Thus, the interaction energy between the surface of the cylindrical drug molecule and the tube of thickness l can be given by

$$E_1^{2v} = a\eta_s\eta_v^*(-AI_3^3 + BI_6^3).$$

3.2.2. Circular ends for cylindrical drug molecule

Here, the coordinates of atoms on the circular ends are defined by $(r_1 \cos \theta_1, r_1 \sin \theta_1, Z \pm L_2)$ where $r_1 \in [0, a]$ and the coordinates of the tube are given by $(b \cos \theta_2, b \sin \theta_2, z)$. Accordingly, we have

$$\begin{split} \rho_1^{2s} &= (b\cos\theta_2 - r_1\cos\theta_1)^2 + (b\sin\theta_2 - r_1\sin\theta_1)^2 + [z - (Z + L_2)]^2 \\ &= (b - r_1)^2 + [z - (Z + L_2)]^2 + 4r_1b\sin^2\left(\frac{\theta_2 - \theta_1}{2}\right), \\ \rho_2^{2s} &= (b\cos\theta_2 - r_1\cos\theta_1)^2 + (b\sin\theta_2 - r_1\sin\theta_1)^2 + [z - (Z - L_2)]^2 \\ &= (b - r_1)^2 + [z - (Z - L_2)]^2 + 4r_1b\sin^2\left(\frac{\theta_2 - \theta_1}{2}\right). \end{split}$$

Consequently, the interaction energy between the circular areas at the two ends and the cylindrical surface of the tube is

$$E_2^{2s} = b\eta_s \eta_s^* \int_{-\pi}^{\pi} \int_{-\pi}^{\pi} \int_0^a \int_0^{L_1} r_1 \Phi(\rho_i^{2s}) dz dr_1 d\theta_1 d\theta_2, \quad i = 1, 2.$$

We define I_n^4 for this interaction energy that is defined by

$$I_n^4 = \int_{-\pi}^{\pi} \int_{-\pi}^{\pi} \int_0^a \int_0^{L_1} \frac{r_1}{(\rho_i^{2s})^n} dz dr_1 d\theta_1 d\theta_2,$$

where i = 1, 2 and n = 3, 6. With the similar techniques presented in Section 3.2.1, we finally deduce

$$\begin{split} I_3^4 &= 8\pi \int_0^{\frac{\pi}{2}} \int_0^a \frac{r_1}{\gamma_1^5} \left[\frac{3}{8} \tan^{-1} \left(\frac{L_1 - G_i}{\gamma_1} \right) + \frac{3\gamma_1 (L_1 - G_i)}{8[\gamma_1^2 + (L_1 - G_i)^2]} + \frac{\gamma_1^3 (L_1 - G_i)}{4[\gamma_1^2 + (L_1 - G_i)^2]^2} \right. \\ &\quad + \frac{3}{8} \tan^{-1} \left(\frac{G_i}{\gamma_1} \right) + \frac{3\gamma_1 G_i}{8(\gamma_1^2 + G_i^2)} + \frac{\gamma_1^3 G_i}{4(\gamma_1^2 + G_i^2)^2} \right] dr_1 dx, \end{split}$$

and

$$\begin{split} I_6^4 &= 8\pi \int_0^{\frac{\pi}{2}} \int_0^a \frac{r_1}{\gamma_1^{11}} \bigg[\frac{63}{256} \tan^{-1} \bigg(\frac{L_1 - G_i}{\gamma_1} \bigg) + \frac{63\gamma_1 (L_1 - G_i)}{256 [\gamma_1^2 + (L_1 - G_i)^2]} + \frac{21\gamma_1^3 (L_1 - G_i)}{128 [\gamma_1^2 + (L_1 - G_i)^2]^2} \\ &+ \frac{21\gamma_1^5 (L_1 - G_i)}{160 [\gamma_1^2 + (L_1 - G_i)^2]^3} + \frac{9\gamma_1^7 (L_1 - G_i)}{80 [\gamma_1^2 + (L_1 - G_i)^2]^4} + \frac{\gamma_1^9 (L_1 - G_i)}{10 [\gamma_1^2 + (L_1 - G_i)^2]^5} + \frac{63}{256} \tan^{-1} \bigg(\frac{G_i}{\gamma_1} \bigg) \\ &+ \frac{63\gamma_1 G_i}{256 (\gamma_1^2 + G_i^2)} + \frac{21\gamma_1^3 G_i}{128 (\gamma_1^2 + G_i^2)^2} + \frac{21\gamma_1^5 G_i}{160 (\gamma_1^2 + G_i^2)^3} + \frac{9\gamma_1^7 G_i}{80 (\gamma_1^2 + G_i^2)^4} + \frac{\gamma_1^9 G_i}{10 (\gamma_1^2 + G_i^2)^5} \bigg] dr_1 dx, \end{split}$$

where $\gamma_1^2 = (b - r_1)^2 + 4r_1b\sin^2 x$, $G_1 = Z + L_2$ and $G_2 = Z - L_2$. Now, we need to consider the two integrations for I_n^4 that are given by

$$F_m = 8\pi \int_0^{\frac{\pi}{2}} \int_0^a \frac{r_1}{\gamma_1^m} \tan^{-1} \left(\frac{G_i}{\gamma_1}\right) dr_1 dx,$$

$$H_m = 8\pi \int_0^{\frac{\pi}{2}} \int_0^a \frac{r_1 G_i}{\gamma_1^m (\gamma_1^2 + G_i^2)^n} dr_1 dx, \quad i = 1, 2, 3, 4.$$

These two integrals are determined numerically.

Next, we examine the interaction energy for the circular areas at two ends and a cylindrical tube with thickness *l* which is given by

$$E_2^{2v} = \eta_s \eta_v^* \int_{-\pi}^{\pi} \int_{0}^{\pi} \int_{0}^{a} \int_{b}^{b+l} \int_{0}^{L_1} r r_1 \Phi(\rho_i^{2v}) dz dr dr_1 d\theta_1 d\theta_2, \quad i = 1, 2,$$

where now

$$\rho_1^{2v} = (r - r_1)^2 + [z - (Z + L_2)]^2 + 4rr_1 \sin^2\left(\frac{\theta_2 - \theta_1}{2}\right),$$

$$\rho_2^{2v} = (r - r_1)^2 + [z - (Z - L_2)]^2 + 4rr_1 \sin^2\left(\frac{\theta_2 - \theta_1}{2}\right).$$

We also define I_n^5 for the interaction energy between the two circular ends and a tube with thickness l that is

$$I_{n}^{5} = \int_{-\pi}^{\pi} \int_{-\pi}^{\pi} \int_{0}^{a} \int_{b}^{b+l} \int_{0}^{L_{1}} \frac{rr_{1}}{(\rho_{i}^{2v})^{n}} dz dr dr_{1} d\theta_{1} d\theta_{2},$$

where again i = 1, 2 and n = 3, 6. Similarly, we employ the techniques detailed in Section 3.2.1, and obtain

$$\begin{split} I_3^5 &= 8\pi \int_0^{\frac{\pi}{2}} \int_0^a \int_b^{b+l} \frac{r r_1}{\gamma_2^5} \left[\frac{3}{8} \tan^{-1} \left(\frac{L_1 - G_i}{\gamma_2} \right) + \frac{3\gamma_2 (L_1 - G_i)}{8 [\gamma_2^2 + (L_1 - G_i)^2]} + \frac{\gamma_2^3 (L_1 - G_i)}{4 [\gamma_2^2 + (L_1 - G_i)^2]^2} \right. \\ &\quad \left. + \frac{3}{8} \tan^{-1} \left(\frac{G_i}{\gamma_2} \right) + \frac{3\gamma_2 G_i}{8 (\gamma_2^2 + G_i^2)} + \frac{\gamma_2^3 G_i}{4 (\gamma_2^2 + G_i^2)^2} \right] dr dr_1 dx, \end{split}$$

and

$$\begin{split} I_6^5 &= 8\pi \int_0^{\frac{\pi}{2}} \int_0^a \int_b^{b+l} \frac{rr_1}{\gamma_2^{11}} \bigg[\frac{63}{256} \tan^{-1} \bigg(\frac{L_1 - G_i}{\gamma_2} \bigg) + \frac{63\gamma_2 (L_1 - G_i)}{256 [\gamma_2^2 + (L_1 - G_i)^2]} + \frac{21\gamma_2^3 (L_1 - G_i)}{128 [\gamma_2^2 + (L_1 - G_i)^2]^2} \\ &+ \frac{21\gamma_2^5 (L_1 - G_i)}{160 [\gamma_2^2 + (L_1 - G_i)^2]^3} + \frac{9\gamma_2^7 (L_1 - G_i)}{80 [\gamma_2^2 + (L_1 - G_i)^2]^4} + \frac{\gamma_2^9 (L_1 - G_i)}{10 [\gamma_2^2 + (L_1 - G_i)^2]^5} + \frac{63}{256} \tan^{-1} \bigg(\frac{G_i}{\gamma_2} \bigg) \\ &+ \frac{63\gamma_2 G_i}{256 (\gamma_2^2 + G_i^2)} + \frac{21\gamma_2^3 G_i}{128 (\gamma_2^2 + G_i^2)^2} + \frac{21\gamma_2^5 G_i}{160 (\gamma_2^2 + G_i^2)^3} + \frac{9\gamma_2^7 G_i}{80 (\gamma_2^2 + G_i^2)^4} + \frac{\gamma_2^9 G_i}{10 (\gamma_2^2 + G_i^2)^5} \bigg] dr dr_1 dx, \end{split}$$

where $\gamma_2^2 = (r - r_1)^2 + 4rr_1 \sin^2 x$, $G_1 = Z + L_2$ and $G_2 = Z - L_2$. There are two types for I_n^5 which are

$$P_{m} = 8\pi \int_{0}^{\frac{\pi}{2}} \int_{0}^{a} \int_{b}^{b+l} \frac{rr_{1}}{\gamma_{2}^{m}} \tan^{-1} \left(\frac{G_{i}}{\gamma_{2}}\right) dr dr_{1} dx,$$

$$Q_{m} = 8\pi \int_{0}^{\frac{\pi}{2}} \int_{0}^{a} \int_{b}^{b+l} \frac{rr_{1}G_{i}}{\gamma_{2}^{m}(\gamma_{2}^{2} + G_{i}^{2})^{n}} dr dr_{1} dx, \quad i = 1, 2, 3, 4.$$

We note that these two integrations are also determined numerically using algebraic package MAPLE. Subsequently, the interaction energies for the circular areas at the two ends interacting with the cylindrical surface and with the cylinder of thickness *l* are obtained, respectively, as

$$E_2^{2s} = b\eta_s \eta_s^* (-AI_3^4 + BI_6^4).$$

$$E_2^{2v} = \eta_s \eta_s^* (-AI_3^5 + BI_6^5).$$

The total interaction energy arising from the surface of the tube is $E^{2s} = E_1^{2s} + E_2^{2s}$ and that arising from the volume of the tube is $E^{2v} = E_1^{2v} + E_2^{2v}$. Finally, the suction energy is examined using (3).

3.3. Ellipsoidal drug molecule

For the case of an ellipsoidal drug molecule interacting with the cylindrical surface, we define the coordinates of atoms on an ellipsoid surface centred at (0, 0, Z) as $(c_1 \sin \phi \cos \theta_1, c_1 \sin \phi \sin \theta_1, c_2 \cos \phi + Z)$. Similarly, the coordinates for the nanotube are $(b \cos \theta_2, b \sin \theta_2, z)$. Therefore, we have

$$\begin{split} \rho^2 &= (b\cos\theta_2 - c_1\sin\phi\cos\theta_1)^2 + (b\sin\theta_2 - c_1\sin\phi\sin\theta_1)^2 + [z - (c_2\cos\phi + Z)]^2 \\ &= (b - c_1\sin\phi)^2 + [z - (c_2\cos\phi + Z)]^2 + 4bc_1\sin\phi\sin^2\left(\frac{\theta_2 - \theta_1}{2}\right). \end{split}$$

A schematic model for this interaction is illustrated in Fig. 5. Hence, the interaction energy for a surface of an ellipsoidal drug molecule interacting with a surface of the tube becomes

$$E^{3s} = b\eta_s\eta_s^* \int_{S_1} \int_{S_2} \Phi(\rho) dS_2 dS_1.$$

Now, we need to determine

$$I_n^6 = \int_{-\pi}^{\pi} \int_{-\pi}^{\pi} \int_{0}^{\pi} \int_{0}^{L_1} \frac{c_1 \sin \phi \sqrt{(c_1 \cos \phi)^2 + (c_2 \sin \phi)^2}}{\rho^n} dz d\phi d\theta_1 d\theta_2,$$

where c_1 and c_2 are a minor axis and a major axis of an ellipsoid, respectively. On determining these integrals, we utilize the techniques described in Section 3.2, thus, we have

$$\begin{split} I_3^6 &= 8c_1\pi \int_0^{\frac{\pi}{2}} \int_0^{\pi} \frac{\sin\phi\sqrt{(c_1\cos\phi)^2 + (c_2\sin\phi)^2}}{\alpha^5} \Bigg[\frac{3}{8} \tan^{-1} \left(\frac{L_1 - (c_2\cos\phi + Z)}{\alpha} \right) \\ &+ \frac{3\alpha[L_1 - (c_2\cos\phi + Z)]}{8\{\alpha^2 + [L_1 - (c_2\cos\phi + Z)]^2\}} + \frac{\alpha^3[L_1 - (c_2\cos\phi + Z)]}{4\{\alpha^2 + [L_1 - (c_2\cos\phi + Z)]^2\}^2} + \frac{3}{8} \tan^{-1} \left(\frac{c_2\cos\phi + Z}{\alpha} \right) \\ &+ \frac{3\alpha(c_2\cos\phi + Z)}{8[\alpha^2 + (c_2\cos\phi + Z)^2]} + \frac{\alpha^3(c_2\cos\phi + Z)}{4[\alpha^2 + (c_2\cos\phi + Z)^2]^2} \Bigg] d\phi dx, \end{split}$$

and

$$\begin{split} I_6^6 &= 8c_1\pi \int_0^{\frac{\pi}{2}} \int_0^{\pi} \frac{\sin\phi\sqrt{(c_1\cos\phi)^2 + (c_2\sin\phi)^2}}{\alpha^{11}} \bigg[\frac{63}{256} \tan^{-1} \bigg(\frac{L_1 - (c_2\cos\phi + Z)}{\alpha} \bigg) \\ &+ \frac{63\alpha [L_1 - (c_2\cos\phi + Z)]}{256\{\alpha^2 + [L_1 - (c_2\cos\phi + Z)]^2\}} + \frac{21\alpha^3 [L_1 - (c_2\cos\phi + Z)]}{128\{\alpha^2 + [L_1 - (c_2\cos\phi + Z)]^2\}^2} \\ &+ \frac{21\alpha^5 [L_1 - (c_2\cos\phi + Z)]}{160\{\alpha^2 + [L_1 - (c_2\cos\phi + Z)]^2\}^3} + \frac{9\alpha^7 [L_1 - (c_2\cos\phi + Z)]}{80\{\alpha^2 + [L_1 - (c_2\cos\phi + Z)]^2\}^4} \\ &+ \frac{\alpha^9 [L_1 - (c_2\cos\phi + Z)]}{10\{\alpha^2 + [L_1 - (c_2\cos\phi + Z)]^2\}^5} + \frac{63}{256} \tan^{-1} \bigg(\frac{c_2\cos\phi + Z}{\alpha} \bigg) + \frac{63\alpha (c_2\cos\phi + Z)}{256[\alpha^2 + (c_2\cos\phi + Z)^2]} \\ &+ \frac{21\alpha^3 (c_2\cos\phi + Z)}{128[\alpha^2 + (c_2\cos\phi + Z)^2]^2} + \frac{21\alpha^5 (c_2\cos\phi + Z)}{160[\alpha^2 + (c_2\cos\phi + Z)^2]^3} + \frac{9\alpha^7 (c_2\cos\phi + Z)}{80[\alpha^2 + (c_2\cos\phi + Z)^2]^4} \\ &+ \frac{\alpha^9 (c_2\cos\phi + Z)}{10[\alpha^2 + (c_2\cos\phi + Z)^2]^5} \bigg] \mathrm{d}\phi \mathrm{d}x, \end{split}$$

where $\alpha^2 = (b - c_1 \sin \phi)^2 + 4bc_1 \sin \phi \sin^2 x$.

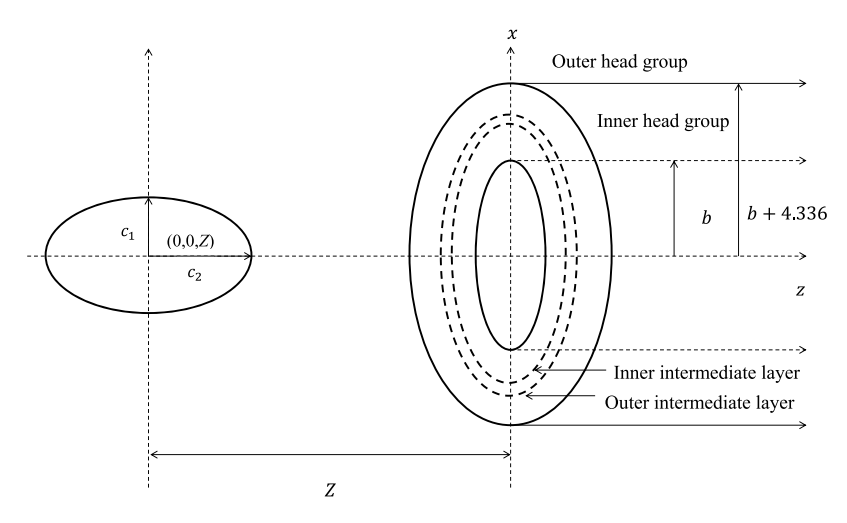


Fig. 5. Ellipsoidal drug molecule entering lipid nanotube.

Moreover, the interaction energy between a surface of an ellipsoidal drug molecule and the tube with thickness l is defined by

$$E^{3v} = \eta_s \eta_v^* \int_V \int_S \Phi(\rho) dS dV.$$

In this case, we wish to evaluate

$$I_n^7 = \int_b^{b+l} \int_{-\pi}^{\pi} \int_{-\pi}^{\pi} \int_0^{\pi} \int_0^{L_1} \frac{rc_1 \sin \phi \sqrt{(c_1 \cos \phi)^2 + (c_2 \sin \phi)^2}}{\rho^n} dz d\phi d\theta_1 d\theta_2 dr.$$

With the similar techniques presented in Section 3.2, we also have

$$\begin{split} I_3^7 &= 8c_1\pi \int_0^{\frac{\pi}{2}} \int_0^{\pi} \int_b^{b+l} \frac{r \sin \phi \sqrt{(c_1 \cos \phi)^2 + (c_2 \sin \phi)^2}}{\beta^5} \bigg[\frac{3}{8} \tan^{-1} \bigg(\frac{L_1 - (c_2 \cos \phi + Z)}{\beta} \bigg) \\ &+ \frac{3\beta [L_1 - (c_2 \cos \phi + Z)]}{8 \{\beta^2 + [L_1 - (c_2 \cos \phi + Z)]^2\}} + \frac{\beta^3 [L_1 - (c_2 \cos \phi + Z)]}{4 \{\beta^2 + [L_1 - (c_2 \cos \phi + Z)]^2\}^2} + \frac{3}{8} \tan^{-1} \bigg(\frac{c_2 \cos \phi + Z}{\beta} \bigg) \\ &+ \frac{3\beta (c_2 \cos \phi + Z)}{8 [\beta^2 + (c_2 \cos \phi + Z)^2]} + \frac{\beta^3 (c_2 \cos \phi + Z)}{4 [\beta^2 + (c_2 \cos \phi + Z)^2]^2} \bigg] dr d\phi dx, \end{split}$$

and

$$\begin{split} I_6^7 &= 8c_1\pi \int_0^{\frac{\pi}{2}} \int_0^\pi \int_b^{b+l} \frac{r \sin\phi \sqrt{(c_1\cos\phi)^2 + (c_2\sin\phi)^2}}{\beta^{11}} \Bigg[\frac{63}{256} \tan^{-1} \left(\frac{L_1 - (c_2\cos\phi + Z)}{\beta} \right) \\ &+ \frac{63\beta [L_1 - (c_2\cos\phi + Z)]}{256\{\beta^2 + [L_1 - (c_2\cos\phi + Z)]^2\}} + \frac{21\beta^3 [L_1 - (c_2\cos\phi + Z)]}{128\{\beta^2 + [L_1 - (c_2\cos\phi + Z)]^2\}^2} \\ &+ \frac{21\beta^5 [L_1 - (c_2\cos\phi + Z)]}{160\{\beta^2 + [L_1 - (c_2\cos\phi + Z)]^2\}^3} + \frac{9\beta^7 [L_1 - (c_2\cos\phi + Z)]}{80\{\beta^2 + [L_1 - (c_2\cos\phi + Z)]^2\}^4} \\ &+ \frac{\beta^9 [L_1 - (c_2\cos\phi + Z)]}{10\{\beta^2 + [L_1 - (c_2\cos\phi + Z)]^2\}^5} + \frac{63}{256} \tan^{-1} \left(\frac{c_2\cos\phi + Z}{\beta} \right) \\ &+ \frac{63\beta (c_2\cos\phi + Z)}{256[\beta^2 + (c_2\cos\phi + Z)^2]} + \frac{21\beta^3 (c_2\cos\phi + Z)}{128[\beta^2 + (c_2\cos\phi + Z)^2]^2} + \frac{21\beta^5 (c_2\cos\phi + Z)}{160[\beta^2 + (c_2\cos\phi + Z)^2]^3} \\ &+ \frac{9\beta^7 (c_2\cos\phi + Z)}{80[\beta^2 + (c_2\cos\phi + Z)^2]^4} + \frac{\beta^9 (c_2\cos\phi + Z)}{10[\beta^2 + (c_2\cos\phi + Z)^2]^5} \Bigg] \mathrm{d}r\mathrm{d}\phi\mathrm{d}x, \end{split}$$

where $\beta^2 = (r - c_1 \sin \phi)^2 + 4c_1 r \sin \phi \sin^2 x$. Due to the complicated formulae, the algebraic package MAPLE is utilized to determine the total interaction energies which are given by

$$E^{3s} = b\eta_s\eta_s^*(-AI_3^6 + BI_6^6),$$

$$E^{3v} = \eta_s \eta_s^* (-AI_2^7 + BI_6^7),$$

and also the suction energy defined by (3) can be obtained by taking a limit of the energy from $Z=-\infty$ to $Z=\infty$.

Table 3 Values of b_0 , b_{max} , and S_{max} for all cases studied here.

Shapes	b ₀ (nm)	b _{max} (nm)	S _{max} (kJ/mol)
	a = 12 nm		
Sphere $(r = a)$	12.2487	12.3069	1.2896×10^{-2}
Cylinder $(r = a/2)$	6.2765	6.3343	6.2849×10^{-2}
Cylinder $(r = a)$	12.2768	12.3357	3.6046×10^{-2}
Cylinder ($r = 0.7321a$)	9.0615	9.1143	5.2086×10^{-2}
Cylinder ($r = 0.4494a$)	5.6701	5.7289	6.4818×10^{-2}
Ellipsoid ($c_1 = 0.9441a$ and $c_2 = 1.114a$)	11.5776	11.6354	1.3930×10^{-2}
	a = 30 nm		
Sphere $(r = a)$	30.2484	30.3069	5.0334×10^{-2}
Cylinder $(r = a/2)$	15.2775	15.3343	3.7935×10^{-1}
Cylinder $(r = a)$	30.2786	30.3357	2.1708×10^{-1}
Cylinder $(r = 0.7321a)$	22.2384	22.2986	3.1651×10^{-1}
Cylinder $(r = 0.4494a)$	13.7615	13.8208	3.9033×10^{-1}
Ellipsoid ($c_1 = 0.9441a$ and $c_2 = 1.114a$)	28.5713	28.6306	5.4431×10^{-2}

4. Numerical results and discussion

We assume the length of the lipid nanotube to be $L_1 = 200$ nm, and fix the surface areas of the three shapes of DOX cluster to be equal. The surface areas for the three shapes of the drug molecule can be evaluated using the formulae

- 1. Spherical area = $4\pi a^2$,
- 2. Cylindrical area (including two circular ends) = $2\pi a(2L_2) + 2\pi a^2$, 3. Ellipsoidal area = $2\pi c_1^2 \left(1 + \frac{c_2 \sin^{-1} \sqrt{1 c_1^2/c_2^2}}{c_1 \sqrt{1 c_1^2/c_2^2}}\right)$.

We consider a sphere of radius a while a cylindrical structure is determined in four cases; that are, radii a/2, a, 0.7321a, and 0.4494a corresponding to the length L_2 of 7a/4, a/2, a, and 2a, respectively. Moreover, a minor and a major axes of an ellipsoidal drug molecule are taken to be 0.9441a and 1.114a, respectively, giving rise to the equal surface area of the sphere and representing an ellipsoidal structure. We employ the algebraic package MAPLE to numerically calculate the suction energy. Here, we assume two values for a which are 12 and 30 nm to represent a small and a large cluster of DOX. As illustrated in Fig. 6 for the case of a=12 nm, we can predict the radius of the lipid nanotube that can encapsulate each shape of the DOX, and the numerical values are presented in Table 3. We note that for a = 12 nm, the surface areas of all shapes are 1809 nm². The minimum value of the inner most radius of the lipid nanotube that accepts the drug is denoted by b_0 , and that gives the maximum suction energy is denoted by b_{max} . We comment that the volume integral for the solid structures of DOXs can be determined by including another integral dimension. For the case of spherical solid DOX with a=12 nm, we obtain $b_0=12.1902$ nm and $b_{\rm max}=12.2504$ nm which are comparable with the hollow spherical shape.

From the maximum suction energy shown in Table 3, we observe that the best structure of the drug molecule is a cylinder with $L_2 = 2a$. It offers the suction energy of 6.4818×10^{-2} kJ/mol that is greater than other cases in our study. This is because the best fit configuration where the surfaces of the lipid nanotube and the drug molecule interact perfectly.

Further, we determine the suction behaviour for a = 30 nm that is larger than the tail length l, and it is depicted in Fig. 7. In this case, all the surface areas of DOX drug molecule are fixed to be 11,309 nm². The numerical results are also reported in Table 3, and we find that a cylinder of the length $L_2 = 2a$ is also an appropriate shape with the maximum suction energy 3.9033×10^{-1} kJ/mol. The long cylinder maximizes the suction energy, therefore, it may be a good candidate among other possible structures of the drug molecules studied here to interact with the lipid nanotube. We comment that both small and large drug molecules present a similar suction behaviour. On defining $\delta=b_{\max}-r$ which is the interspacing between the surface of the drug and the inner most radius of the tube giving rise to the maximum suction energy, for the three shapes and for both sizes, we have $\delta \approx 0.3$ nm.

Furthermore, an appropriate shape of the drug is also related to the size of the lipid nanotube. For example, when the lipid nanotube is small, we can employ a thin cylinder since it requires a small tube radius. In addition, if there is a large size of the lipid nanotube, then either a cylindrical structure of radius a or a spherical molecule may be used to obtain a more stable system, see Figs. 6 and 7.

5. Summary

The work presented in this paper focuses on the interaction energy between the three hollow shapes of DOX cluster and the lipid nanotube. Those three shapes consist of a sphere, a cylinder, and an ellipsoid. We derive the mathematical expression, and use the Lennard-Jones potential function and the continuous approximation to examine the energy behaviour for each system of DOX entering the lipid nanotube. Further, the suction energy is determined where we find that a thin cylindrical DOX molecule gives a maximum suction energy among other cases. Finally, we can predict the minimum

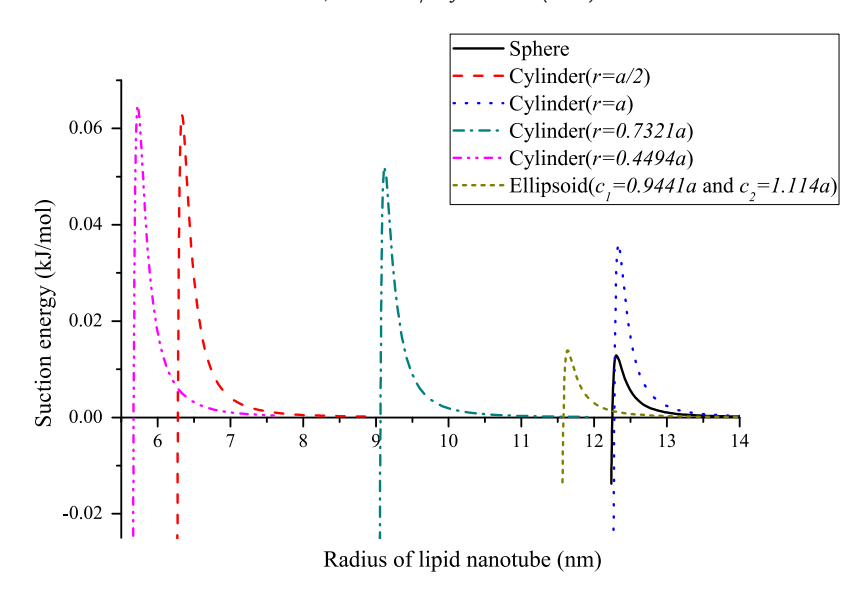


Fig. 6. Suction energy for DOX entering lipid nanotube where a = 12 nm.

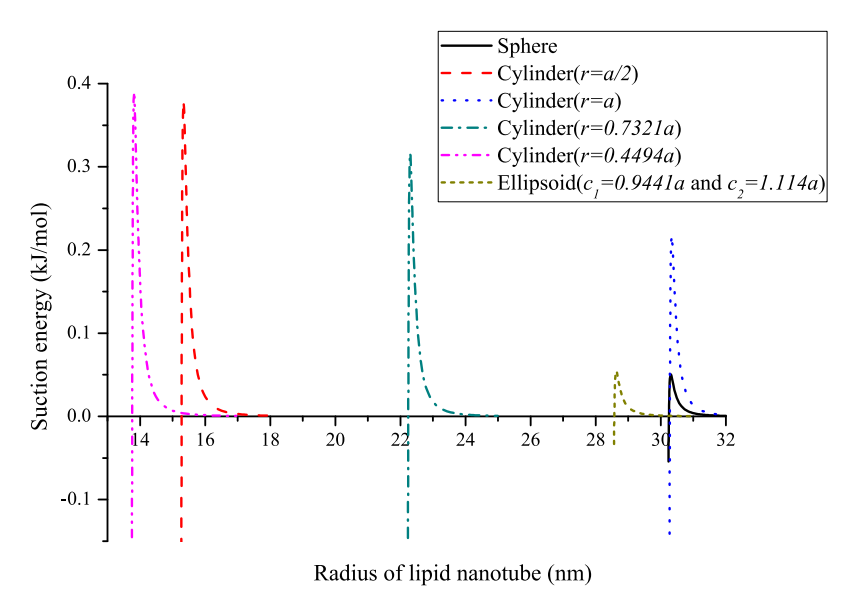


Fig. 7. Suction energy for DOX entering lipid nanotube where a = 30 nm.

size of the tube that accepts the drug inside, consider an appropriate shape of the drug molecule that can be encapsulated by the lipid nanotube, and determine the optimal size of the tube for each shape of DOX. We also obtain that the value of b_0-r is approximate 0.2 nm, and $b_{\rm max}-r$ is around 0.3 nm for all cases. All in all, our study is a basic knowledge to understand the encapsulation behaviour that may play an important role in application of drug and gene delivery.

Acknowledgements

Financial support from the Development and Promotion of Science and Technology Talented Project (DPST) is acknowledged. DB is also grateful for the support of the Thailand Research Fund (RSA5880003). The authors gratefully thank Mr. Kanes Sumetpipat for many helpful discussions.

References

- [1] D.M. Parkin, F. Bray, J. Ferlay, P. Pisani, Global cancer statistics, 2002, CA Cancer J. Clin. 55 (2005) 74–108.
- [2] A. Jema, F. Bray, M.M. Center, J. Ferlay, E. Ward, D. Forman, Global cancer statistics, CA Cancer J. Clin. 61 (2011) 69–90.
- [3] S.S. Suri, H. Fenniri, B. Singh, Nanotechnology-based drug delivery systems, J. Occup. Med. Toxicol. 2 (2007) 16.

- [4] H. Meng, M. Liong, T. Xia, Z. Li, Z. Ji, J.I. Zink, A.E. Nel, Engineered design of mesoporous silica nanoparticles to delivery doxorubicin and P-glycoprotein siRNA to overcome drug resistance in a cancer cell line, Am. Chem. Soc. Publ. 4 (2010) 4539–4550.
- [5] Y.J. Lu, K.C. Wei, C.C.M. Ma, S.Y. Yang, J.P. Chen, Dual targeted delivery of doxorubicin to cancer cells using folate-conjugated magnetic multi-walled carbon nanotubes, Colloids Surf. B 89 (2012) 1–9.
- [6] L. Meng, X. Zhang, Q. Lu, Z. Fei, P.J. Dyson, Single walled carbon nanotubes as drug delivery vehicles: Targeting doxorubicin to tumors, Biomaterials 33 (2012) 1689–1698.
- [7] Y. Zhou, T. Shimizu, Lipid nanotube: A unique template to create diverse one-dimensional nanostructures, Chem. Mater. 20 (2008) 625–633.
- [8] T. Shimizu, Self-assembled lipid nanotube hosts: The dimension control for encapsulation of nanometer-scale guest substances, J. Polym. Sci. A 44 (2006) 5137–5152.
- [9] Q. Ji, S. Kamiya, J.H. Jung, T. Shimizu, Self-assembly of glycolipid on silica nanotube templates yielding hybrid nanotubes with concentric organic and inorganic layers, J. Mater. Chem. 15 (2005) 743–748.
- [10] A.M. Seddon, H.M. Patel, S.L. Burkett, S. Mann, Chiral templating of silica-lipid lamellar mesophase with helical tubular architecture, Angew. Chem. Int. Ed. 41 (2002) 2988–2991.
- [11] E. Leo, R. Cameroni, F. Forni, Dynamic dialysis for the drug release evaluation from doxorubicin-gelatin nanoparticle conjugates, Int. J. Pharm. 180 (1999) 23–30.
- [12] Z. Liu, X. Sun, N. Nakayama-Ratchford, H. Dai, Supramolecular chemistry on water-soluble carbon nanotubes for drug loading and delivery, ACS Nano 1 (2007) 50–56.
- [13] W. Dali, S. Yue, J. Chengyu, Z. Bangshang, P. Yan, Z. Lijuan, L. Jinyao, T. Chunlai, Y. Deyue, Z. Xinyuan, Supramolecular copolymer micelles based on the complementary multiple hydrogen bonds of nucleobases for drug delivery, J. Am. Chem. Soc. 12 (2011) 1370–1379.
- [14] D. Baowan, B.J. Cox, J.M. Hill, Instability of C₆₀ fullerene interacting with lipid bilayer, J. Mol. Model. 18 (2012) 549-557.
- [15] D. Baowan, N. Thamwattana, Modelling encapsulation of gold and silver nanoparticles inside lipid nanotubes, Physica A 396 (2014) 149-154.
- [16] B.J. Cox, N. Thamwattana, J.M. Hill, Mechanics of spheroidal fullerenes and carbon nanotubes for drug and gene delivery, Quart. J. Mech. Appl. Math. 60 (2007) 231–253.
- [17] B.J. Cox, N. Thamwattana, J.M. Hill, Spherical and spheroidal fullerenes entering carbon nanotubes, Curr. Appl. Phys. 8 (2008) 249–252.
- [18] B.J. Cox, N. Thamwattana, J.M. Hill, Mechanics of atoms and fullerenes in single-walled carbon nanotubes. I. Acceptance and suction energies, Proc. R. Soc. A 463 (2007) 461–477.
- [19] Y. Li, L. Yang, Diving forces for drug loading in drug carriers, J. Microencapsul. 32 (2015) 255-272.
- [20] L. Poudel, A.M. Wen, R.H. French, V.A. Parsegian, R. Podgornik, N.F. Steinmetz, C. Wai-Yim, Electronic structure and partial charge distribution of Doxorubicin in different molecular environments, Chem. Phys. Chem. 16 (2015) 1451–1460.
- [21] D. Baowan, H. Peuschel, A. Kraegeloh, V. Helms, Energetics of liposomes encapsulating silica nanoparticles, J. Mol. Model. 19 (2013) 2459-2472.
- [22] S.J. Marrink, H.J. Risselada, S. Yefimov, D.P. Tieleman, A.H. de Vries, The martini force field: Coarse grained model for biomolecular simulations, J. Phys. Chem. B 111 (2007) 7812–7824.
- [23] K. Sumetpipat, D. Baowan, Three model shapes of doxorubicin for liposome encapsulation, J. Mol. Model. 20 (2014) 2504.
- [24] I.S. Gradshteyn, I.M. Ryzhik, Table of Integrals, Series, and Products, seventh ed., Academic Press, 2007.

FISEVIER

Contents lists available at ScienceDirect

Chemical Physics Letters

journal homepage: www.elsevier.com/locate/cplett



Research paper

Continuous approximation for interaction energy of adamantane encapsulated inside carbon nanotubes



Duangkamon Baowan a,b,*, James M. Hill c, Wolfgang Bacsa d

- ^a Department of Mathematics, Faculty of Science, Mahidol University, Rama VI Rd., Bangkok 10400, Thailand
- ^b Centre of Excellence in Mathematics, CHE, Bangkok 10400, Thailand
- c School of Information Technology & Mathematical Sciences, University of South Australia, Mawson Lakes, SA, Australia
- ^d CEMES-CNRS and University of Toulouse, 29 rue Jeanne Marvig, 31055 Toulouse, France

ARTICLE INFO

Article history:
Received 6 October 2017
In final form 21 December 2017
Available online 22 December 2017

Keywords: Adamantane Carbon nanotube Lennard-Jones potential Interaction energy

ABSTRACT

The interaction energy for two adjacent adamantane molecules and that of adamantane molecules encapsulated inside carbon nanotubes are investigated considering only dipole-dipole induced interaction. The Lennard-Jones potential and the continuous approximation are utilised to derive analytical expressions for these interaction energies. The equilibrium distance 3.281 Å between two adamantane molecules is determined. The smallest carbon nanotube radius b_0 that can encapsulate the adamantane molecule and the radius of the tube b_{max} that gives the maximum suction energy, linearly depend on the adamantane radius, are calculated. For larger diameter tubes, the off axis position has been calculated, and equilibrium distance between molecule and tube wall is found to be close to the interlayer spacing in graphene.

© 2018 Elsevier B.V. All rights reserved.

1. Introduction

Conceivably, linear forms of crystalline diamond constitute a new one-dimensional nanomaterial. They are believed to assemble within carbon nanotubes which serve as a template and by taking diamondoids as building blocks. Template synthesis of linear chain nanodiamonds have been considered recently using diamantine polymers [1]. The smallest building block of diamond is adamantane, which is the smallest unit with a diamond lattice. We examine here the interaction energy of adamantane in canbon nanotubes assuming the Lennard-Jones potential and the continuous approximation. Analytical expressions are derived using a highly simplified model, and the derived structural parameters are close to density functional calculations [2].

Adamantane ($C_{10}H_{16}$) is the smallest diamondoid with sp³ hybridization and hydrogen on its surface [3–5]. It consists of four connected cyclohexane rings, in armchair configuration, and in three dimensions arranges to form a cage, with bond angles the same as those found in diamond. While hydrocarbons with only σ -bonds are relatively chemically inert, adamantane is highly reactive. The four 3-coordinated carbon atoms are particularly reactive

E-mail address: duangkamon.bao@mahidol.ac.th (D. Baowan).

while the remaining six 2-coordinated carbon atoms are less reactive. Adamantanes and its derivatives are also used in medical applications, for example; to treat flu [6], avian influenza virus [7,8] and to act as an antiviral agent against HIV [9,10] or as a lubricant stable at elevated temperatures.

In this study, we aim to determine the interaction energy between two adamantane moleclues and that of an adamantane molecule interacting with a carbon nanotube taking only dipole-dipole interaction into account. The equilibrium position of two adamantanes and the encapsulation behaviour of an adamantane molecule are determined. The continuum approach utilised here might also be useful when applied to future one-dimensional nanomaterials or relevant biomedical systems.

In terms of energy calculations, McIntosh et al. [11] use density functional theory and propose that the encapsulation of adamantane molecules inside carbon nanotubes occurs spontaneously. Moreover, they suggest that the (7,7) carbon nanotube (r=4.75 Å) has the ideal radius to contain a single adamantane molecule with optimal suction energy, and the peapod structure [12–14] of the adamantane molecules is found when the radius of the tube is increased. Linear assemblies of adamantanes inside double-wall carbon nanotubes have been studied by Zhang et al. [2] who suggest that the equilibrium distance between two adamantane molecules is approximately 6.2 Å. Shi et al. [15] report a method for the bulk production of long linear carbon chains in double-walled carbon nanotubes. Further, they find that the equilibrium spacing in

^{*} Corresponding author at: Department of Mathematics, Faculty of Science, Mahidol University, Rama VI Rd., Bangkok 10400, Thailand.

the carbon chain that is encapsulated in a carbon nanotube is $3.378\,\text{Å}.$

In this paper, we employ applied mathematical modelling to derive analytical expressions for the energy of the system involving adamantane molecules and a carbon nanotube. The Lennard-Jones potential for the non-bonded atoms is assumed to approximate the van der Waals interactions, since it has been confirmed that the dipole-dipole interactions play an important role in systems of adamantanes and carbon nanotubes [2,11,15]. Furthermore, we assume that the continuous approximation, where atoms on the surface of the molecule are assumed to be uniformly distributed over the molecule, can be used to evaluate the total energy of the system. The continuous or continuum approach has been successfully used to determine the energy behavior of several nanoscaled systems and, in particular, it has been adopted to determine C_{60} fullerene patterns inside carbon nanotubes, referred as nanopeapods [14] or nobel gases encapsulated in carbon nanotubes [16].

The Lennard-Jones potential function and the continuous approach are presented in the following section and mathematical derivations for spherical and cylindrical shapes are given in Section 3. The results of our findings are presented in Section 4 and finally, a brief summary is given in Section 5.

2. Lennard-Jones potential and continuous approximation

We employ the Lennard-Jones potential and continuous approximation to determine the molecular interatomic energy between two molecules. We assume the 6–12 Lennard-Jones potential given by

$$\Phi = -\frac{A}{\rho^6} + \frac{B}{\rho^{12}},$$

where ρ denotes the distance between two atoms, $A=4\epsilon\sigma^6$ and $B=4\epsilon\sigma^{12}$ are respectively the attractive and repulsive constants, and where ϵ is the energy well depth and σ is the inter-atomic distance when the potential is zero. The minimum of the potential well is located at distance $\rho_0=(2B/A)^{1/6}=2^{1/6}\sigma$. Using a continuum approach, atoms at discrete locations on the molecule are assumed to be averaged over its surface, which means that summations over all atoms involved is replaced by surface integrals. The molecular interatomic energy is then obtained by calculating integrals over the surface of each molecule, given by

$$E = \eta_1 \eta_2 \int_{S_1} \int_{S_2} \left(-\frac{A}{\rho^6} + \frac{B}{\rho^{12}} \right) dS_2 dS_1, \tag{1}$$

where η_1 and η_2 represent the mean surface density of atoms on each molecule. Further, by writing

$$I_n = \int_{S_1} \int_{S_2} \rho^{-2n} dS_2 dS_1, \quad (n = 3, 6), \tag{2}$$

Eq. (1) can then be written as

$$E = \eta_1 \eta_2 (-AI_3 + BI_6). \tag{3}$$

To determine the radius of the tube which will maximise the suction energy, we utilize the suction energy concept as proposed in [17]. The suction energy W is defined as the total energy or work gained by the van der Waals interactions acquired by a particular molecule to enter the tube,

$$W = \int_{-\infty}^{\infty} F(Z)dZ = \int_{-\infty}^{\infty} -\frac{\partial E}{\partial Z}dZ, \tag{4}$$

where E is as given in (3) and Z is a distance between two molecules. Note that due to the symmetry of the systems studied here we only need to consider axial forces.

The numerical values of the Lennard-Jones parameters used for nonbonded adamantane sp³ hybridization and carbon nanotube sp² hybridiztion are taken from the work of Rappé et al. [18] where $\epsilon = 0.105$ kcal/mol and $\sigma = 3.851$ Å for both hybridizations. The mean atomic surface density of the carbon nanotube is taken to be 0.3812 Å⁻² [19], and the adamantane molecule (C₁₀H₁₆) is modelled as a sphere. For any given radius a of an adamantane, the mean atomic surface density of carbon atoms on the surface of an adamantane is given by $10/(4\pi a^2)$ Å⁻².

We note that since the energy well depth of hydrogen is approximately six times less that of carbon, only the carbon atoms are considered and the effect of the hydrogen is ignored. We note that there are two categories of carbon atoms on the adamantane molecule connecting to hydrogen atoms; one category are those which are bonded to only one hydrogen atom, while the other category are those bonded to two hydrogen atoms. Further, the locations of hydrogen are not well defined, since the spherical adamantane molecule has a large curvature. Moreover, hydrogen has already been incorporated in the Lennard-Jones parameter values for sp³ hybridization.

3. Interaction energy

Here we investigate the energy behaviour of an adamantane molecule inside a single-walled carbon nanotube. Firstly, we determine the equilibrium distance between two adamantane molecules assuming they form a linear array. Secondly, the encapsulation behaviour of an adamantane molecule in a carbon nanotube is studied to determine the tube radius that can encapsulate the molecule.

As mentioned in Section 2, the Lennard-Jones potential is used to determine the interaction energy between two non-bonded atoms. The atoms are uniformly distributed on the surface of the molecule or nanotube and hence an integral expression is utilised using uniform atom densities to determine the total interaction energy between two molecules.

We start by considering a spherical adamantane molecule, consisting of carbon atoms, interacting with a single atom, as described in the following subsection. Subsequently, we assume that the single atom is located either on another spherical adamandane molecule or on the surface of a cylindrical carbon nanotube, and the interaction between two spheres and the interaction between a sphere and a cylinder are determined as described in Sections 3.2 and 3.3, respectively.

Noting that the encapsulation of nano-scaled materials is also dependent on the temperature, other environmental effects and impurities or adsorbed species. The mathematical modelling presented here is an idealised approach which provides reasonably accurate estimates for stable configurations of pristine systems.

3.1. Interaction between sphere and single atom

Here, we determine the interaction energy between a spherical surface and a single atom, a configuration shown in Fig. 1. In the Cartesian coordinate system with origin at the centre of the sphere, the single atom is assumed to be located at $(0,0,\delta)$, so that the integral I_n defined in (2) becomes

$$I_{n}=\int_{-\pi}^{\pi}\int_{0}^{\pi}\frac{a^{2}\sin\phi}{\left(a^{2}+\delta^{2}-2a\delta\cos\phi\right)^{n}}d\phi d\theta,$$

where $\rho^2 = a^2 + \delta^2 - 2a\delta\cos\phi$ and δ is the distance from the single atom to the centre of the sphere. By making the substitution $t = a^2 + \delta^2 - 2a\delta\cos\phi$ and using the fact that I_n is independent of θ , we may deduce

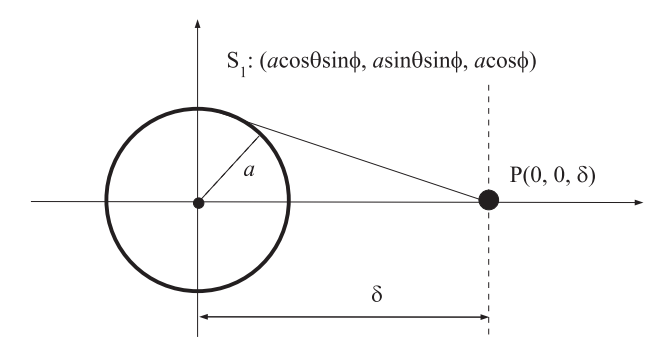


Fig. 1. Geometry for interaction between sphere and atom.

$$I_{n} = \frac{a\pi}{\delta} \int_{(\delta-a)^{2}}^{(\delta+a)^{2}} \frac{1}{t^{n}} dt = \frac{a\pi}{\delta(n-1)} \left[\frac{1}{(\delta+a)^{2(n-1)}} - \frac{1}{(\delta-a)^{2(n-1)}} \right], \quad (5)$$

and in particular,

$$\begin{split} I_{3} &= \frac{a\pi}{2\delta} \left[\frac{1}{\left(\delta + a\right)^{4}} - \frac{1}{\left(\delta - a\right)^{4}} \right] = 4\pi a^{2} \left[\frac{1}{\left(\delta^{2} - a^{2}\right)^{3}} + \frac{2a^{2}}{\left(\delta^{2} - a^{2}\right)^{4}} \right], \tag{6} \\ I_{6} &= \frac{a\pi}{5\delta} \left[\frac{1}{\left(\delta + a\right)^{10}} - \frac{1}{\left(\delta - a\right)^{10}} \right] \\ &= \frac{4\pi a^{2}}{5} \left[\frac{5}{\left(\delta^{2} - a^{2}\right)^{6}} + \frac{80a^{2}}{\left(\delta^{2} - a^{2}\right)^{7}} + \frac{336a^{4}}{\left(\delta^{2} - a^{2}\right)^{9}} + \frac{256a^{8}}{\left(\delta^{2} - a^{2}\right)^{10}} \right]. \end{aligned}$$

Thus, the total interaction energy between a spherical molecule and a single atom is given by

$$E_{sp} = \frac{\eta_1 a \pi}{\delta} \left\{ -\frac{A}{2} \left[\frac{1}{(\delta + a)^4} - \frac{1}{(\delta - a)^4} \right] + \frac{B}{5} \left[\frac{1}{(\delta + a)^{10}} - \frac{1}{(\delta - a)^{10}} \right] \right\},$$
(8)

where η_1 is the mean atomic surface density of the adamantane molecule.

3.2. Interaction between two spherical molecules

Here, we aim to determine the interaction energy between two spherical adamantane molecules by evaluating two spherical surface integrals. The schematic of this problem is presented in Fig. 2. The distance from the centre of one sphere centred at the origin to an arbitrary point of the other sphere centred at the (0,0,Z) is given by $\delta^2 = a_2^2 + Z^2 - 2a_2Z\cos\phi$ where Z is the distance between their centres. From the integral I_n defined by (5), the other surface evaluation becomes

$$I'_{n} = \frac{a_{1}\pi}{(n-1)} \int_{-\pi}^{\pi} \int_{0}^{\pi} \frac{a_{2}^{2} \sin \phi}{\delta} \left[\frac{1}{(\delta - a_{1})^{2(n-1)}} - \frac{1}{(\delta + a_{1})^{2(n-1)}} \right] d\phi d\theta,$$

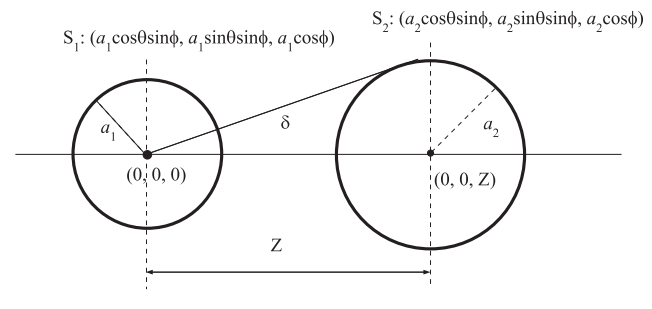


Fig. 2. Geometry for interaction between two spheres.

where a_2 denotes the radius of the sphere S_2 . As there is no dependence on θ in the integrand, this can be done immediately and we make the substitution of variable of δ for ϕ , which yields

$$\begin{split} I_n' &= \frac{2\pi^2 a_1 a_2}{Z(n-1)} \int_{Z-a_2}^{Z+a_2} \left[\frac{1}{(\delta-a_1)^{2(n-1)}} - \frac{1}{(\delta+a_1)^{2(n-1)}} \right] d\delta \\ &= \frac{2\pi^2 a_1 a_2}{Z(n-1)(2n-3)} \left[\frac{1}{(Z-a_1-a_2)^{2n-3}} - \frac{1}{(Z+a_1-a_2)^{2n-3}} \right. \\ &- \frac{1}{(Z-a_1+a_2)^{2n-3}} + \frac{1}{(Z+a_1+a_2)^{2n-3}} \right]. \end{split} \tag{9}$$

Thus, the total van der Waals interaction energy between two spheres becomes

$$E_{ss} = \eta_1 \eta_2 (-AI_3' + BI_6'), \tag{10}$$

where I_n' is defined by (9), and η_1 and η_2 are the mean surface densities for the two spheres.

3.3. Interaction between sphere and cylinder

In order to determine the molecular interaction energy between a spherical adamantane molecule and a cylindrical carbon nanotube, we need to perform another surface integral of (6) and (7) which are given respectively by

$$I_3'' = 4\pi a^2 \int_{S} \left[\frac{1}{(\delta^2 - a^2)^3} + \frac{2a^2}{(\delta^2 - a^2)^4} \right] dS, \tag{11}$$

$$I_{6}'' = \frac{4\pi a^{2}}{5} \int_{S} \left[\frac{5}{(\delta^{2} - a^{2})^{6}} + \frac{80a^{2}}{(\delta^{2} - a^{2})^{7}} + \frac{336a^{4}}{(\delta^{2} - a^{2})^{8}} + \frac{512a^{6}}{(\delta^{2} - a^{2})^{9}} + \frac{256a^{8}}{(\delta^{2} - a^{2})^{10}} \right] dS.$$

$$(12)$$

For convenience, we define the integrals J_n given by

$$J_n = \int_S \frac{1}{\left(\delta^2 - a^2\right)^n} dS,\tag{13}$$

where n is a positive integer corresponding to the power of polynomials appearing in the above equations for I_3^n and I_6^n .

Assuming that all the carbon atoms are distributed over its surface, a surface integral technique can be employed to determine the interaction energy between a spherical adamantane molecule and a cylindrical tube, and the schematic representation of this system is shown in Fig. 3.

In Cartesian coordinates, the tube is assumed to have length L with radius b, and its open end is assumed to be located at the origin. Further, the sphere is assumed to be centred at $(\varepsilon,0,Z)$ where Z is the distance between the tube open end to the centre of the sphere, and ε is the off-set distance from the tube axis. Positive and negative values of Z indicate that the sphere is inside and outside the tube, respectively. The distance from the centre of the sphere to a typical point of the tube is given by

$$\delta^{2} = (b\cos\theta - \varepsilon)^{2} + (b\sin\theta)^{2} + (z - Z)^{2},$$

= $(b - \varepsilon)^{2} + 4\varepsilon b\sin^{2}(\theta/2) + (z - Z)^{2}.$

so that the cylindrical surface integral of J_n defined by (13) becomes

$$J_{n} = \int_{-\pi}^{\pi} \int_{0}^{L} \frac{b}{\left[\left(b-\varepsilon\right)^{2} + 4\varepsilon b \sin^{2}(\theta/2) + \left(z-Z\right)^{2} - a^{2}\right]^{n}} dz d\theta.$$

We let $\lambda^2 = (b - \varepsilon)^2 + 4\varepsilon b \sin^2(\theta/2) - a^2$, and we introduce $z - Z = \lambda \tan \psi$ to obtain

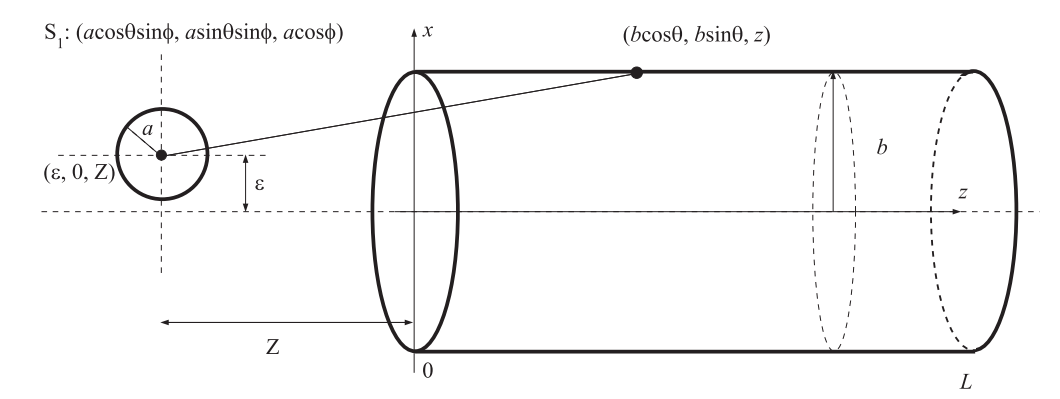


Fig. 3. Geometry for interaction between sphere and cylindrical tube.

$$J_n = b \int_{-\pi}^{\pi} \frac{1}{\lambda^{2n-1}} \int_{-\tan^{-1}(Z/\lambda)}^{\tan^{-1}[(L-Z)/\lambda]} \cos^{2n-2} \psi d\psi d\theta.$$

From Gradshteyn and Ryzhik (formula 2.513.3) [20], the above integral with ψ can be determined for any given n, namely

$$\int \cos^{2n} x dx = \frac{1}{2^{2n}} \left[\binom{2n}{n} x + \sum_{k=0}^{n-1} \binom{2n}{k} \frac{\sin[(2n-2k)x]}{n-k} \right],$$

and we have

$$J_{n} = \frac{b}{2^{2(n-1)}} \times \int_{-\pi}^{\pi} \frac{1}{\lambda^{2n-1}} \left[\binom{2n-2}{n-1} \psi + \sum_{k=0}^{n-2} \binom{2n-2}{k} \frac{\sin[(2n-2-2k)\psi]}{n-1-k} \right]_{\psi=-\tan^{-1}(\mathbb{Z}/\lambda)}^{\tan^{-1}((L-\mathbb{Z})/\lambda)} d\theta.$$
 (14)

For any given integer n, the above integration is numerically evaluated using the mathematical package MAPLE. We then substitute J_n as defined by (14) into I_3'' and I_6'' defined by (11) and (12), respectively, and finally the interaction energy between a spherical adamantane molecule and a cylindrical carbon nanotube is given by

$$E_{sc} = \eta_1 \eta_3 (-AI_3'' + BI_6''), \tag{15}$$

where η_3 represents the mean atomic surface density of the carbon nanotube which is 0.3812 Å⁻².

4. Numerical results

We consider first the interaction energy between two adamantane molecules. Fig. 4 traces the energy as a function of inter molecular distance by evaluating the analytic expression for the interaction energy as outlined in Section 3.2 and assuming the molecular radius to be of 1.773 Å. This is the average geometric distance of the ten atoms from the center of an adamantane molecule. As a result the closest distance Z or spacing between surfaces ξ of the two adamantane molecules can be determined noting that $Z_0 = \xi + 2a$. A schematic of the two molecules appears as an insert in Fig. 4(a). We find that the equilibrium distance between the two spheres Z_0 is 6.863 Å and the spacing ξ is 3.317 Å. This finding is within 10% of Zhang et al. [2] who report an equilibrium distance of 6.2 Å when using ab inito calculations using density functional theory. The binding energy is 0.076 eV whereas that obtained by Zhang et al. [2] is 0.16 eV. The 52% difference is due to the fact that we take only dipole induced forces into account.

To obtain the same spacing between the adamantine molecules $(Z_0=6.2~\text{Å})$ with our analytic approach one would need to reduce the molecular radius by 20% to 1.427 Å. Since the exact radius a of the sphere which represents adamantane molecule, is not known, we can calculate Z_0 or ξ as a function of radius. Fig. 4(b) shows the relation between ξ and a, and we find that the value of ξ decreases to 3.285 Å when the radius a becomes larger. A larger sphere reduces the effect of curvature, increases the interaction and reduces the intermolecular distance.

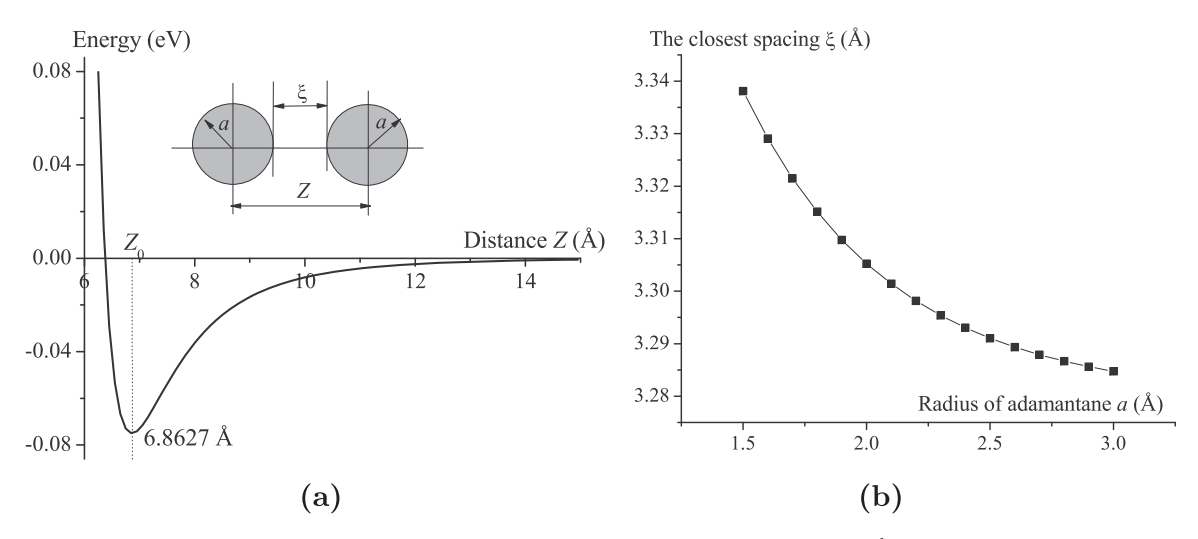


Fig. 4. (a) Potential profile for interaction energy between two spherical adamantane molecules of radius a = 1.773 Å and (b) closest distance ξ between two spherical adamantane molecules at minimum energy location Z_0 .

We incorporate the effect of hydrogen in our model by taking the upper limit of the carbon-hydrogen bond length, which tends to increase the equilibrium distance by approximately 2.200 Å.

The suction energy, the gain of energy through encapsulation per molecule and as a function of tube radius, has been traced in Fig. 5(a) after evaluating the expression of the suction energy derived in Section 3.3 and Eq. (4) for a molecular radius a = 1.773 Å. Here we suppose that the adamantane molecule is located on the tube axis so that $\varepsilon = 0$, and we find that the minimum radius of the tube b_0 that can draw the molecule inside is 4.847 Å which is close to the diameter of a (7,7) tube. Further we see that the maximum suction energy will occur when the nanotube has a radius of about $b_{max} = 5.426$ Å corresponding to an armchair (8,8) tube which has a radius of 5.424 Å.

As mentioned by McIntosh et al. [11] and Zhang et al. [2], the smallest carbon nanotube according to DFT calculations that can encapsulate a molecule of adamantane is a (7,7) tube having a radius of 4.747 Å which is only 2% off when taking only van der Waals interaction into account and using the continuum approach.

The adamantane radius which fits with the DFT calculations of the minimum tube radius (4.747 Å) is 6.3% smaller (1.668 Å). We observe that the tube radii b_0 and b_{max} are both linearly dependent

on the adamantane radius a as shown in Fig. 5(b). Fig. 5(b) also shows the difference between the tube and molecular radius denoted as c_{b_0} and $c_{b_{max}}$, are constant when changing the molecular radius. That means that the adamantane will enter the carbon nanotube when the radius of the tube is approximately $c_{b_0}=3.050$ Å larger than that of the adamantane, and we have $b_0=a+c_{b_0}$. Similarly the maximum suction energy will occur when the radius of the tube is around $c_{b_{max}}=3.610$ Å in excess of that of the adamantane molecule.

We note that the equilibrium distance between the spherical adamantane and the cylindrical carbon nanotube (c_e = 3.446 Å) is very close to the inter-layer distance in graphite (3.414 Å) as given

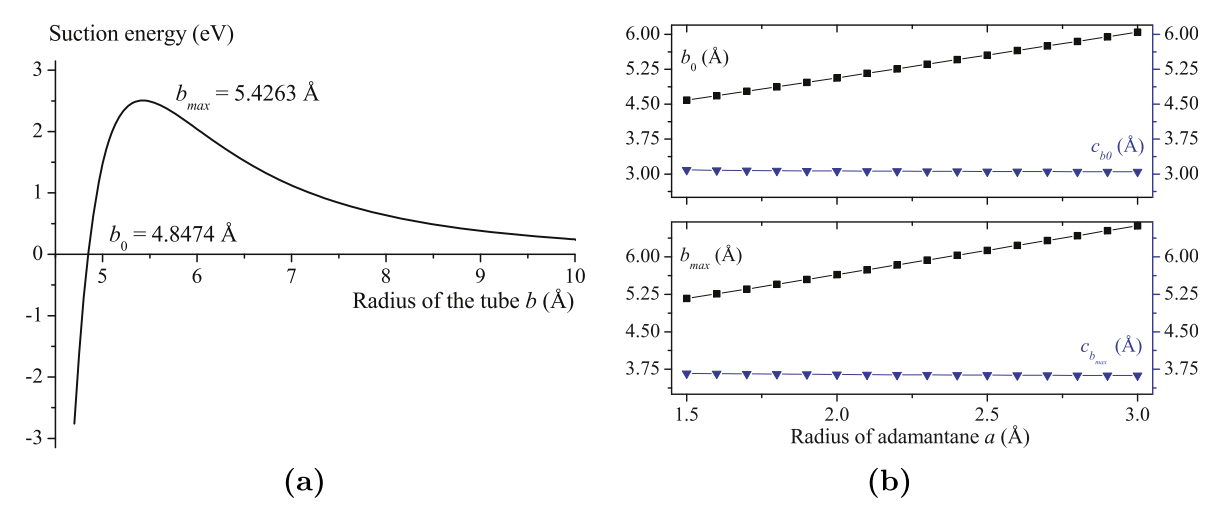


Fig. 5. (a) Suction energy for an adamantane of radius a = 1.773 Å encapsulated in carbon nanotube of radius b and (b) relation of adamantane radius a, the smallest radius of carbon nanotube b_0 that can encapsulate adamantane molecule and radius of tube b_{max} that gives maximum suction energy.

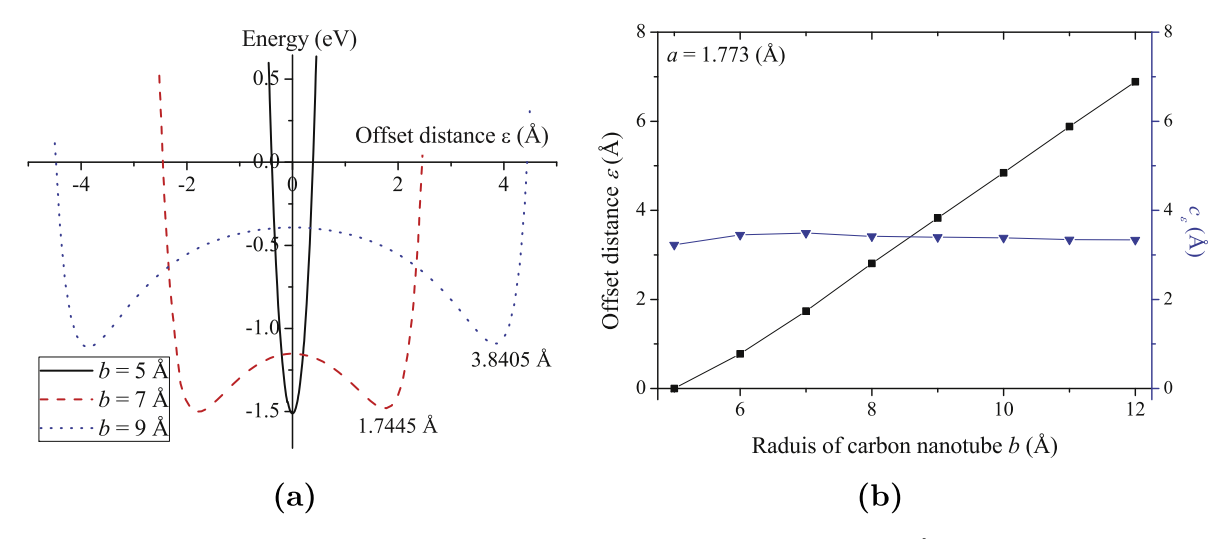


Fig. 6. (a) Interaction energy corresponding to offset location ε for adamantane molecule inside a tube of radii b = 5, 7, 9 Å and (b) linearly dependence of offset distance ε and carbon nanotube radius b when a = 1.773 Å.

by Girifalco et al. [21], or Shi et al. [15] who propose the value of 3.378 Å for the distance between a carbon chain and the carbon nanotube wall.

We have ignored here the effect of hydrogen due to its small mass and small Lennard-Jones potential parameters. However, if the hydrogen atoms were included we might expect slightly larger values of b_0 and b_{max} for the radii of carbon nanotubes that would encapsulate an adamantane molecule.

5. Summary

The continuous or continuum approach is employed to determine the interaction energies between two adamantane molecules and that of an adamantane molecule inside a carbon nanotube using the Lennard-Jones potential function. Adamantane is modelled as a perfect sphere with sp³ hybridization structure such as is found in diamond, while the carbon nanotube is assumed to be a cylinder with the sp² hybridization structure such as is found in graphene.

Calculation of the interaction energy using a radius of 1.773 Å for the adamantane molecule, we find that the equilibrium distance between the two adamantane molecules is 6.863 Å as measured from their centers which is within 10% of *ab inito* DFT calculations. However, the predicted binding energy is 52% different from the DFT calculations since only the van der Waals energy is taken into account here.

It is also found that the smallest radius of carbon nanotube that can encapsulate the adamantane is 4.847 Å which is within 2% of ab inito DFT calculations. The offset position ε from the tube axis is also examined, and a linear relation for $\varepsilon \approx b-a-c_\varepsilon$ is obtained where the distance between molecule and tube wall is $c_\varepsilon=3.446$ Å. The equilibrium distance between two molecules, suction energy for encapsulation and offset position depend linearly on the radius of the adamantane. We note that the structural information predicts the stable configurations close to those obtained from the DFT when taking only dipole-dipole interaction into account.

The major benefit of the mathematical modelling approach presented here is the use of significantly less computational resources and simplification reducing the trial-and-error process for designing experiments which allows to consider more complex systems. These findings constitute a first step toward the design of novel hybrid materials of carbon nanostructures.

Acknowledgements

D.B. is grateful for the support of the Thailand Research Fund (RSA5880003).

References

- [1] Y. Nakanishi, H. Omachi, N.A. Fokina, P.R. Schreiner, R. Kitaura, J.E.P. Dahl, R.M. K. Carlson, H. Shinohara, Template synthesis of linear-chain nanodiamonds inside carbon nanotubesfrom bridgehead-halogenated diamantane precursors, Angew. Chem. Int. Ed. 54 (2015) 10802–10806.
- [2] J. Zhang, Y. Feng, H. Ishiwata, Y. Miyata, R. Kitaura, J.E.P. Dahl, R.M.K. Carlson, H. Shinohara, D. Tomanek, Synthesis and transformation of linear adamantane assemblies inside carbon panetules. ACS Nano 6 (2012) 8674–8683
- [3] P.R. von Schleyer, A simple preparation of adamantane, J. Am. Chem. Soc. 79 (1957) 3292.
- [4] J.C. Garcia, J.F. Justo, W.V.M. Machado, L.V.C. Assali, Functionalized adamantane: building blocks for nanostructure self-assembly, Phys. Rev. B 80 (2009) 125421.
- [5] R.C. Merkle, Molecular building blocks and development strategies for molecular nanotechnology, Nanotechnology 11 (2000) 89–99.
- [6] T. Maugh, Panel urges wide use of antiviral drug, Science 206 (1979) 1058–1060
- [7] S.S.Y. Wong, K.-Y. Yuen, Avian influenza virus infections in humans, Chest 129 (2006) 156–168.
- [8] V.M. Deyde, X. Xu, R.A. Bright, M. Shaw, C.B. Smith, Y. Zhang, Y. Shu, L.V. Gubareva, N.J. Cox, A.I. Klimov, Surveillance of resistance to adamantanes among influenza A(H3N2) and A(H1N1) viruses isolated worldwide, J. Infect. Dis. 196 (2007) 249–257.
- [9] M.E. Burstein, A.V. Serbin, T.V. Khakhulina, I.V. Alymova, L.L. Stotskaya, O.P. Bogdan, E.E. Manukchina, V.V. Jdanov, N.K. Sharova, A.G. Bukrinskaya, Inhibition of HIV-1 replication by newly developed adamantane-containing polyanionic agents, Antiviral Res. 41 (1999) 135–144.
- [10] A. El-Emam, O.A. Al-Deeb, M. Al-Omar, J. Lehmann, Synthesis, antimicrobial, and anti-HIV-1 activity of certain 5-(1-adamantyl)-2-substituted thio-1,3,4-oxadiazoles and 5-(1-adamantyl)-3-substituted aminomethyl-1,3,4-oxadiazoline-2-thiones, Bioorg. Med. Chem. 12 (2004) 5107–5113.
- [11] G.C. McIntosh, M. Yoon, S. Berber, D. Tománek, Diamond fragments as building blocks of functional nanostructures, Phys. Rev. B 70 (2004) 045401.
- [12] B.W. Smith, M. Monthioux, D.E. Luzzi, Encapsulated C₆₀ in carbon nanotubes, Nature 396 (1998) 323–324.
- [13] B.W. Smith, D.E. Luzzi, Formation mechanism of fullerene peapods and coaxial tube: a path to large scale synthesis, Chem. Phys. Lett. 321 (2000) 169–174.
- [14] D. Baowan, N. Thamwattana, J.M. Hill, Zigzag and spiral configurations for fullerenes in carbon nanotubes, J. Phys. A: Math. Theor. 40 (2007) 7543–7556.
- [15] L. Shi, P. Rohringer, K. Suenaga, Y. Niimi, J. Kotakoski, J.C. Meyer, H. Peterlik, M. Wanko, S. Cahangirov, A. Rubio, Z.J. Lapin, L. Novotny, P. Ayala, T. Pichler, Confined linear carbon chains as a route to bulk carbyne, Nat. Mater. 15 (2016) 634–640
- [16] S.G. Balasubramani, D. Singh, R.S. Swathi, Noble gas encapsulation into carbon nanotubes: predictions from analytical model and dft studies, J. Chem. Phys. 141 (2014) 184304.
- [17] B.J. Cox, N. Thamwattana, J.M. Hill, Mechanics of atoms and fullerenes in single-walled carbon nanotubes. I. Acceptance and suction energies, Proc. Roy. Soc. A 463 (2007) 461–476.
- [18] A.K. Rappé, C.J. Casewit, K.S. Colwell, W.A. Goddard III, W.M. Skiff, UFF, a full periodic table force field for molecular, J. Am. Chem. Soc. 114 (1992) 10024– 10035.
- [19] D. Baowan, B.J. Cox, T.A. Hilder, J.M. Hill, N. Thamwattana, Modelling and Mechanics of Carbon-Based Nanostructured Materials, first ed., Matthew Deans, Elsevier, 2017.
- [20] I.S. Gradshteyn, I.M. Ryzhik, Table of Integrals, Series, and Products, seventh ed., Academic Press, 2007.
- [21] L.A. Girifalco, M. Hodak, R.S. Lee, Carbon nanotubes, buckyballs, ropes, and a universal graphitic potential, Phys. Rev. B 62 (2000) 13104–13110.